Since January 2020 Elsevier has created a COVID-19 resource centre with free information in English and Mandarin on the novel coronavirus COVID-19. The COVID-19 resource centre is hosted on Elsevier Connect, the company's public news and information website.

Elsevier hereby grants permission to make all its COVID-19-related research that is available on the COVID-19 resource centre - including this research content - immediately available in PubMed Central and other publicly funded repositories, such as the WHO COVID database with rights for unrestricted research re-use and analyses in any form or by any means with acknowledgement of the original source. These permissions are granted for free by Elsevier for as long as the COVID-19 resource centre remains active.

CHAPTER

Nanotechnologies for early diagnosis, in situ disease monitoring, and prevention

1

SUBCHAPTER

Fluorescent nanodiamond for tracking the engraftment and repair of lung stem cells

1.1

Tsai-Jung Wu*, Hsiao-Yu Chiu*,, John Yu*,†**

**Institute of Stem Cell and Translational Cancer Research, Chang Gung Memorial Hospital, Kuei Shang, Taiwan; **China Medical University, Taichung, Taiwan; †Institute of Cellular and Organismic Biology, Taipei, Taiwan*

1 INTRODUCTION

Adult lung is lined by dynamic airway epithelium. The integrity of epithelium is essential for the maintenance of normal lung functions. To preserve its homeostasis and normal functions following injuries caused by various environmental insults, such as inhaled pollutants and inflammatory responses, a variety of stem cells in respiratory epithelium that would turnover in a steady state and lung injury further incurred the proliferation of stem/progenitor cells and differentiation to form all cell types. Furthermore, crosstalk between lung stem cells (LSCs) and the microenvironmental stem cell niche is crucial for the maintenance of the balance of stem cells and their differentiated derivatives and tissue homeostasis. Defects in such interactions may lead to lung damages and diseases.

Diseases, such as lung cancer and chronic obstructive pulmonary disease, are severe and slowly progressive and disabling disorders associated with an accelerated decline in lung function, and are among the most common causes of death in the world. Research on LSCs has significant implications for understanding how the airway epithelium develops and functions in health and disease and may provide the basis for future treatments. Stem cells can be defined as unspecialized cells capable of self-renewal and differentiation into diverse tissue- or organ-specific cells. Stem cells are also essential for embryonic development and organogenesis. In addition, during normal tissue turnover or injury, stem cells are essential for the maintenance

Nanotechnologies in Preventive and Regenerative Medicine. http://dx.doi.org/10.1016/B978-0-323-48063-5.00001-0
Copyright © 2018 Elsevier Inc. All rights reserved.

of homeostasis and repair of adult tissues. Stem cells normally are quiescent, proliferating infrequently, and can undergo asymmetric cell division. In response to injury, stem cells can proliferate rapidly and give rise to differentiated cells.

The cell-based regenerative medicine has opened new ways for therapeutic strategies for protection and repair of damaged tissues. Therefore, the ability to monitor the viability, distribution, and differentiation of the transplanted stem cells in vivo is a prerequisite for a better understanding of the role of stem cells play in the therapeutic process. For successful development of cell-based therapy, it is essential to facilitate and improve the number of stem cells engrafted in the target area and to monitor the trafficking of labeled stem cells by molecular and cellular imaging. A cell-labeling strategy is currently performed using the probes incorporated into the cells or transfecting the reporter genes into the genome. Nanotechnology that provided the functional elements at the nanoscale level is an enabling technology with great potential for applications in cell-based therapy.[1,2]

Traditionally, the fate of the transplanted stem cells is generally assessed by direct labeling in vitro with fluorescent dyes, radionuclides (e.g., Indium^{111} oxine), and thymidine base analogs (e.g., BrdU), or indirect labeling through transfected genes, such as fluorescent protein (e.g., GFP) or other reporter proteins (e.g., luciferase). However, several limitations exist, such as the dilution or exclusion of the imaging probes after labeling of cells, insertional mutagenesis of the transfected cells, changes of cell phenotypes and functions, and the compounded issues with tissue autofluorescence.[3,4] In comparison to the traditional fluorescent probes, such as fluorescent proteins and small-molecule dyes, nanoparticle-based probes are advantageous in terms of their photostabilities and minimal alterations to the cell phenotypes and functions.

However, an ideal imaging technology for stem cell tracking should have several unique features: (1) biocompatibility and nontoxicity of the exogenous contrast agent, (2) lack of genetic modification or perturbation to the stem cells, (3) resolution with single-cell detection at an appropriate anatomic location, (4) ability for quantification, (5) minimal or no transfer of contrast agent to other cells not originally labeled, (6) noninvasive imaging in the living subject for long term, (7) no requirement for injectable contrast modalities, and so on.[5] To fulfillment of these conditions requires the use of a highly sensitive imaging modality, as well as the employment of a highly stable (both biologically and photophysically) imaging probe, to allow tracking of the transplanted cells in vivo over an extended period of time.

Currently, many nanomaterials, such as quantum dots (QDs), silica nanoparticles, and polymer nanoparticles, that are used for fluorescence imaging; noble metal nanoparticles, such as gold particles, that are useful for photoacoustic imaging; superparamagnetic iron oxide particles, which are the most suitable for magnetic resonance imaging, are used to label and track stem cells in vitro and in vivo. In comparison to other modalities, such as magnetic resonance imaging, photoacoustic imaging, positron emission tomography, and computed tomography, optical imaging possesses distinctive advantages, such as low cost, easy accessibility, high spatial and

temporal sensitivity, large in vitro and in vivo throughputs, and greater potential for clinical translation.[6]

For example, QDs are a very popular fluorescent platform that can be used with single- or multiphoton imaging techniques. Although QDs have been adopted and highly regarded as a fluorescence imaging medium, the application is hampered by their potential toxicity (e.g., CdSe QDs are trapped in endosomes/lysosomes after endocytosis) and facile degradation (e.g., the decline of fluorescence as pH decreases).[2,7–11] Indeed, the existence of heavy metals in QDs, such as cadmium, a well-established human toxicant and carcinogen, poses potential dangers especially for future medical application. As the use of nanomaterials for biomedical applications is increasing, environmental pollution and toxicity have to be addressed, and the development of a nontoxic and biocompatible nanomaterial is becoming an important issue. Fluorescent nanodiamond (FND), a new member in the nanocarbon family, has recently emerged as a promising nanotechnology imaging probe for biomedical applications.[12–16] FNDs combine the advantages of QDs (small size, high photostability, and bright multicolor fluorescence) with biocompatibility, nontoxicity, and rich surface chemistry that have the potential to revolutionize imaging applications.[16–18]

2 FLUORESCENT NANODIAMOND

Nanodiamond, which is comprised of sp^3-hybridized carbon, belongs to the carbon-based nanomaterial family.[12] Owing to their low chemical reactivity and unique physical properties, nanodiamonds could be useful in a variety of biological applications. The natural diamonds have aggregated nitrogen defects (type Ia diamonds), while synthetic diamonds manufactured under high-temperature and high-pressure conditions are mainly embellished with single–substitutional nitrogen centers (type Ib diamonds).[19,20] Irradiation damage of type Ib diamond nanocrystallites generates intrinsic defects, such as vacancies in the diamond structure. During thermal annealing, these vacancies move toward nitrogen centers and get trapped within to form nitrogen-vacancy (NV) color defect centers. Then these centers lead to useful fluorescence properties. When excited by green-yellow light (515–560 nm), the fluorophores (e.g., the negatively charged NV centers, NV^-) built in the FND emit stable far-red emission (600–800 nm) with a fluorescence lifetime (τ) of greater than 15 ns.[13,21] In addition, when photoexcited with 8 kW/cm^2 power density of light for 5 min, no photobleaching occurred in FNDs. In contrast, under the same conditions, the fluorescence of an Alexa Fluor dye photobleached and faded completely in 12 s.[12,13] Furthermore, no fluorescence blinking was detected within a time resolution of 1 ms.[13] Overall, the extreme photostability of the NV^- defect centers provides a great advantage to FNDs to emerge as an excellent candidate for long-term cellular imaging and tracking.

One important issue of concern for biomedical application is the autofluorescence from cells or tissues. Fluorescence from endogenous components in live cells and

tissues, or from fixative-induced fluorescence, are commonly referred to collectively as "autofluorescence," which is the major source of the fluorescence background in imaging experiments involving biological samples. The majority of cell autofluorescence originates from mitochondria and lysosomes. Together with aromatic amino acids and lipopigments, the most important endogenous fluorophores are pyridinic (NADPH) and flavin coenzymes. In tissues, the extracellular matrix often contributes to the autofluorescence emission more than the cellular component because collagen and elastin have, among the endogenous fluorophores, a relatively high quantum yield. The absorption and emission waves of cellular endogenous fluorophores, ranging from 400 to 500 nm, overlap with most of the organic fluorophores used for cellular imaging. The far-red fluorescence emission of FND, peaking at about 700 nm, is well separated from the cellular autofluorescence region of biological specimens.[12,13]

Another important parameter that could be utilized to improve the image contrast of fluorescence probes within a biological environment is the issue of fluorescence lifetime. The fluorescence lifetime is defined as the time the fluorophore remains in the excited state before returning to the ground state. The average fluorescence lifetime of FNDs is 17 ns, which is considerably longer than that typical of tissue autofluorescence or common fluorescent imaging dyes ($\tau < 6$ ns).[22,23] By fluorescence lifetime imaging microscopy (FLIM) and various nanosecond time-gating techniques, it is possible to separate FND emission from the strong autofluorescence background of host tissue.[21,24,25]

3 IN VITRO AND IN VIVO STUDIES USING FLUORESCENT NANODIAMOND

Nanotechnologies have great potential in enhancing stem cell research and stem cell therapy. FNDs in the size range of 100 nm were produced by ion irradiation and thermal annealing of type Ib diamond powders, followed by air oxidation and purification in strong oxidative acids.[14] As mentioned, FNDs are novel imaging probes that are not only chemically robust and fluorescently stable, but also biologically inert and nontoxic. Therefore, FNDs might be an alternative for the long-term labeling of stem cells. In the past few years, several biocompatibility and cytotoxicity studies have been conducted to examine cell viability, oxidative stress, DNA damage, and physiological processes in vivo after labeling of cells with FNDs.[26,27] It was shown that FNDs could be used in many cell lines without obvious cytotoxicity, such as kidney (HEK 293T),[12] lung (A549 and HFL-1),[28,29] neuronal (Neuro2a),[30] and cervical (HeLa) cells.[31,32] The internalization of FNDs did not affect the cell viability and cell division, as assessed by monitoring mitochondrial function and luminescent ATP production.[26] By time-lapse imaging and flow cytometric analysis, it was observed that the number of FND nanoparticles were divided nearly equally between daughter cells during cell division, and the fluorescence intensity in each cell decreased exponentially with time due to cell proliferation.[32] Moreover, FND-labeled 3T3-L1 preadipocyte and 489-2.1 osteoprogenitor cells did not have any cytotoxic or detrimental

effects on the proliferation and differentiation potential of these cells.[31] With flow cytometry, transmission electron microscope, and the use of a series of metabolic and cytoskeletal inhibitors, it was found that the mechanism of the FND uptake in cells was facilitated via energy-dependent clathrin-mediated endocytosis.[28,31] Additionally, no significant exocytosis of FNDs was found during cell proliferation.[32]

Besides these cellular studies, some histopathological examinations have been conducted to evaluate the toxicity of nanodiamonds in vivo. The intratracheally administered nanodiamonds did not cause any pulmonary toxicity; the amount of nanodiamonds in alveolar cells decreased with time, and the macrophages burdened with nanodiamonds were clearly observed in the bronchia for approximately 1 month after exposure.[33] Moreover, the intradermal, subcutaneous, and intraperitoneal injections of nanodiamonds did not induce any inflammatory reactions and systemic toxicity in mice and rats.[34,35] On microinjection into wild-type *Caenorhabditis elegans*, FNDs were dispersed in the gonad, delivered to the embryos, and eventually into the hatched larvae in the next generation.[17] Recently, Simpson et al. had also demonstrated that microinjected FNDs were effective nanoscale fluorescent probes for determining the intracellular dynamics in developing *Drosophila* embryos.[36] Overall, FNDs are photostable, biocompatible, and nontoxic, which have potential use in labeling, imaging, and tracking of the cellular and developmental processes in vitro and in vivo.[18,37] In our recent work, we also demonstrated that FND labeling did not impair the biological functions of LSCs.[25]

4 REGENERATION AND STEM CELLS IN LUNG

The adult lung is a complex organ consisting of at least 40 different cell lineages and is developed sequentially by early epithelial tube branching and late septation of terminal air sacs.[38] Based on the anatomical and functional features, the lung can be further divided into three epithelial domains with distinct composition of epithelial cell types: the proximal cartilaginous airway (trachea and bronchi), distal bronchioles (bronchioles, terminal bronchioles, and respiratory bronchioles), and gas-exchanging airspaces (alveoli).[39] In human and mice, the trachea and bronchi are lined by a pseudostratified epithelium that contains basal, ciliated, secretory (goblet, serous, and club cells), and a small number of neuroendocrine cells.[40] In addition, submucosal glands are composed of an interconnecting network of serous and mucous tubule that secrete liquid for hydrating airway surfaces, supporting mucociliary transport and serving as a fluid matrix for numerous secreted macromolecules, including the gel-forming mucins.[41] In the bronchioles, the cuboidal epithelium contains secretory club cells and fewer ciliated cells than in more-proximal airway regions. Of note, the neuroendocrine cells are found to be residing individually or as clusters in neuroepithelial bodies in the distal airway.[42] The alveolar epithelium that leads by terminal bronchioles are composed of two epithelial cell types, alveolar type I pneumocytes (AECI) and alveolar type II pneumocytes (AECII). AECI cells, which are essential for gas exchange, are large flat squamous cells covering about 95% of the alveolar

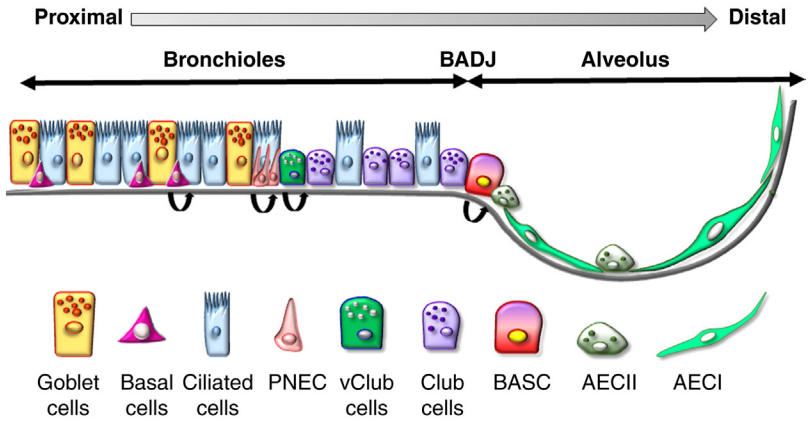

FIGURE 1.1.1 Various Subpopulations of Cells Around the Bronchoalveolar Duct Junction *(BADJ)*.

Schematic presentation shows the distribution of various cell subpopulations in the lung epithelia. Basal cells, pulmonary neuroendocrine cells *(PNEC)*, naphthalene-resistant variant club cells *(vClub cells)*, and bronchoalveolar stem cells *(BASC)* of the BADJ are proposed to be self-renewing stem cell populations. *AECI*, Alveolar type I pneumocytes; *AECII*, alveolar type II pneumocytes.

surface. The relatively smaller, granular, and roughly cuboidal AECII cells, which produce surfactant components, critical for the maintenance of alveolar integrity,[43] contribute to only ~5% of the alveolar surface. As shown in Fig. 1.1.1, there are various subpopulations of cells around bronchoalveolar duct junction (BADJ), where the LSCs for alveolar sac reside.

Endogenous LSCs have been found to be able to renew and proliferate to epithelial cells in vivo. They are potentially useful in regenerative therapy, such as repairing damaged lung tissue in patients. During the pseudoglandular stage of lung development, the distal tips of the branching tubules appear to contain the undifferentiated multipotent $Id2^+$ tip cells that can self-renew and contribute descendents to all epithelial cell lineages.[44] Following postnatal growth, the lung epithelium slowly turns over (~1% per day) under normal conditions, but its regenerative capacity can be substantially activated after injury.[45,46] The large surface area, numerous branches, and folded topography suggest that lung tissue may have several stem or progenitor cell types. Different regional stem cells in lung are responsible for postnatal lung growth, homeostasis, and repair of the injured lungs, and contribute differently to local needs in times of tissue damage.[47]

For example, in trachea and main stem bronchi, a subset of basal cells are the dominant epithelial stem cell type responsible for homeostasis and injury repair, which possess a capacity to different into the basal, ciliated, goblet, and granular secretory cells in vivo.[48,49] Several cellular markers, including the cytokeratin 5, cytokeratin 14, integrin α6, and nerve growth factor receptor, have been employed in the

identification and isolation of basal cells.[50,51] On the other hand, in the gas exchange alveolar epithelium, a subset of AECII cells have been recognized as precursors for AECI cells in the adult lung. By ^{3}H-thymidine labeling, clonogenic assays, and genetic lineage tracing analysis, AECII cells are able to proliferate and restore the alveolar epithelium by giving rise to either new AECII or the squamous AECI cells following an injury.[23–25] Moreover, in an attempt to identify biomarkers for AECII stem cells, a subset of prosurfactant protein C (SP-C)$^{-}$/integrin $\alpha6\beta4^{+}$ cells are found to sporadically localize in alveolar epithelia and possess the capacity for proliferation, further differentiation of SP-C^{+} AECII, and regeneration of lung structures.[26]

To date, at least a subset of basal, secretory, and mucous cells in the submucosal glands of the proximal airways, variant club cells in the bronchioles, bronchoalveolar stem cells (BASCs) in the BADJ of terminal bronchioles (Fig. 1.1.1), and a subset of AECII cells in alveolar space have been suggested to be as region-specific epithelial stem/progenitor cells in the adult lung of mice and humans.[38,39,52–58]

In the distal airway, the bronchiolar epithelium is quiescent until injury. Following naphthalene-mediated club cell ablation, a small number of naphthalene-resistant club cells (termed variant club cells) survive and regenerate all differentiated distal bronchiolar cell types.[54,55] These variant club cells expressing club cell secretory protein (CCSP), but not CyP450-2F2 (CCSP^{+}, CyP450-2F2^{-}), are located within the neuroepithelial bodies and the BADJ. Kim et al. also identified a subpopulation of club cells that coexpress CCSP and SP-C, referred to as BASCs, which is another naphthalene-resistant progenitor cell population located at the BADJ.[56] Using a naphthalene- or bleomycin-induced murine lung injury model, they further demonstrated that these cells possessed a capacity for self-renewal and injury repair in vivo and an ability to differentiate into club cells and alveolar epithelial cells.[56] In addition to BASCs, our lab had previously reported a serum free–selective culture procedure to sustain preferential growth of the lung colonies, which was further supported by pulmonary mesenchymal cells in the surrounding.[59] The Oct-4–expressing cell population also residing in the terminal bronchiolar region of neonatal lungs was introduced as a putative neonatal lung stem/progenitor cell that is capable of being cultured in vitro for weeks and induced to differentiate into AECII and AECI cells. Interestingly, these cells were susceptible to infection with the severe acute respiratory syndrome (SARS) virus, raising the possibility that LSCs may be specific disease targets.[59] Therefore, our study suggests that the LSCs could be targets for environmental agents, including pneumotropic pathogens.

5 ISOLATION AND CHARACTERIZATION OF CD45⁻ CD54⁺CD157⁺ LUNG STEM CELLS

As LSCs play protective roles in epithelial repair and tissue homeostasis, direct isolation of these cells is important but challenging. On one hand, it is conceivable that different populations of stem cells could be isolated from different regions of lung tissues. Several comprehensive analyses, such as transcriptomic and proteomic analyses, had

been used to elucidate the gene and protein expression profiles and determine novel molecular markers. However, specific surface markers on cells are more valuable for the isolation of stem cells, but many commonly used stem cell markers are often adopted from phenotypic characteristics of other cell types, such as hematopoietic cell lineages, with limited insight into the specific stem cells under study.

Although several putative markers of stem cell subpopulations for lung tissue have been studied in great detail, such as the BASCs at BADJ and the basal cells in proximal airways, a specific marker for unambiguous identification and isolation of LSCs has not been defined yet.[60–62] More specific surface markers are thus needed for the preparation of a homogenous population of LSCs.[39] As more than 85% of cell surface components are glycosylated, the glycomic analysis is useful to probe the stem cell and cancer cell surface systematically in search for novel glycoproteins and glycolipids.[63,64]

Recently we took another step forward by developing a new and prospective isolation method to obtain LSCs with glycoproteomics analysis (Fig. 1.1.2A).[25] Briefly, alkynyl sugar derivatives can be incorporated into glycoproteins, which can be tagged with biotin azide using click chemistry, permitting their enrichment from proteomes via affinity capture with immobilized avidin.[65] Following tryptic digestion on beads, the protein ID can be identified by liquid chromatography/tandem mass spectrometry (LC-MS/MS) (Fig. 1.1.2A). From such an analysis, we identified a total of 164 proteins, of which only 83 were uniquely expressed in the LSC-enriched cell population. Examination with UniProt database indicated that 14% of these 83 glycoproteins were plasma membrane proteins (e.g., 12 surface markers). According to the real-time polymerase chain reaction (PCR) and immunofluorescent staining, it was found that CD157 (bone marrow stromal cell antigen 1, BST-1) was specifically expressed on the cell surface of LSC colonies than other types of more differentiated lung cells (Fig. 1.1.2B). In addition, it was also shown that $CD157^+$ cells in lung section are located at terminal bronchioles and BADJ upon immunohistochemical analysis (Fig. 1.1.2B), consistent with the BrdU retaining cells in our previous study.[59] Therefore, CD157 was used as one new surface marker in ensuing experiments for prospective isolation of LSCs.[25] Through fluorescence-activated cell sorting (FACS) with staining with two specific cell surface markers (CD54 and CD157), propidium iodide, and the CD45 antibody, we achieved the isolation of a subpopulation of cells highly enriched for LSCs from neonatal lung tissues.[25] These $CD45^-CD54^+CD157^+$ cells were not only capable of self-renewal, but could also maintain colony morphology after serial passages (Fig. 1.1.2C). Furthermore, these isolated cells could be cryopreserved and thawed without significant loss of their ability for cell renewal and extensive expansion. Similar to the originally isolated LSCs, the cobblestone-like cell morphology was maintained after expansion. To fully characterize the sorted $CD45^-CD54^+CD157^+$ cells, immunofluorescence analysis was first performed at the time of isolation. These isolated cells expressed the club cell marker (CCSP) and the epithelial cell marker (cytokertain-7) but not pneumocytes markers.[25] After 7–10 days of culture in growth medium, there were no changes in the expression of these markers (Fig. 1.1.2C).

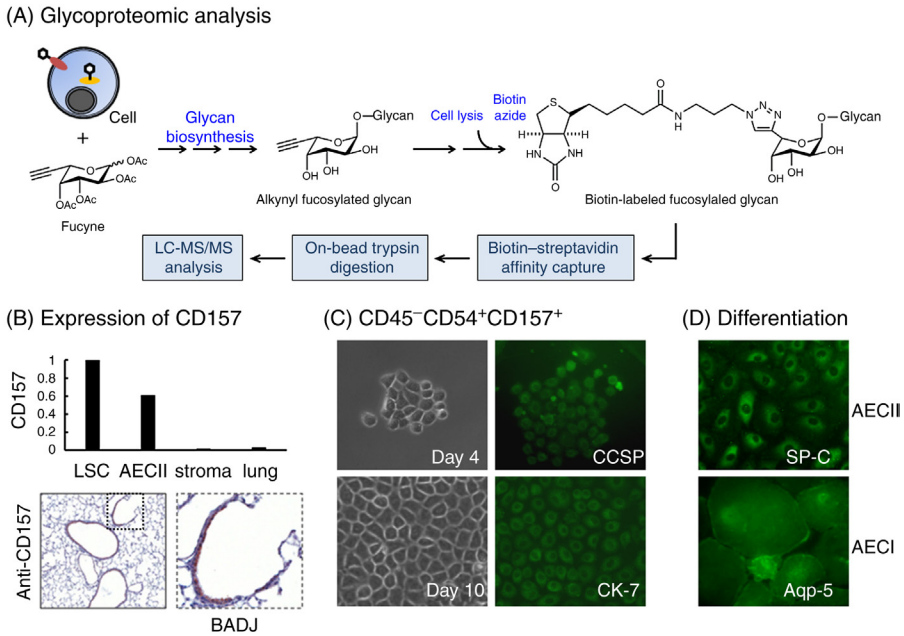

FIGURE 1.1.2 Isolation and Characterization of CD45⁻CD54⁺CD157⁺ Lung Stem Cells (LSCs).

(A) Workflow of the glycoproteomic analysis. (B) mRNA expression associated with CD157 in LSC-enriched cells, AECII, stromal cells, and lung tissues. Immunohistochemical staining for CD157 (*black*; *brown* in the web version) in lung tissue sections of the neonatal mice. (C) Phase contrast imaging of LSC colonies derived from sorted CD45⁻CD54⁺CD157⁺ cells on day 4 and 10. Immunofluorescence staining of the sorted CD45⁻CD54⁺CD157⁺ cells with anti-cytokeratin *(CK-7)* and anti-CCSP antibodies. (D) Examination for the induced differentiation of CD45⁻CD54⁺CD157⁺ cells with the AECII marker, prosurfactant protein C *(SP-C)*, after incubation in MCDB201 medium for 7 days, and then with the AECI marker, Aquaporin 5 *(Aqp-5)*, after incubation for another 14 days. *LC-MS/MS*, Liquid chromatography/tandem mass spectrometry.

Adapted from Fig. 1 in Wu TJ, Tzeng YK, Chang WW, Cheng CA, Kuo Y, Chien CH, et al. Tracking the engraftment and regenerative capabilities of transplanted lung stem cells using fluorescent nanodiamonds. Nat Nanotechnol *2013;**8**(9):682–9.*[25]

In addition to the ability of self-renewal and expansion, we also examined whether the sorted and expanded CD45⁻CD54⁺CD157⁺ cells possessed the capacity of stem cells for differentiation. After 7 days of incubation in induction medium, the cell shape became flattened, the size became larger, and the AECII cell marker (SP-C) expression was detected in the cytoplasm close to the perinuclear region, which is indicative of cell differentiation into AECII cells (Fig. 1.1.2D).[25] Extension of the incubation to 14 days led to further flattening and enlargement of the cells (approximately fivefold greater than that of the original undifferentiated cells). These morphological changes were accompanied with a decrease in SP-C expression and an increase in

the AECI cell marker (Aquaporin 5, Aqp-5) expression, an indication that these prospectively isolated $CD45^{-}CD54^{+}CD157^{+}$cells have the potential to differentiate into AECII cells and then AECI cells in a sequential manner (Fig. 1.1.2D).[25]

6 IN VIVO TRACKING OF FND-LABELED LUNG STEM CELLS

When $CD45^{-}CD54^{+}CD157^{+}$ LSCs were labeled with 100 μg/mL FNDs, we showed that the FND-labeled cells displayed one useful feature in flow cytometric analysis. In addition to far-red fluorescence, data collected in the side scatter channel (SSC) also provide useful information on the FND uptake.[25,32] This is due to the fact that diamond has the highest refractive index of all transparent minerals, and diamond nanoparticles scatter light strongly in the visible region and thus produce strong SSC signals. By properly gating the bivariate plot (SSC versus far-red) in quadrants, two distinct separate populations of FND-labeled and unlabeled cells could be detected in these two channels.[25,32] The double-positive cell population, denoted as $SSC^{+}Far\text{-}red^{+}$, was subsequently identified as the FND-labeled cells without additional staining.[25,32]

Furthermore, our analysis revealed that both the control and FND-labeled LSCs were able to undergo morphological alterations and express SP-C on day 7 after induction of LSCs to form AECII cells, implying that the endocytic FNDs do not change the apparent biological functions of stem cells (Fig. 1.1.3).[25] Furthermore, no interference of FNDs was detected in the differentiation from AECII to AECI, suggesting that FNDs did not impair the biological functions of these LSCs (Fig. 1.1.3).[25] In addition, we tracked the proliferation of the FND-labeled LSCs continuously over 2 weeks by flow cytometry and found that the $CD45^{-}CD54^{+}CD157^{+}$ LSCs labeled with FNDs were viable and continued proliferate for at least 2 weeks (approximately seven divisions), suggesting that the extent of the FND exocytosis is low.

To track the homing capacity of the isolated and expanded LSCs in vivo, 5×10^{5} FND-labeled $CD45^{-}CD54^{+}CD157^{+}$ cells were injected into the tail vein of adult mice. In addition to lungs, other tissues, such as kidney, liver, and spleen, were also harvested for examination on days 1, 4, and 7 after intravenous (i.v.) injection of the FND-labeled $CD45^{-}CD54^{+}CD157^{+}$ cells in mice. Lung tissue sections from mice infused with FND-labeled cells were then prepared for fluorescence imaging (Fig. 1.1.4). Meanwhile, to verify that the FND-labeling was not a consequence of FND engulfment by macrophages, lung sections were stained with a macrophage-specific antibody, F4/80, followed by hematoxylin counterstaining (Fig. 1.1.4A).[25]

However, during the search for FNDs in the immunohistochemically stained tissue sections, it was noted that the imaging was overwhelmed by tissue autofluorescence and also by the fluorescence derived from photoexcitation of the hematoxylin counterstain, thus preventing the detection of the FND signal (Fig. 1.1.4B).[25] With the use of FLIM, however, the background fluorescence and the FND signals can be readily separated because the fluorescence lifetime of FND, which is substantially longer than that of the endogenous autofluorescence in tissue sections (typically 1–4 ns) (Fig. 1.1.4C).[25] By gating the time at 7 ns, the location of FNDs in the lung

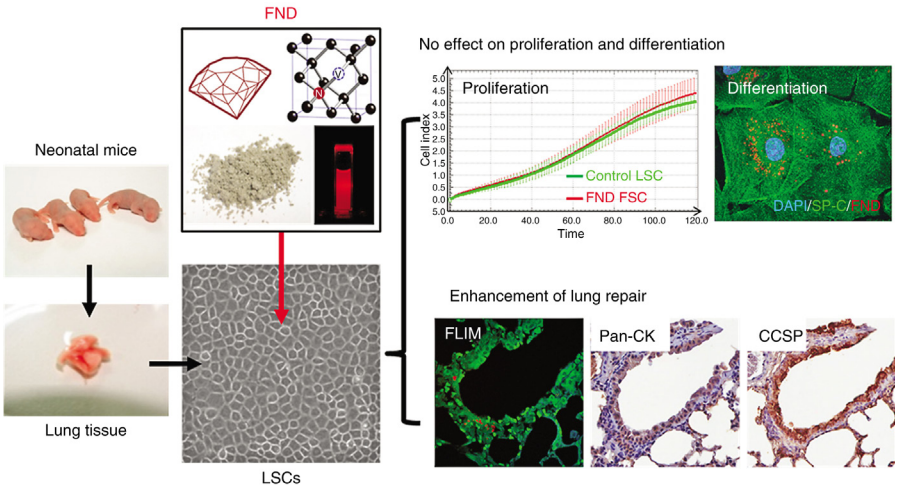

FIGURE 1.1.3 Labeling of Fluorescent Nanodiamond (FND) in LSCs.

Labeling of the prospectively isolated LSCs with FNDs did not eliminate the abilities of stem cells for proliferation and differentiation into type I and type II pneumocytes in vitro. The FND labeling in combination with fluorescence-activated cell sorting (FACS), fluorescence lifetime imaging microscopy (FLIM), and time-gated fluorescence (TGF) imaging could identify the LSCs transplanted in vivo and allows tracking of their engraftment and regenerative capabilities with single-cell resolution.

tissue could now be clearly identified (Fig. 1.1.4D–E).[25] Furthermore, overlapping the bright-field and TGF images indicated that FNDs were not colocalized with macrophages in lung tissues, leading to the conclusion that FND-labeled LSCs in alveolar sac regions had not been engulfed by alveolar macrophages.

From flow cytometric identification of $SSC^{+}Far\text{-}red^{+}$ cells, we confirmed that the injected $CD45^{-}CD54^{+}CD157^{+}$ cells preferentially resided in the lungs and not in other tissues. It was also found that on day 1, approximately 1.6% of the total population of viable cells in the lungs appeared as FND-labeled LSCs. The fraction of the $SSC^{+}Far\text{-}red^{+}$ cells, however, decreased to 0.2 and 0.1%, respectively, on day 4 and 7 after the injection. To further verify whether the $SSC^{+}Far\text{-}red^{+}$ cells sorted by FACS were truly the FND-labeled $CD45^{-}CD54^{+}CD157^{+}$ cells that we has injected, lung tissue sections were stained with hematoxylin and eosin (H&E) for a morphological analysis. The time-gating technique had similarly been applied to image lung tissues prepared on days 1, 4, and 7. Again, the FND fluorescence (red spots) could be readily distinguished from the background fluorescence with the time gated at >7 ns (Fig. 1.1.4D–E). Further confirmation of the FNDs was made by prolonged excitation, which did not lead to any significant decrease in fluorescence intensity, consistent with the characteristic of FND fluorescence.[12,13] From the merged images of bright-field H&E staining and TGF, it was found that while some FND-labeled LSCs were trapped in interalveolar spaces (Fig. 1.1.4A), many of them resided close

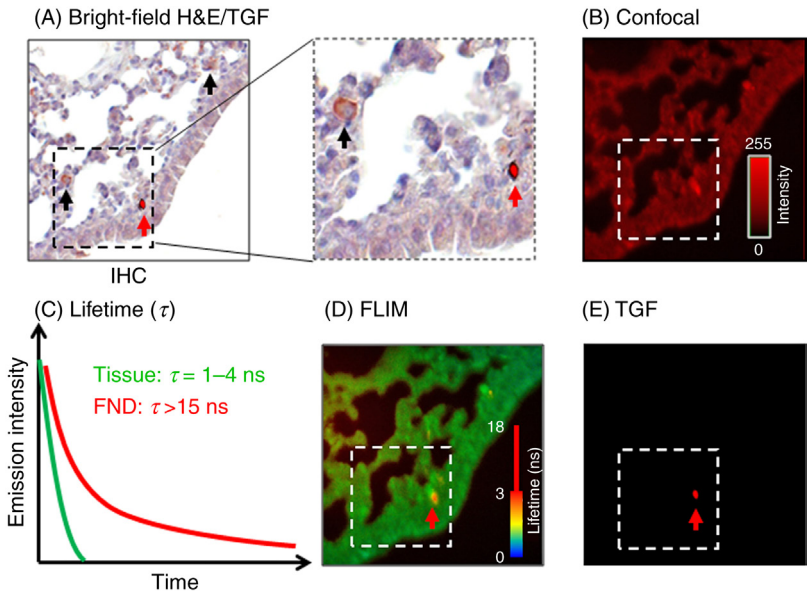

FIGURE 1.1.4 FND-Labeled LSCs in Uninjured Mice.

(A) The merged images of the antimacrophage antibody (F4/80) immunostaining with hematoxylin and eosin (H&E) and the TGF, which display the different locations for macrophages (*brown*, denoted by *black arrows*) and FND-labeled cells (*red*, denoted by *red arrows*) in lung tissue. The same tissue section also was visualized with (B) confocal fluorescence, (D) FLIM, and (E) TGF. The fluorescence imaging gated at time > 7 ns clearly reveals the location of FNDs (*red arrow*). (C) Comparison between the fluorescence lifetimes of autofluorescence in cells and tissues (*green*) and FNDs (*red*).

Adapted from Fig. 3 in Wu TJ, Tzeng YK, Chang WW, Cheng CA, Kuo Y, Chien CH, et al. Tracking the engraftment and regenerative capabilities of transplanted lung stem cells using fluorescent nanodiamonds. Nat Nanotechnol *2013;**8**(9):682–9.*[25]

to terminal bronchioles or BADJs. In addition, these FND-labeled cells were retained in this region of the lung for at least 7 days after injection.

7 HOMING AND ENGRAFTMENT OF LUNG STEM CELLS IN LUNG-INJURED MICE

To demonstrate the potential of LSCs for homing and engraftment, we tracked these cells in vivo using mice pretreated with naphthalene. Naphthalene causes lung injury mainly to distal bronchiolar club cells without significantly depleting alveolar epithelial cells in the mouse.[66,67] As shown in Fig. 1.1.5, mice received either normal saline or 275 mg/kg naphthalene, intraperitoneally; 2 days later, the FND-labeled LSCs were injected into lung-injured or control mice via i.v. administration. Mice were

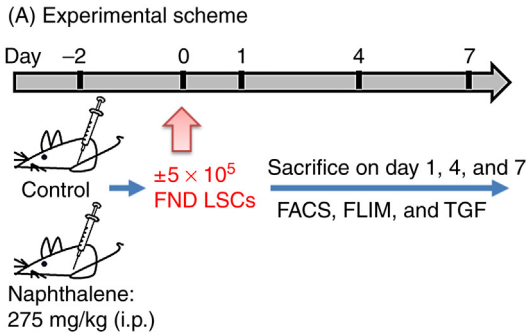

(C) % of the transplanted stem cells engrafted to the lung (P_h)

Mouse lung	Time	P_h	$= N_v$	$\times$	P_s/N_t
Uninjured	Day 1	22%	7×10^6	1.6%	5×10^5
	Day 7	1.4%		0.12%	
Injured	Day 1	14%		0.91%	
	Day 7	11%		0.8%	

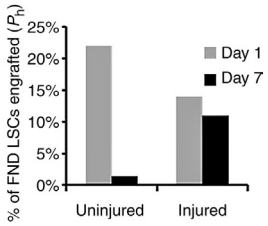

FIGURE 1.1.5 FND-Labeled LSCs in Lung-Injured Mice.

(A) Experimental scheme for tracking the engraftment and regenerative potential of the transplanted LSCs using FNDs. (B) FLIM, TGF, and bright-field H&E staining images reveal that the FND-labeled LSCs reside preferentially at the BADJs of lungs in naphthalene-injured mice after intravenous (i.v.) transplantation (*white and black arrows*). (C) To provide a semiquantitative estimate for the stem cell–homing efficiency, we calculate the percentage (P_h) of the transplanted FND-labeled LSCs homing to lung based on the total number (N_v) of viable (PI^-) cells isolated from mouse lung tissue, the percentage (P_s) of the FND-labeled cells in FACS analysis, and the number (N_t) of cells actually transplanted as $P_h = (N_v \times P_s)/N_t$.[68] Details are described in the text. *i.p.*, Intraperitoneal.

Adapted from Fig. 4 in Wu TJ, Tzeng YK, Chang WW, Cheng CA, Kuo Y, Chien CH, et al. Tracking the engraftment and regenerative capabilities of transplanted lung stem cells using fluorescent nanodiamonds. Nat Nanotechnol *2013;**8**(9):682–9.*[25]

sacrificed at different time points and organs were collected to search for the injected LSCs by fluorescence microscopy (Fig. 1.1.5A). As mentioned, the high-autofluorescence background prevented clear identification of these cells in the lungs. Thanks to the distinct fluorescence lifetime of the NV^- center, this undesirable effect could be largely removed with FLIM and TGF. Fig. 1.1.5B shows FLIM images of the lung tissue collected on day 7. The injected cells can be clearly discerned, even when the cells are stained with H&E to aid histological examination (Fig. 1.1.5B, arrows). First, the FND-labeled LSCs preferentially reside at the terminal bronchioles of the lungs on day 7 after i.v. administration, which was confirmed by TGF imaging of the tissue sections of naphthalene-injured mice with single-cell resolution (Fig. 1.1.5B).

Additionally, the damaged lung cells can rapidly recover after transplantation of the FND-labeled LSCs into the mice, as shown by the increase in pan-cytokeratin (Pan-CK^+) and $CCSP^+$ epithelial cells (Fig. 1.1.3).

An important implication of the present study is that the prospectively isolated LSCs are potentially useful as a new cell source for stem cell–based therapy in regenerative medicine. In such experiments, injury and repair of the bronchiolar epithelium were assessed by immunostaining of the club cells specific marker, CCSP, on day 1 and 7 after injury and injection. It was found that on day 1, the bronchiolar epithelium of lung-injured mice was sparsely surrounded by cells expressing CCSP in both the control (saline-treated) and FND LSC-treated mouse groups. On day 7, although some progress of club cell regeneration occurred in the saline-treated mice, the bronchiolar epithelium of the FND LSC-treated mice displayed a significantly enhanced repopulation of club cells and CCSP staining (Fig. 1.1.3).[25] The almost complete restoration of club cells suggests that the transplanted FND-labeled LSCs are involved in lung repair and homeostasis. The suggestion was additionally supported by flow cytometric identification of SSC^+Far-red^+ cells, which revealed that from day 1 up to day 7 after LSC injection in the injury mice, approximately 0.8–0.91% of the total population of viable cells was associated with FND-labeled LSCs in the lungs. In other words, the percentage of the FND-labeled LSCs did not show any pronounced decrease for an entire week after naphthalene treatment (Fig. 1.1.5B),[25] a situation totally differing from that of the uninjured mice. This discrepancy in the results between the experiments with uninjured and injured mice demonstrated the homing capacity of the FND-labeled LSCs.

Last, lung tissue sections prepared from mice on day 1 and day 7 after injection of FND-labeled LSCs were stained with H&E for morphological analysis. Again, TGF images showed that the FND-labeled LSCs were preferentially localized in terminal bronchioles of lung-injured mice. Moreover, using FLIM image, immunohistochemistry for epithelial marker Pan-CK and Clare cell marker (CCSP), it was found that the FND-labeled cells were located at epithelium regions (Fig. 1.1.3). The increase of the FND-labeled LSC population in bronchioles, together with the fluorescence images, is a reflection that the LSCs preferentially home to the terminal bronchioles or BADJs in lung-injured mice.

It is known that lung epithelium slowly turns over in a normal condition, its regenerative capacity could be activated after injury.[69] Similarly, bone marrow transplantation also requires the specific myeloablative conditioning of recipients to create "space" for accommodation of hematopoietic stem cells from donor.[70] In our lung injury experiment, the epithelium was restored more rapidly after transplantation of the FND-labeled cells in the injured model. Furthermore, to provide a semiquantitative estimate for the stem cell–homing efficiency, we calculate the proportion of the FND-labeled cells that homed to lung (P_h) with the following equation, $[(N_v \times P_s)/N_t] \times 100\%$,[68] where N_v equals the percent of FND-labeled cells determined by flow cytometry, P_s equals the total number of cells in the lung, and N_t equals the number of cells actually transplanted (Fig. 1.1.5C). In our experiment, the number of FND-labeled cells transplanted to mice in each experiment was 5×10^5. The

total number of cells isolated from mouse lung tissue was approximately 10^7 cells, of which about 70% were viable cells (PI^-). Moreover, the $SSC^+Far\text{-}red^+$ cells (i.e., the FND-labeled cells) in the PI^- gate was 1.6% on day 1, which declined to 0.12% on day 7 in normal (uninjured) mice. Thus, the proportion of the transplanted cells that homed to lung (P_h) could be estimated as $[1.6\% \times (10^7 \times 70\%)/5 \times 10^5] = 22\%$. Similar calculation resulted in the decrease of the proportion of the transplanted cells that remained in lung to become 1.4% (i.e., $[0.12\% \times (10^7 \times 70\%)/5 \times 10^5] = 1.4\%$. Therefore, in normal (uninjured) mice, there was a significant decrease of the value from 22% of the transplanted cells in the lung on day 1 to 1.4% on day 7 (Fig. 1.1.5C). In other words, most of the transplanted cells initially entrapped in the lung had now disappeared from the lung on day 7. In sharp contrast, similar calculations for the lung injury model revealed that the proportion of the transplanted FND-labeled cells that homed to lung did not show significant decrease after 7 days (i.e., 14% on day 1 and 11% on day 7) (Fig. 1.1.5C). These results seemed to imply that the lodgment of the transplanted FND-labeled cells in injured model is indicative of "proactive" homing, but not nonspecific (or passive) entrapment.

The use of LSCs for stem cell therapies relies on the homing capacity and long-term engraftment of these cells to the appropriate niches of lung tissues. Although the mechanisms by which the prospectively isolated LSCs reach lung tissues and further home to the BADJs upon i.v. transplantation are not yet fully understood,[71] it is speculated that CXCR4 plays a crucial role in these processes. A previous study has found that CXCR4/CXCL12 are markers essential for stem cell homing and recruitment of circulating epithelial progenitor cells to the specific site of airway injury.[72] In this study, CXCR4 was indeed expressed on $CD45^-CD54^+CD157^+$ cells and in colony cells under serum free–selective culture, suggesting that the marker may also facilitate homing of these cells to the regenerating epithelium after transplantation.[25]

8 CONCLUSIONS

TGF imaging of the tissue sections of naphthalene-injured mice indicated that FND-labeled LSCs preferentially reside at terminal bronchioles of the lungs after i.v. injection. Our results demonstrated not only the feasibility of finding rare stem cells in vivo with this innovative FND–FLIM imaging technology, but also the engraftment capacity and regenerative potential of the prospectively isolated LSCs. In uninjured mice, there was a significant decrease of the transplanted cells detected in lung on day 1 to a very low level on day 7. It seemed that most of the transplanted cells were initially entrapped in the lung and now had disappeared from the lung on day 7. In contrast, similar calculations for the lung injury model revealed that the proportion of the transplanted FND-labeled cells homed to lung did not show significant changes after 7 days. Our results thus imply that the lodgment of the transplanted FND-labeled cells in injured model is indicative of "proactive" homing, but not nonspecific (or passive) entrapment. Notably, the fact that lung repair in injury mice became

significantly enhanced through the injection of LSCs implied the feasibility of cell therapy for regenerative medicine.

Therefore, here we have presented a nanoparticle-based platform that combines FND labeling, FACS, FLIM, TGF imaging, and immunostaining to assess the tissue-specific engraftment and regenerative potential of stem cells transplanted in vivo. Moreover, these approaches should offer new insights into the components that limit the acceptance of the transplanted stem cells in vivo, as well as the mechanism of their regeneration within a host. Nanotechnology holds great potential for monitoring the homing of different kinds of stem cells for preclinical experimentation and thus is an enabling technology for applications in stem cell research and regenerative medicine.

ACKNOWLEDGMENTS

This work was supported by grants of the Ministry of Science and Technology, Taiwan (MOST103-2321-B-182A-003 and MOST104-2321-B-182A-001) and Chang Gung Medical Foundation (OMRPG3C0043 and OMRPG3C0044) for John Yu.

REFERENCES

1. Accomasso L, Gallina C, Turinetto V, Giachino C. Stem cell tracking with nanoparticles for regenerative medicine purposes: an overview. *Stem Cells Int* 2016;**2016**:7920358.
2. Solanki A, Kim JD, Lee KB. Nanotechnology for regenerative medicine: nanomaterials for stem cell imaging. *Nanomedicine* 2008;**3**(4):567–78.
3. Jackson KA, Snyder DS, Goodell MA. Skeletal muscle fiber-specific green autofluorescence: potential for stem cell engraftment artifacts. *Stem Cells* 2004;**22**(2):180–7.
4. Brambrink T, Foreman R, Welstead GG, Lengner CJ, Wernig M, Suh H, et al. Sequential expression of pluripotency markers during direct reprogramming of mouse somatic cells. *Cell Stem Cell* 2008;**2**(2):151–9.
5. Frangioni JV, Hajjar RJ. In vivo tracking of stem cells for clinical trials in cardiovascular disease. *Circulation* 2004;**110**(21):3378–83.
6. Kircher MF, Gambhir SS, Grimm J. Noninvasive cell-tracking methods. *Nat Rev Clin Oncol* 2011;**8**(11):677–88.
7. Ferreira L, Karp JM, Nobre L, Langer R. New opportunities: the use of nanotechnologies to manipulate and track stem cells. *Cell Stem Cell* 2008;**3**(2):136–46.
8. Liu YS, Sun Y, Vernier PT, Liang CH, Chong SY, Gundersen MA. pH-Sensitive photoluminescence of CdSe/ZnSe/ZnS quantum dots in human ovarian cancer cells. *J Phys Chem C* 2007;**111**(7):2872–8.
9. Sasaki F, Miyamoto T, Yamamoto A, Tamai Y, Yajima T. Morphological and genetic characteristics of the entomopathogenic fungus *Ophiocordyceps nutans* and its host insects. *Mycol Res* 2008;**112**(Pt. 10):1241–4.
10. Pi QM, Zhang WJ, Zhou GD, Liu W, Cao Y. Degradation or excretion of quantum dots in mouse embryonic stem cells. *BMC Biotechnol* 2010;**10**:36.
11. Rosen AB, Kelly DJ, Schuldt AJ, Lu J, Potapova IA, Doronin SV, et al. Finding fluorescent needles in the cardiac haystack: tracking human mesenchymal stem cells labeled with

quantum dots for quantitative in vivo three-dimensional fluorescence analysis. *Stem Cells* 2007;**25**(8):2128–38.
12. Yu SJ, Kang MW, Chang HC, Chen KM, Yu YC. Bright fluorescent nanodiamonds: no photobleaching and low cytotoxicity. *J Am Chem Soc* 2005;**127**(50):17604–5.
13. Fu CC, Lee HY, Chen K, Lim TS, Wu HY, Lin PK, et al. Characterization and application of single fluorescent nanodiamonds as cellular biomarkers. *Proc Natl Acad Sci USA* 2007;**104**(3):727–32.
14. Chang YR, Lee HY, Chen K, Chang CC, Tsai DS, Fu CC, et al. Mass production and dynamic imaging of fluorescent nanodiamonds. *Nat Nanotechnol* 2008;**3**(5):284–8.
15. Boudou JP, Curmi PA, Jelezko F, Wrachtrup J, Aubert P, Sennour M, et al. High yield fabrication of fluorescent nanodiamonds. *Nanotechnology* 2009;**20**(23):235602.
16. McGuinness LP, Yan Y, Stacey A, Simpson DA, Hall LT, Maclaurin D, et al. Quantum measurement and orientation tracking of fluorescent nanodiamonds inside living cells. *Nat Nanotechnol* 2011;**6**(6):358–63.
17. Mohan N, Chen CS, Hsieh HH, Wu YC, Chang HC. In vivo imaging and toxicity assessments of fluorescent nanodiamonds in *Caenorhabditis elegans*. *Nano Lett* 2010;**10**(9):3692–9.
18. Mochalin VN, Shenderova O, Ho D, Gogotsi Y. The properties and applications of nanodiamonds. *Nat Nanotechnol* 2012;**7**(1):11–23.
19. Vaijayanthimala V, Chang HC. Functionalized fluorescent nanodiamonds for biomedical applications. *Nanomedicine* 2009;**4**(1):47–55.
20. Kaur R, Badea I. Nanodiamonds as novel nanomaterials for biomedical applications: drug delivery and imaging systems. *Int J Nanomed* 2013;**8**:203–20.
21. Faklaris O, Garrot D, Joshi V, Druon F, Boudou JP, Sauvage T, et al. Detection of single photoluminescent diamond nanoparticles in cells and study of the internalization pathway. *Small* 2008;**4**(12):2236–9.
22. Berezin MY, Achilefu S. Fluorescence lifetime measurements and biological imaging. *Chem Rev* 2010;**110**(5):2641–84.
23. Resch-Genger U, Grabolle M, Cavaliere-Jaricot S, Nitschke R, Nann T. Quantum dots versus organic dyes as fluorescent labels. *Nat Methods* 2008;**5**(9):763–75.
24. Chang CW, Sud D, Mycek MA. Fluorescence lifetime imaging microscopy. *Method Cell Biol* 2007;**81**:495–524.
25. Wu TJ, Tzeng YK, Chang WW, Cheng CA, Kuo Y, Chien CH, et al. Tracking the engraftment and regenerative capabilities of transplanted lung stem cells using fluorescent nanodiamonds. *Nat Nanotechnol* 2013;**8**(9):682–9.
26. Schrand AM, Huang H, Carlson C, Schlager JJ, Omacr Sawa E, Hussain SM, et al. Are diamond nanoparticles cytotoxic? *J Phys Chem B* 2007;**111**(1):2–7.
27. Xing Y, Xiong W, Zhu L, Osawa E, Hussin S, Dai L. DNA damage in embryonic stem cells caused by nanodiamonds. *ACS Nano* 2011;**5**(3):2376–84.
28. Liu KK, Wang CC, Cheng CL, Chao JI. Endocytic carboxylated nanodiamond for the labeling and tracking of cell division and differentiation in cancer and stem cells. *Biomaterials* 2009;**30**(26):4249–59.
29. Lien ZY, Hsu TC, Liu KK, Liao WS, Hwang KC, Chao JI. Cancer cell labeling and tracking using fluorescent and magnetic nanodiamond. *Biomaterials* 2012;**33**(26):6172–85.
30. Schrand AM, Lin JB, Hens SC, Hussain SM. Temporal and mechanistic tracking of cellular uptake dynamics with novel surface fluorophore-bound nanodiamonds. *Nanoscale* 2011;**3**(2):435–45.
31. Vaijayanthimala V, Tzeng YK, Chang HC, Li CL. The biocompatibility of fluorescent nanodiamonds and their mechanism of cellular uptake. *Nanotechnology* 2009;**20**(42):425103.

32. Fang CY, Vaijayanthimala V, Cheng CA, Yeh SH, Chang CF, Li CL, et al. The exocytosis of fluorescent nanodiamond and its use as a long-term cell tracker. *Small* 2011;**7**(23):3363–70.
33. Yuan Y, Wang X, Jia G, Liu JH, Wang TC, Gu YQ, et al. Pulmonary toxicity and translocation of nanodiamonds in mice. *Diam Relat Mater* 2010;**19**(4):291–9.
34. Vaijayanthimala V, Cheng PY, Yeh SH, Liu KK, Hsiao CH, Chao JI, et al. The long-term stability and biocompatibility of fluorescent nanodiamond as an in vivo contrast agent. *Biomaterials* 2012;**33**(31):7794–802.
35. Chow EK, Zhang XQ, Chen M, Lam R, Robinson E, Huang H, et al. Nanodiamond therapeutic delivery agents mediate enhanced chemoresistant tumor treatment. *Sci Transl Med* 2011;**3**(73):73ra21.
36. Simpson DA, Thompson AJ, Kowarsky M, Zeeshan NF, Barson MS, Hall LT, et al. In vivo imaging and tracking of individual nanodiamonds in *Drosophila melanogaster* embryos. *Biomed Opt Express* 2014;**5**(4):1250–61.
37. Hsiao WW, Hui YY, Tsai PC, Chang HC. Fluorescent nanodiamond: a versatile tool for long-term cell tracking, super-resolution imaging, and nanoscale temperature sensing. *Acc Chem Res* 2016;**49**(3):400–7.
38. Kotton DN, Morrisey EE. Lung regeneration: mechanisms, applications and emerging stem cell populations. *Nat Med* 2014;**20**(8):822–32.
39. Li F, He J, Wei J, Cho WC, Liu X. Diversity of epithelial stem cell types in adult lung. *Stem Cells Int* 2015;**2015**:728307.
40. Mercer RR, Russell ML, Roggli VL, Crapo JD. Cell number and distribution in human and rat airways. *Am J Respir Cell Mol Biol* 1994;**10**(6):613–24.
41. Ballard ST, Inglis SK. Liquid secretion properties of airway submucosal glands. *J Physiol* 2004;**556**(Pt. 1):1–10.
42. Van Lommel A. Pulmonary neuroendocrine cells (PNEC) and neuroepithelial bodies (NEB): chemoreceptors and regulators of lung development. *Paediatr Respir Rev* 2001;**2**(2):171–6.
43. Morrisey EE, Hogan BL. Preparing for the first breath: genetic and cellular mechanisms in lung development. *Dev Cell* 2010;**18**(1):8–23.
44. Rawlins EL, Clark CP, Xue Y, Hogan BL. The $Id2^+$ distal tip lung epithelium contains individual multipotent embryonic progenitor cells. *Development* 2009;**136**(22):3741–5.
45. Rawlins EL, Hogan BL. Ciliated epithelial cell lifespan in the mouse trachea and lung. *Am J Physiol Lung Cell Mol Physiol* 2008;**295**(1):L231–4.
46. Giangreco A, Arwert EN, Rosewell IR, Snyder J, Watt FM, Stripp BR. Stem cells are dispensable for lung homeostasis but restore airways after injury. *Proc Natl Acad Sci USA* 2009;**106**(23):9286–91.
47. Rawlins EL, Okubo T, Xue Y, Brass DM, Auten RL, Hasegawa H, et al. The role of Scgb1a1$^+$ Clara cells in the long-term maintenance and repair of lung airway, but not alveolar, epithelium. *Cell Stem Cell* 2009;**4**(6):525–34.
48. Hong KU, Reynolds SD, Watkins S, Fuchs E, Stripp BR. In vivo differentiation potential of tracheal basal cells: evidence for multipotent and unipotent subpopulations. *Am J Physiol Lung Cell Mol Physiol* 2004;**286**(4):L643–9.
49. Schoch KG, Lori A, Burns KA, Eldred T, Olsen JC, Randell SH. A subset of mouse tracheal epithelial basal cells generates large colonies in vitro. *Am J Physiol Lung Cell Mol Physiol* 2004;**286**(4):L631–42.
50. Rock JR, Onaitis MW, Rawlins EL, Lu Y, Clark CP, Xue Y, et al. Basal cells as stem cells of the mouse trachea and human airway epithelium. *Proc Natl Acad Sci USA* 2009;**106**(31):12771–5.

51. Rock JR, Randell SH, Hogan BL. Airway basal stem cells: a perspective on their roles in epithelial homeostasis and remodeling. *Dis Model Mech* 2010;**3**(9–10):545–56.
52. Kajstura J, Rota M, Hall SR, Hosoda T, D'Amario D, Sanada F, et al. Evidence for human lung stem cells. *N Engl J Med* 2011;**364**(19):1795–806.
53. Engelhardt JF, Schlossberg H, Yankaskas JR, Dudus L. Progenitor cells of the adult human airway involved in submucosal gland development. *Development* 1995;**121**(7): 2031–46.
54. Hong KU, Reynolds SD, Giangreco A, Hurley CM, Stripp BR. Clara cell secretory protein-expressing cells of the airway neuroepithelial body microenvironment include a label-retaining subset and are critical for epithelial renewal after progenitor cell depletion. *Am J Respir Cell Mol Biol* 2001;**24**(6):671–81.
55. Giangreco A, Reynolds SD, Stripp BR. Terminal bronchioles harbor a unique airway stem cell population that localizes to the bronchoalveolar duct junction. *Am J Pathol* 2002;**161**(1):173–82.
56. Kim CF, Jackson EL, Woolfenden AE, Lawrence S, Babar I, Vogel S, et al. Identification of bronchioalveolar stem cells in normal lung and lung cancer. *Cell* 2005;**121**(6): 823–35.
57. Hoffman AM, Ingenito EP. Alveolar epithelial stem and progenitor cells: emerging evidence for their role in lung regeneration. *Curr Med Chem* 2012;**19**(35):6003–8.
58. Oeztuerk-Winder F, Ventura JJ. Isolation, culture, and potentiality assessment of lung alveolar stem cells. *Methods Mol Biol* 2012;**916**:23–30.
59. Ling TY, Kuo MD, Li CL, Yu AL, Huang YH, Wu TJ, et al. Identification of pulmonary Oct-4^{+} stem/progenitor cells and demonstration of their susceptibility to SARS coronavirus (SARS-CoV) infection in vitro. *Proc Natl Acad Sci USA* 2006;**103**(25):9530–5.
60. Teisanu RM, Lagasse E, Whitesides JF, Stripp BR. Prospective isolation of bronchiolar stem cells based upon immunophenotypic and autofluorescence characteristics. *Stem Cells* 2009;**27**(3):612–22.
61. Raiser DM, Kim CF. Commentary: Sca-1 and cells of the lung: a matter of different sorts. *Stem Cells* 2009;**27**(3):606–11.
62. Teisanu RM, Chen H, Matsumoto K, McQualter JL, Potts E, Foster WM, et al. Functional analysis of two distinct bronchiolar progenitors during lung injury and repair. *Am J Respir Cell Mol Biol* 2011;**44**(6):794–803.
63. Liang YJ, Kuo HH, Lin CH, Chen YY, Yang BC, Cheng YY, et al. Switching of the core structures of glycosphingolipids from globo- and lacto- to ganglio-series upon human embryonic stem cell differentiation. *Proc Natl Acad Sci USA* 2010;**107**(52):22564–9.
64. Cho HC, Liao CH, Yu AL, Yu J. Surface markers in stem cells and cancer from the perspective of glycomic analysis. *Int J Biol Markers* 2012;**27**(4):e344–52.
65. Sawa M, Hsu TL, Itoh T, Sugiyama M, Hanson SR, Vogt PK, et al. Glycoproteomic probes for fluorescent imaging of fucosylated glycans in vivo. *Proc Natl Acad Sci USA* 2006;**103**(33):12371–6.
66. Van Winkle LS, Buckpitt AR, Nishio SJ, Isaac JM, Plopper CG. Cellular response in naphthalene-induced Clara cell injury and bronchiolar epithelial repair in mice. *Am J Physiol* 1995;**269**(6 Pt. 1):L800–18.
67. Stripp BR, Maxson K, Mera R, Singh G. Plasticity of airway cell proliferation and gene expression after acute naphthalene injury. *Am J Physiol Lung C* 1995;**269**(6):L791–9.
68. Szilvassy SJ, Meyerrose TE, Ragland PL, Grimes B. Differential homing and engraftment properties of hematopoietic progenitor cells from murine bone marrow, mobilized peripheral blood, and fetal liver. *Blood* 2001;**98**(7):2108–15.

69. Kauffman SL. Cell proliferation in the mammalian lung. *Int Rev Exp Pathol* 1980;**22**: 131–91.
70. Craddock C. Haemopoietic stem-cell transplantation: recent progress and future promise. *Lancet Oncol* 2000;**1**:227–34.
71. Chavakis E, Urbich C, Dimmeler S. Homing and engraftment of progenitor cells: a prerequisite for cell therapy. *J Mol Cell Cardiol* 2008;**45**(4):514–22.
72. Gomperts BN, Belperio JA, Rao PN, Randell SH, Fishbein MC, Burdick MD, et al. Circulating progenitor epithelial cells traffic via CXCR4/CXCL12 in response to airway injury. *J Immunol* 2006;**176**(3):1916–27.

SUBCHAPTER 1.2

Antiretroviral drug–loaded nanosystems for preventing HIV transmission

Mafalda P. Cautela*,, Bruno Sarmento*,**, José das Neves*,****

**i3S—Instituto de Investigação e Inovação em Saúde, Universidade do Porto, Porto, Portugal;*
***INEB—Instituto de Engenharia Biomédica, Universidade do Porto, Porto, Portugal*

1 INTRODUCTION

The human immunodeficiency virus (HIV), the causative agent of human acquired immunodeficiency syndrome (AIDS), is at the epicenter of a global epidemic affecting millions of people.[1] This constitutes a major problem, especially in developing countries of sub-Saharan Africa, where prevalence and transmission rates are higher and access to treatment and prevention are still limited.[2] Current treatment relies on the use of multiple antiretroviral drugs that can inhibit different steps of the virus infection cycle. Combination antiretroviral therapy (cART) is able to improve the health of patients particularly when started early after infection, but lifelong treatment is required.[3,4] Therapeutic regimens are often hard to implement, especially when considering the poor patient adherence and side effects.[5]

As a feasible cure of HIV infection is unlikely to be available in the near future, control of the epidemic relies largely on preventive interventions.[6,7] Among those recently proven effective, oral pre-exposure prophylaxis (PrEP)—already approved in several countries, such as the United States, Canada, and France—and topical microbicides (also referred to as topical PrEP) may be particularly promising to fulfill unmet needs in averting new infections.[8] Despite the exciting results of oral PrEP in men who have sex with men, protection among heterosexual women has been shown

inconsistent.[9] Issues related with poor adherence or biological differences between routes of transmission (vaginal vs. rectal) may be involved. Also, oral PrEP can be limited by the onset of systemic adverse effects as also typically seen with cART. Topical microbicides have struggled throughout roughly the last quarter of a century to achieve proof of concept in human clinical trials, but recent successes may boost further investment in their development and market introduction. The dapivirine vaginal ring is at the forefront, but other products will likely rise in coming years.[10] Rectal microbicides are also under development, but advances have been slower.[11]

It is recognized that drug formulation and delivery plays an important role in developing topical microbicides.[12] Many strategies involving the use of more conventional dosage forms or novel delivery systems have been proposed and tested for various anti-HIV compounds. This subchapter describes recent developments in the field of nanotechnology-based carrier systems for the delivery of antiretroviral compounds and for the purpose of topical prevention of sexual HIV transmission.

2 BASICS ON HIV INFECTION AND TOPICAL MICROBICIDES

The UNAIDS estimates that around 36.7 million people worldwide were living with HIV by the end of 2015, while 2.1 million became newly infected during that single year.[13] Type 1 virus (HIV-1) accounts for most cases, as it is easier to transmit and more virulent than type 2 HIV.[6] Transmission may occur through sexual, blood, or vertical (mother-to-child) contacts, although the majority of the infection burden arises from unprotected sex.[14] When at the cervicovaginal or rectal mucosae, the virus can exploit several pathways to reach its main target cells, namely $CD4^+$ cells.[15] HIV can also infect other cells, such as macrophages and dendritic cells (DCs). Fig. 1.2.1 presents a schematic representation of the main mechanisms and possible pathways behind transmission at the cervicovaginal mucosa.[16]

Lack of a cure for HIV/AIDS makes prevention an essential approach in the fight against the epidemic. While an effective vaccine is still elusive,[17] several modalities are currently available and have been proven as, at least, partially effective (Table 1.2.1).[18,19] However, large-scale implementation of preventive measures has been shown to be a huge challenge requiring further investment, namely on novel strategies. Avoiding sexual transmission in particular is urgently needed. Alongside oral PrEP with antiretroviral drugs, the possibility of delivering anti-HIV compounds by the vaginal and/or rectal routes has attracted considerable attention.[20,21] Microbicides can be defined as products for vaginal and/or rectal delivery that can block early viral transmission events at the mucosal level. Microbicides are considered particularly important, as they may represent a means for women at risk to protect themselves without the need of consent, cooperation, or even knowledge of the male partner. Even if unlikely to confer full protection, microbicides may still have an important role in averting HIV infection when combined with other preventive strategies.[22] Contrary to oral PrEP, antiretroviral drugs are intended to concentrate at mucosae and do not reach systemic circulation in significant levels, thus contributing to ameliorate adverse effects. The development of

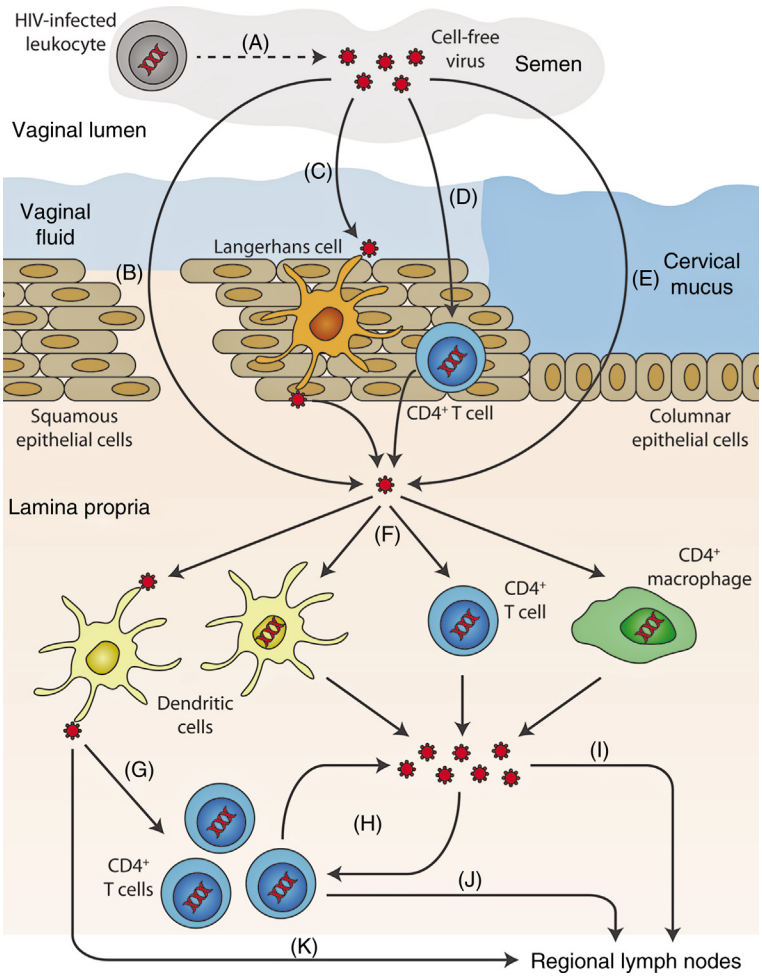

FIGURE 1.2.1 Mechanisms of Sexual Transmission of Cell-Free Human Immunodeficiency Virus (HIV) Through the Cervicovaginal Route.

Upon ejaculation, HIV present in semen or (A) produced in loco by donor HIV-infected leukocytes requires to first cross mucus fluids covering mucosae. Then, viral particles can surpass the epithelial barrier by different pathways: (B) direct access to the lamina propria across gaps in the epithelium, (C) capture and transepithelial transport of virions by Langerhans cells, (D) partial penetration of the epithelium and infection of intraepithelial $CD4^+$ T cells (or other leukocytes) that then migrate to the lamina propria, or (E) epithelial crossing through intercellular spaces or by transcytosis. Once in the lamina propria, (F) HIV can productively infect target cells, such as macrophages, $CD4^+$ T cells, or dendritic cells (DCs). (G) DCs can also mediate transinfection of other target cells, namely $CD4^+$ T cells. Upon initial infection of target cells, (H) local viral amplification occurs mainly in $CD4^+$ T cells before migration of (I) the free virus and/or (J) infected cells to regional lymph nodes. (K) Transfer of HIV to lymph nodes can also be mediated in *trans* by nonproductively infected DCs.

Reprinted from das Neves J, Nunes R, Rodrigues F, Sarmento B. Nanomedicine in the development of anti-HIV microbicides. Adv Drug Deliv Rev *2016;**103**:57–75.*[16] *Copyright 2016 Elsevier.*

Table 1.2.1 Preventive Measures for Sexual HIV Transmission With Main Advantages and Disadvantages[18,19]

Preventive Measures	Advantages	Disadvantages
Condom use	The most effective for preventing HIV sexual transmission	Adherence is far from perfect
		Requires partner consent (difficult to negotiate in several settings)
	Inexpensive and easy to use	
	Widely available	Dependent on coitus
Sociobehavioral interventions (e.g., monogamy, sexual abstinence, counseling, and regular testing for infection)	Usually require limited resources to be implemented	Difficult to implement, namely in large scale
	Not dependent on coitus	Difficult to implement in setting prevailing gender inequality
Medical male circumcision	Relatively high protection obtained after one single surgical intervention	Requires appropriate medical facilities and specialized staff
		Does not protect women
	Not dependent on coitus	Only partially effective
Testing for HIV infection	Reduces the probability of risky sexual intercourse	May not be readily available
		Possibility of false results
Antiretroviral treatment of HIV-positive individuals	Reduces risk of transmission to uninfected partner	Requires lifelong treatment and monitoring
	Beneficial to infected partner (significantly suppresses viral replication and reduces viral load)	Toxicity issues may compromise success
		Costly (still unavailable in many low-resource settings)
	Not dependent on coitus	
Oral PrEP	Highly effective, particularly in men who have sex with men, if used consistently	Requires near-perfect adherence and long-term use
		Contradictory results in the case of women
	Not dependent on coitus	Costly
		Toxicity issues may arise

PeEP, Pre-exposure prophylaxis.

products intended to circumvent anogenital mucosal transmission of the virus received a much needed boost with the recent release of the results of two phase 3 clinical trials testing a dapivirine vaginal ring.[23,24] Still, this tentative microbicide product was shown to be only mildly effective, reducing the transmission from men to women by 27%–31% as compared to the placebo ring. These results were in line with those of a tenofovir gel tested in the CAPRISA 004 phase 2b clinical trial, the first and only other study showing protection for vaginal microbicides.[25] Combined, the partial success of these trials suggests that additional work in developing novel solutions may be useful for potentially improving efficacy of microbicides. As for rectal microbicides, development is still in earlier stages, and human efficacy studies have not been conducted yet.[26]

Once considered an issue of lesser relevance, microbicide drug formulation has taken an essential place during development by its own.[12] Formulation efforts should

lead to stable, safe, and potentially effective products that should also be accepted by users. Presently, it is well established that a relationship between pharmacokinetics (PK) and pharmacodynamics exists for several microbicide drugs, namely dapivirine and tenofovir, by which higher local concentrations are related with enhanced protection.[27,28] Adequate design of vaginal and rectal products may contribute to increased and sustained drug levels. Most products developed so far rely on conventional dosage forms, particularly gels. These are considered practical and cheap to manufacture, but limitations exist, such as potentially poor physicochemical and microbiological stability, alongside issues concerning leakage and messiness upon administration.[29] Moreover, the use of gels is coitus dependent, that is, products require to be administered immediately before and/or after every sexual intercourse to be effective. This raises issues concerning adherence and has been regarded as one of the most challenging topics influencing the efficacy of microbicides.[30] Other dosage forms have also been considered, namely tablets, capsules, suppositories, creams, solutions, suspensions, and foams,[31] but the advances in development have been slow, presumably because no or limited advantages exist when compared to gels. Vaginal films are seen as an interesting alternative dosage form to gels, namely due to their compact size, increased stability, and decreased ability to cause vaginal leakage.[32] In particular, a film containing dapivirine has been tested recently in a phase 1 clinical trial, and results suggested that it was safe and provided potentially protective genital drug levels.[33] However, films are not suitable for rectal administration and, alongside other more conventional dosage forms, are limited by the need to be administered every time sexual intercourse occurs. Vaginal rings have been engineered to deliver different antiretroviral drugs for use as coitus-independent microbicides.[34] Once placed in the vagina, rings can release drugs in a sustained fashion for up to several weeks or even months. Notwithstanding the potential to abbreviate adherence issues, the dapivirine ring provided only modest protection to women, as described before in this subchapter. More data are required to fully understand such results, but frequent ring removal, particularly around the time of sexual intercourse, is a possible explanation.[35]

Another important aspect that needs to be stressed concerns the specificity of the vaginal and rectal routes. As mentioned before, some dosage forms are route specific, namely rings and films. Apart from that, the biology of the vaginal and rectal milieu require to be considered to meet requirements of safety, administration, distribution, and overall local PK. Description of the main characteristics of the vagina and colorectum is beyond the scope of this manuscript. Details on the main anatomical, histological, and physiological features of both these routes, with particular relevance to the development of microbicides, can be found in previous publications by our research group.[26,36,37]

3 MICROBICIDES AND NANOTECHNOLOGY

Advances in the field of nanomedicine have been tremendous over the last decades, with several nanotechnology-based drug products already reaching markets worldwide.[38] Such encouraging achievements boosted interest in applying nanotechnology

to healthcare and the field of HIV treatment and prevention was no exception.[39,40] Development of nanomicrobicides has been receiving increasing interest but, as in the case of more conventional drug delivery approaches, mostly for providing protection from vaginal HIV transmission. Microbicide nanosystems may be conveniently classified as those possessing inherent activity, either by interacting directly with HIV or blocking virus–host cell interactions, and those acting as carriers for anti-HIV compounds.[41] In the first case, dendrimers have been the focus of extensive development.[42] In particular, the SPL7013 dendrimer has been formulated as a gel (VivaGel; Starpharma, Abbotsford, Victoria, Australia) and tested as a vaginal microbicide. This fourth-generation dendrimer comprises polylysine branches attached to a central core of benzhydrylamine amide. Polylysines are terminally derivatized with naphthalene disulfonate groups, which are responsible for interacting with HIV-1, particularly with gp-120.[43] Viral gp-120 is an envelope glycoprotein that plays a crucial role in infection by binding to the CD4 receptor and one coreceptor (CCR5 or CXCR4) present in host cell membranes.[44] VivaGel underwent a series of promising clinical trials,[45,46] but the possible onset of safety issues seems to have halted its development as a microbicide product.[47,48] The use of gels formulated for the rectal delivery of SPL7013 has also been explored.[49] Recently, various carbosilane dendrimers have been proposed as a promising alternative and in vitro and in vivo data seem to attest their potential.[50]

Over roughly the last decade, research in nanotechnology-based microbicides has mainly focused on the development of nanocarriers for promising anti-HIV compounds, namely antiretroviral drugs already tested in clinical trials. Following release of the results of the CAPRISA 004 trial, tenofovir and its derivatives became immediate candidates for developing drug-loaded nanosystems. Different types of nanocarriers intended for vaginal delivery have been developed, including solid lipid nanoparticles (SLNs),[51] chitosan and thiolated chitosan nanoparticles (NPs),[52,53] pH-sensitive poly(lactic-*co*-glycolic acid) (PLGA), Eudragit S100 NPs,[54] and hyaluronidase-sensitive hyaluronic acid NPs.[55] Nanofibers loaded with tenofovir have also been recently proposed for developing vaginal microbicides.[56,57] Apart from tenofovir, a wide variety of vaginal nanocarriers have further been developed for other anti-HIV compounds, namely PSC-RANTES–loaded PLGA NPs,[58] dapivirine-loaded polycaprolactone (PCL) NPs,[59] efavirenz/raltegravir-loaded PLGA NPs,[60] efavirenz- or saquinavir-loaded PLGA NPs,[61] saquinavir-loaded CD4-targeted PLGA NPs,[62] dapivirine-loaded PLGA NPs,[63] efavirenz-loaded cellulose acetate phthalate (CAP) NPs,[64] and efavirenz/curcumin-loaded lactoferrin NPs.[65] Overall, advantageous features of using nanosystems for the vaginal delivery of active compounds may include controlled release, enhanced solubility, protection of labile molecules, improved distribution throughout the mucosa, modulation of mucoadhesive behavior, improved interactions with host cells (e.g., by leading to higher intracellular drug concentrations or providing targeted drug delivery to HIV-susceptible cells), or enhanced drug penetration/accumulation in genital tissues.[66] One issue that has been the focus of intense research and discussion over the last decade relates with the mucoadhesive behavior of nanosystems.[67,68] Once regarded as advantageous, extensive interaction

with cervicovaginal mucus is now considered as potentially deleterious, as decreased transport of nanosystems can result in poor ability to reach epithelial linings and interact with cells of interest.[69] Different strategies have been described to decrease mucoadhesion,[70] but dense surface modification of NPs with relatively short-chain, linear poly(ethylene oxide) [PEO, also commonly referred to as poly(ethylene glycol)], has been preferential.[71,72]

Research on rectal nanomicrobicides has been nearly nonexistent and much work is still required.[73] The same advantages pointed out earlier for the vaginal administration of nanosystems may apply. For example, data from animal studies and human clinical trials indicate that NPs may be an interesting approach to improve distribution and retention throughout the colorectum, as well as to enhance transport across the mucus barrier.[74,75] Only a few specific studies have been described regarding nanomicrobicides. For example, data from in vitro and ex vivo studies with cells or animal colorectal tissues support that dapivirine-loaded PCL NPs may be successfully engineered to be safe and effective when considering rectal administration.[76] In another study, nanoconjugates of the protease inhibitor amprenavir, PEO, and a cell penetrating peptide (Bac7) were found particularly useful for enhancing drug uptake into colorectal tissue when administered intrarectally to mice.[77]

3.1 MICROBICIDE DRUG NANOCARRIERS

As mentioned earlier, substantial effort has been placed in the development of vaginal nanocarrier systems for compounds that may potentially inhibit transmission at the mucosal level. The next subsection is partially reproduced and updated from a recent review by our group on the subject[16] and describes illustrative case studies of microbicide nanocarriers at advanced preclinical stages of development, with particular focus on their in vivo evaluation.

3.1.1 Dapivirine-loaded PCL nanoparticles

Dapivirine is a diarylpyrimidine compound and one of the lead microbicide drug candidates, currently being evaluated in two phase 3 clinical trials as a vaginal ring. Although possessing potent anti-HIV-1 activity, dapivirine presents some problematic features, namely poor solubility in aqueous vehicles, which limits formulation approaches.[78] Our group has been engaged over the years in developing different polymeric NP carriers as an alternative for the vaginal delivery of dapivirine. These NPs have been extensively evaluated in vitro for stability, toxicity, activity, interaction with various cell types and mucus-like fluids, and cell monolayer/tissue permeability and drug retention.[59,63,76,79–82] For example, PCL NPs have been shown to maintain the antiviral activity of dapivirine upon encapsulation (Fig. 1.2.2), but modulated toxicity differently according to selected particle stabilizer: PEO-modified NPs improved toxicity profile, while the incorporation of sodium lauryl sulfate (SLS) or cetyltrimethylammonium bromide (CTAB) in particle composition did not generally change or increase cytotoxicity, respectively.[59,76] PCL NPs were further shown to penetrate both pig vaginal and rectal mucosae ex vivo (Fig. 1.2.3), while enhancing dapivirine

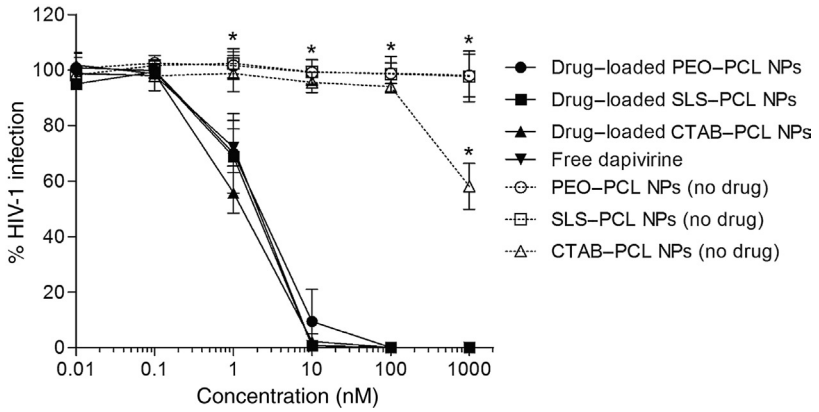

FIGURE 1.2.2 Concentration–Response Inhibition of Viral Infection of TZM-bl Cells by Drug-Loaded Nanoparticles (NPs), Drug-Free NPs, and Free Dapivirine.

Concentration in the *x*-axis is expressed in dapivirine (or virtual dapivirine in the case of NPs with no drug). Each point represents the mean value and bars, the standard deviation ($n = 3$). An *asterisk* denotes a significant difference ($P < 0.05$) when compared with free dapivirine. *CTAB*, Cetyltrimethylammonium bromide; *PCL*, polycaprolactone; *PEO*, poly(ethylene oxide); *SLS*, sodium lauryl sulfate.

Reprinted with permission from das Neves J, Araújo F, Andrade F, Michiels J, Arien KK, Vanham G, et al. In vitro and ex vivo evaluation of polymeric nanoparticles for vaginal and rectal delivery of the anti-HIV drug dapivirine. Mol Pharm *2013;**10**(7):2793–807.*[76] *Copyright 2013 American Chemical Society.*

accumulation at tissues.[76] In particular, a PEO-modified, PCL-based nanoparticulate system presenting mean hydrodynamic diameter around 200 nm emerged as an optimal candidate for the delivery of dapivirine and was further tested in vivo.

PEO–PCL NPs were first evaluated in a mouse model for genital distribution after vaginal instillation in a pH 7.4 phosphate buffered saline (PBS) vehicle (Fig. 1.2.4).[83] Quantitative analysis evidenced rapid removal of NPs from the genital tract (approximately 70 and 90% loss by 30 min and 6 h post-administration, respectively), even if a significant amount of particles was still recovered from vaginal tissues (nearly 10% at 30 min and 5% at 6 h, respectively). Fast particle depletion was associated with the use of PBS instead of a solid or semisolid vehicle that could tackle, at least partially, leakage from the vagina. Noticeably, NPs were still able to penetrate vaginal mucosa to a few tens of micrometers deep (Fig. 1.2.4), thus potentially assuring a drug depot within tissue.[83] Local PK were also assessed up to 24 h post-administration of 5 µg of dapivirine (in 25 µL of PBS), either associated to NPs or in suspension (Fig. 1.2.5).[83] Results showed that NPs were able to better sustain drug levels in vaginal lavages, vaginal tissue, and, partially, the lower half of the uterine horns, despite an overall fast decrease of dapivirine amounts in the genital tract. Vaginal lavage drug levels seem to have been maintained above levels previously found protective in a humanized mouse model[84] for up to 24 h in animals treated with NPs, but only up to 4 h in the case of dapivirine in suspension.[83] Furthermore, dapivirine was able to reach

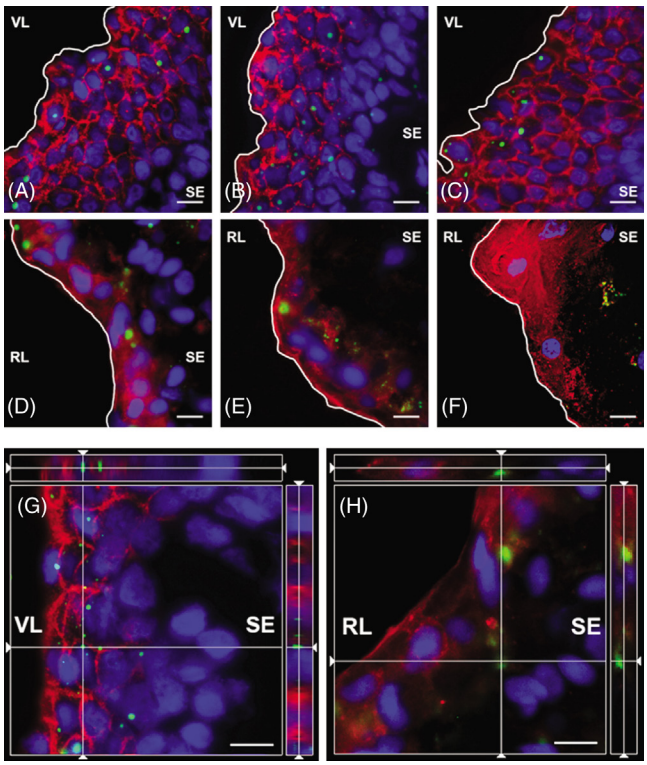

FIGURE 1.2.3 Evidence of the Penetration of Fluorescent NPs in Pig Vaginal and Rectal Mucosae.

Fluorescent microscopy images of pig (A–C) vaginal and (D–F) rectal mucosa after 2 h incubation with (A and D) PEO–rhodamine-123–PCL NPs, (B and E) SLS–rhodamine-123–PCL NPs, and (C and F) CTAB–rhodamine-123–PCL NPs. Detailed fluorescent confocal microscopy images of pig (G) vaginal and (H) rectal mucosae after 2 h incubation with PEO–rhodamine-123–PCL NPs. *Green*, *blue*, and *red* signals are from rhodamine-123–PCL (NPs), Hoechst 33342 (DNA), and wheat germ agglutinin (WGA), Alexa Fluor 594 conjugate (sialic acid/*N*-acetylglucosaminyl residues at cell membranes/mucin), respectively. *White lining* in A–F depicts the mucosal tissue surface and has been included for clarity. Scale bars = 10 μm. *z*-Axis range is 6 and 16 μm for vaginal and rectal mucosa, respectively. *RL*, Rectal lumen; *SE*, subepithelium; *VL*, vaginal lumen.

Reprinted with permission from das Neves J, Araújo F, Andrade F, Michiels J, Arien KK, Vanham G, et al. In vitro and ex vivo evaluation of polymeric nanoparticles for vaginal and rectal delivery of the anti-HIV drug dapivirine. Mol Pharm *2013;**10**(7):2793–807.*[76] *Copyright 2013 American Chemical Society.*

rectal tissues in quantifiable amounts (Fig. 1.2.5), most likely due to external access of vaginal leakage. The significance of these findings for the potential protection from rectal infection deserves further investigation. Overall, local PK data seemed promising when considering the development of a once daily, coitus-independent microbicide product. Still, animal efficacy studies are required to truly assess obtained

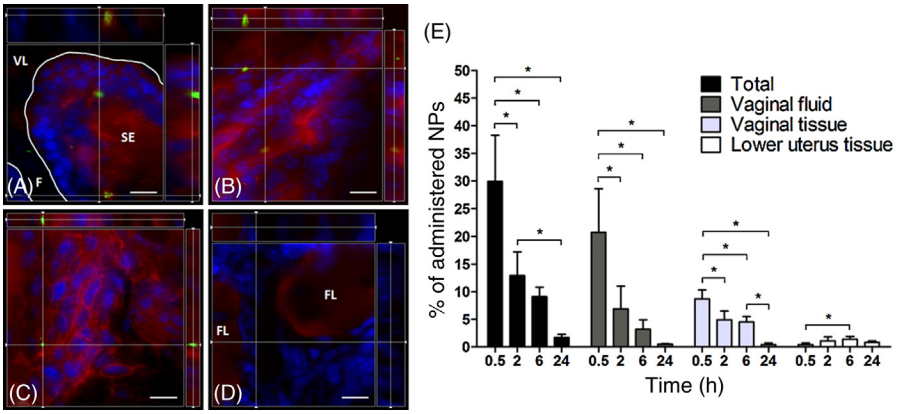

FIGURE 1.2.4 Tissue Penetration and Distribution of Fluorescent PEO–PCL NPs in the Genital Tract.

Fluorescent confocal microscopy images of the (A) vagina, (B) lower uterus, (C) upper uterus, and (D) ovaries were taken 2 h after vaginal administration of PEO–rhodamine-123–PCL NPs (*green*). Images are representative of (A and D) transverse and (B and C) longitudinal sections. *Blue* and *red* signals are from Hoechst 33342 (DNA) and WGA, Alexa Fluor 594 conjugate (sialic acid/*N*-acetylglucosaminyl residues at cell membranes/mucin), respectively. The mucosal tissue surface in (A) (*white lining*) has been included for clarity. Recovery of fluorescent NPs from vaginal lavages and vaginal/lower uterine tissues is presented in (E). Results are expressed as the percentage of the initial amount of NPs administered intravaginally. Columns represent mean values and bars, the standard deviation ($n = 5$). An *asterisk* denotes $P < 0.05$ when comparing amounts of fluorescent NPs at different time points. Scale bars = 10 μm. *F*, Vaginal folding; *FL*, follicle; *SE*, subepithelium; *VL*, vaginal lumen.

Reprinted from das Neves J, Araújo F, Andrade F, Amiji M, Bahia MF, Sarmento B. Biodistribution and pharmacokinetics of dapivirine-loaded nanoparticles after vaginal delivery in mice. Pharm Res *2014;**31**(7):1834–45.[83] Copyright 2014 Springer Science + Business Media.*

PK data. Dapivirine-loaded PEO–PCL NPs were also shown safe upon once daily vaginal administration for 14 days, as assessed by histological analysis and assay of inflammatory chemokine/cytokine levels in vaginal lavages. Systemic drug exposure was low in all cases.[83]

3.1.2 Rilpivirine-loaded PLGA nanoparticles

Rilpivirine is a nonnucleoside reverse transcriptase inhibitor from the same chemical class as dapivirine, being currently used in AIDS therapy.[85] This drug is also being developed as a long-acting, NP-based injectable to be used as PrEP [86]. In a recent report, Kovarova et al.[87] proposed and evaluated for efficacy of a nanotechnology-based formulation of rilpivirine in humanized BLT mice. PEO-modified PLGA NPs (mean hydrodynamic diameter = 66 nm) were selected as drug carriers, being further incorporated into a poloxamer-based thermosensitive gel that undergoes sol–gel transition at body temperature. Drug concentration in the gel was approximately 0.09%

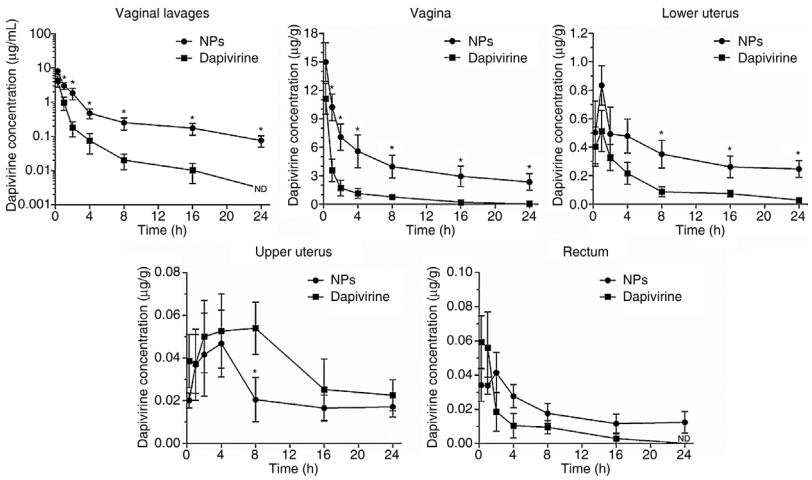

FIGURE 1.2.5 Dapivirine Levels in Vaginal Lavages, Genital Tissues, and Rectum Following Vaginal Administration of Dapivirine-Loaded PEO-Modified PCL NPs or the Free Drug in Phosphate Buffered Saline (PBS, pH 7.4).

Note the different scales and units in *y*-axes, including the log scale for vaginal lavages. Individual points represent mean values and vertical bars, the standard error of the mean ($n = 5$). An *asterisk* denotes $P < 0.05$ when comparing NPs with free dapivirine at the same time point. *ND*, Not detected (<0.003 μg/mL for lavages; <0.006 μg/mL for rectal tissue).

Reprinted from das Neves J, Araújo F, Andrade F, Amiji M, Bahia MF, Sarmento B. Biodistribution and pharmacokinetics of dapivirine-loaded nanoparticles after vaginal delivery in mice. Pharm Res *2014;**31**(7):1834–45.[83] Copyright 2014 Springer Science + Business Media.*

(w/w). The use of such gel has been adapted from previous work undertaken by one of the author's research group to allow ease of administration and enhanced vaginal retention of NPs and rilpivirine.[60,64] Animals treated intravaginally with 20 μL of rilpivirine-loaded NPs gel at 1.5 h before viral challenge (310,000 $TCID_{50}$ of CCR5-tropic HIV-1_{RHPA}) were fully protected from infection.[87] Protection decreased to 50% when the time elapsed from gel administration to viral challenge was extended to 24 h. All control mice were infected by HIV irrespective of the time of administration. The authors of the study claimed that observed protective effects were linked with the formation of a layer of NPs covering the cervicovaginal epithelium that partially persisted up to 24 h post-administration.[87] NPs were also able to penetrate tissues up till the vicinities of HIV-susceptible cells. Although no PK data were provided, results suggest that a significant amount of drug was retained in the vagina for up to at least 24 h. Additionally, assessment of the real value of these NPs and gel formulation in providing protection is not easy, as controls containing free rilpivirine were not included in the study.

3.1.3 Tenofovir disoproxil fumarate–loaded PLGA nanoparticles

Tenofovir disoproxil fumarate (TDF), a prodrug of tenofovir, possesses higher hydrophobicity resulting in higher tissue permeability and cell uptake as compared to the parent molecule, thus leading to enhanced potency.[88,89] These features alone may justify its use as an alternative to tenofovir to obtain potent microbicides. In a recently reported study, Destache et al.[90] incorporated TDF into PLGA NPs (mean hydrodynamic diameter = 149 nm) using sodium deoxycholate as an ion-pairing agent. The addition of sodium deoxycholate allowed enhanced drug association to NPs by about 4 times. NPs were further incorporated into poloxamer-based thermosensitive gels at different TDF concentrations to facilitate vaginal administration. Gels were administered to humanized BLT mice before intravaginal challenge with HIV-1. All animals treated with placebo thermosensitive gel and challenged after 4 h were infected. Conversely, mice were fully protected when administered with different gels containing TDF-loaded NPs and challenged with the virus at different time points posttreatment: 0.1% TDF and 4 h or 0.5% TDF and 24 h. No protection was observed when TDF-loaded NPs in gel at 1% TDF were used at 7 days before viral challenge.[90] These results appear to support that TDF-loaded NPs in thermosensitive gels may be useful as coitus-independent effective microbicides. However, as no data for gels containing TDF alone (i.e., without incorporation into NPs) were provided, it is difficult to assess the real value of the nanocarriers in protection against viral infection. Also, the use of gels bearing different quantities of TDF when different challenge times were considered and the lack of detailed PK data make it difficult to fully understand the value of this otherwise interesting study.

3.1.4 −2 RANTES/liposome complexes

Despite being frequently considered for vaginal drug delivery[91–93] and featuring well-known technological versatility, stability, and biocompatibility,[94] liposomal carriers have been mostly overlooked in the development of nanomicrobicides. One exception has been the use of commercially available Novasome 7474 (Novavax, Gaithersburg, Maryland, USA and IGI Laboratories, Buena, New Jersey, USA) for the vaginal delivery of −2 RANTES, a truncated fragment of Regulated on Activation, Normal T Expressed and Secreted (RANTES) chemokine presenting high specificity for CCR5 binding.[95,96] Novasome are 200–700 nm nonphospholipidic liposomes comprising monoesters of PEO fatty acids, cholesterol, and free fatty acids.[97] The association of −2 RANTES with Novasome did not affect the native activity of the protein.[95,96] Data from an initial study by Kish-Catalone et al.[95] were able to indicate that −2 RANTES/liposome complexes elicited only mild signs of inflammation when administered to mice (single dose) and rabbits (daily administration for 10 consecutive days), thus being considered acceptable for vaginal use. The efficacy of these complexes against vaginal transmission of CCR5-tropic $SHIV_{162P3}$ was further tested in cynomolgus macaques.[96] Pretreatment (30–45 min) of animals with −2 RANTES/liposome complexes in PBS before viral challenge resulted in partial yet significant protection as compared to animals treated with PBS alone. −2 RANTES in PBS solution provided no significant protection when used at a concentration up to nearly 4 times of that

used for complexes. Remarkably, blank liposomes presented similar protection results as compared to those carrying −2 RANTES.[96] A possible explanation may be the inherent antiviral activity of Novasome 7474 as documented for other liposomal vesicles.[98,99] In any case, the ability of liposomes to evenly distribute throughout the mucosa seems to have been important for creating a protective barrier against viral transmission. Additional studies are necessary to clarify these issues.

3.1.5 siRNA-based nanosystems

Strategies comprising mucosal posttranscriptional gene silencing have been considered promising in preventing sexual transmission of HIV.[100] RNA interference (RNAi), namely using small interference RNA (siRNA), may constitute a relatively simple yet challenging approach to silence genes coding for important molecules involved in the life cycle of HIV, particularly those of host origin. Despite significant advances made in the field,[101,102] issues regarding intracellular delivery, molecular stability, and off-target effects of oligonucleotides may impair success and novel formulation approaches are required.[103] Furthermore, specificities of mucosal sites, such as the vagina may present specific additional limitations to the topical delivery of labile molecules (e.g., siRNA).[104] The role of nanotechnology in aiding RNAi-based therapeutics is well recognized,[105] but its application in the field of anti-HIV microbicides is scarce. To our best knowledge, the reports by Eszterhas et al.[106] and Boyapalle et al.[107] constitute the only studies on the subject. The first group of researchers used a commercial cationic polymer transfection agent (INTERFERin, Polyplus-transfection) to produce 45–60 nm polyplexes with CD4- and CCR5-specific siRNA.[106] Obtained nanosystems were able to partially suppress the expression of CD4 and CCR5 in ex vivo human tissue models (endometrial and cervical) for several days, as well as provide partial but significant protection from HIV challenge at 48 h posttransfection. Moreover, mild but significant silencing for several days was observed in the reproductive tract of BALB/c mice in which an aqueous dispersion of murine siRNA targeting CD4 was instilled directly into the uterus.[106] Boyapalleet al.[107] proposed an interesting system based in chitosan–Lipofectamine 2000 NPs (mean hydrodynamic diameter = 441 nm) for the delivery of a plasmid DNA coding for various siRNAs targeting viral (HIV-1 *tat*, *rev*, *gag*, and 5′-LTR) and host (CCR5 and CXCR4) factors. An anti-inflammatory cream of unspecified composition was used as a vehicle for NP administration. In a pilot study, the cream containing the plasmid siRNA cocktail was administered intravaginally to three rhesus macaques at 6 and 3 days before, as well as on the same day of viral challenge with $SHIV_{SF162P3}$. A complete blocking of infection was not observed, although plasmatic viral loads in treated animals were significantly lower than in those receiving the cream only. Also, a 10-day study in rabbits demonstrated the safety of the cream containing NPs. Despite the fact that the reported findings of both previous studies may be considered borderline as to the ability of proposed nanosystems to prevent viral transmission, they seem to support the relevance of nanotechnology in siRNA-based microbicide development. Still, substantial work is required to optimize oligonucleotide vaginal delivery for the prevention of HIV transmission.

3.1.6 Drug-loaded nanofibers

Micro- and nanofibers are attracting substantial attention in the biomedical field for multiple potential applications.[108,109] These typically comprise string-like systems that can extend up to at least several centimeters and present cross-sectional diameter in the nano- or micrometer ranges. Electrospun polymeric fibers in particular have been found useful as novel and versatile drug delivery platforms, and their application in the development of vaginal microbicides is being actively explored.[110,111] Features that may be considered useful when thinking about preventing HIV transmission include: (1) large surface area of fibers, which allows enhanced interactions between fiber surface and outer environment components, including with HIV; (2) the capacity to form mesh-like structures bearing variable pore size that may restrict transport of sperm and viruses; and (3) the ability to incorporate multiple compounds with distinct physicochemical properties.[111] Alongside a few other interesting studies by Huang et al. on pH-sensitive, CAP-based fibers[112] and HIV-trapping, polystyrene-based fibers,[113] as well as those recently reported by Youan and coworkers on thiolated chitosan[56] and PEO shell/thiolated hyaluronic acid plus poly(lactic acid) shell[57] nanofibers for the delivery of tenofovir, most of the research efforts have been undertaken by Woodrow and coworkers at the University of Washington.[114] The latter researchers were able to produce multiple nanofiber formulations by electrospinning using various matrix-forming materials and composites (e.g., PEO, polyvinylpyrrolidone, PLGA, poly-L-lactide, and PCL) and incorporating variable doses of different drugs. These last included compounds with antiviral effect (e.g., zidovudine, tenofovir, maraviroc, or raltegravir) or even with different pharmacological activities.[115–118] Indeed, the combined incorporation of antiherpetic (acyclovir), contraceptive (levonorgestrel), and spermicide (methyl-β-cyclodextrin and glycerol monolaurate) compounds makes nanofibers an interesting delivery platform for designing multipurpose prevention technologies (MPTs). Superimposing and interlacing nanofibers may further allow obtaining meshes with small pore diameters that can restrict pathogens and sperm mobility, thus providing additional anti-infective and contraceptive mechanisms, respectively.[115] The development of MPT products is considered highly relevant, as, apart from preventing HIV transmission, these can also be useful in averting other sexually transmitted infections and/or provide an additional contraceptive option for women.[119]

Modifications in composition and electrospinning processing were shown to be easily undertaken to effectively modulate the properties of fibers (such as diameter, degradation/dissolution, surface morphology, microstructure, drug loading, and crystallinity) and resulting fabrics (i.e., thickness, tensile strength, and Young's module), which can ultimately affect drug release profiles.[115,117,118] Bulk fabrics were shown to be readily shaped into tampon-like shapes that may allow for convenient vaginal administration.[115] Also, successful and cost-effective scale-up of the production processes typically used in the laboratory has been demonstrated for poly(vinyl alcohol) (PVA)–based nanofibers (≈140–320 nm mean cross-sectional diameters) with tenofovir-loading values of up to 60% (w/w).[118] This ability to produce nanofibers at the industrial scale seems critical when considering that an effective and affordable microbicide will have a high market demand. In general, nanofibers produced by

Woodrow and coworkers appeared to present favorable in vitro safety profiles, and that any observed toxicity seemed to have been mostly determined by used materials and active molecules.[115,117,120] Consistent in vivo data is still missing for these carriers, but preliminary experiments in mice evidenced that 30:70 poly-L-lactide/PEO nanofibers (around 600 nm diameter) can provide rapid and extensive coating of the vaginal mucosa as assessed using an in vivo imaging system.[115] Further developments on microbicide nanofibers are eagerly awaited.

3.2 DELIVERY PLATFORMS FOR NANOMICROBICIDES

To be used in practice, it is important to develop platforms for microbicide nanosystems that allow adequate stability, administration, and performance in loco (e.g., good distribution and retention throughout mucosae), while guaranteeing safety and potential effectiveness. Such platforms may be dosage forms commonly used for vaginal or rectal administration. It is impossible to establish one dosage form as a preferential from an end user's perspective (men or women), as product acceptability is widely variable among different sociodemographic and socioeconomic backgrounds.[121–124] Hence, considering multiple platforms for developing nanotechnology-based microbicide products appears to be of interest. Following the footsteps of early microbicides, gels have been frequently proposed as a dosage form for incorporating microbicide nanosystems with either inherent activity (e.g., VivaGel) or acting as drug carriers. In this last case, different examples have been described in literature, particularly poloxamer-based thermosensitive gels for vaginal administration.[60,64,87,90] As described in Section 3.1.2, such an approach achieves easy-to-administer liquids that promote retention once sol–gel transition occurs due to an increase in temperature. Moreover, poloxamer-based gels appear to be generally safe and not to interfere significantly with antiretroviral activity.[60,64]

Gels, however, may present several limitations when considering the development of nanomicrobicides. A general issue concerns vaginal leakage after administration. Due to their typical aqueous nature, stability issues may also arise, particularly related with the premature release of antiretroviral drugs from nanocarrier systems. Moreover, gels require the use of applicators that can increase cost (namely when single use prefilled applicators are considered), and portability is somewhat limited due to the bulkiness of gel tubes and applicators. To overcome such problems, polymeric films have been proposed as platforms for the vaginal administration of antiretroviral drug nanocarriers.[125] Vaginal films have long been used for drug delivery and are generally regarded as acceptable by women.[126] These systems usually comprise thin, flexible, smooth sheets of variable color and transparency, as well as shape (mainly square or rectangular) and area (up to 100 cm^2). The film matrix typically comprises hydrophilic polymers (e.g., PVA, cellulose derivatives, and carrageenan) and plasticizers (e.g., glycerin and PEO), as well as various other optional excipients (e.g., stabilizers, preservatives, and disintegrants).[127] In general, films are designed to dissolve or disintegrate rapidly to release their payload.

Table 1.2.2 Studies Using NPs in Films as Delivery Platforms for Potential Microbicide Compounds

Active Molecules	Nanocarriers (Diameters, nm[a])	Film Compositions	Main Findings	References
siRNA against *SNAP23*[b]	Polyethylenimine complexes functionalized with anti-HLA-DR antibody (223)	PVA, λ-carrageenan, glycerin, PEO 400	siRNA nanocomplexes were able to be transported across an in vitro vaginal mucosa model, selectively taken up by HLA-DR$^+$ DCs and silence *SNAP23*	[128]
IQP-0528	PEO–PLGA/ Eudragit S100 NPs (434)	PVA, HPMC, glycerin, PEO 400, propylene glycol	Genital PK in pig-tailed macaque suggest that protective levels may be achieved up to 24 h following administration even if no differences were observed as compared to IQP-0528 dispersed directly into the film matrix	[129]
Tenofovir	Stearylamine/ PLGA NPs (127)	PVA, HPMC, glycerin	Films were optimized for biophysical properties and shown safe (histology and chemokine/cytokine levels in lavages) after daily vaginal administration for 14 days in mice	[130]
Efavirenz + tenofovir	PLGA NPs (275)[c]	PVA, HPMC, glycerin	*See details in the main text*	[131]

DCs, Dendritic cells; HLA-DR, human leukocyte antigen DR; HPMC, hydroxypropyl methylcellulose; PEO, poly(ethylene oxide); PK, pharmacokinetics; PLGA, poly(lactic-co-glycolic acid); PVA, poly(vinyl alcohol).

[a] *Mean hydrodynamic diameter.*

[b] *Host protein involved in the exocytosis of HIV.*

[c] *Efavirenz was loaded into NPs and tenofovir was dissolved directly in the film matrix.*

A few studies detailing on NPs in films as potential microbicide products have been described (Table 1.2.2).[128–131] For example, our group demonstrated the versatility and potential usefulness of NPs-in-film systems for delivering a combination of hydrophobic (efavirenz) and hydrophilic (tenofovir) antiretroviral drugs.[131] Efavirenz-loaded PLGA NPs and tenofovir were incorporated into the polymer matrix during manufacturing by solvent casting. Obtained films (Fig. 1.2.6) were

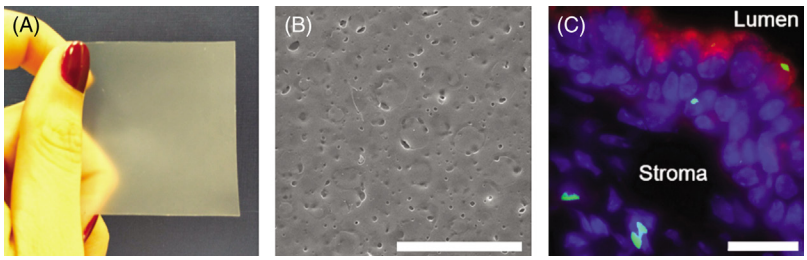

FIGURE 1.2.6 Some Features of Tenofovir/Efavirenz-Loaded NPs in Film.

(A) A photograph of a human-shaped film (5 × 5 cm). (B) A scanning electron microscopy image of the film surface (bar = 50 μm). (C) A confocal microscopy image evidencing the penetration of fluorescent NPs into the mouse vaginal mucosa at 2 h post-administration. *White*, *gray*, and *light gray* signals (*green*, *blue*, and *red* signals in the web version) are from PLGA–fluorescein (from fluorescent NPs), 4′,6-diamidino-2-phenylindole (DAPI; nuclear DNA), and WGA, Alexa Fluor 594 conjugate (sialic acid/N-acetylglucosaminyl residues at cell membranes/mucin), respectively (bar = 20 μm).

Adapted from Cunha-Reis C, Machado A, Barreiros L, Araújo F, Nunes R, Seabra V, et al. Nanoparticles-in-film for the combined vaginal delivery of anti-HIV microbicide drugs. J Control Release *2016;**243**:43–53.*[131] *Copyright 2016 Elsevier.*

characterized for physicochemical characteristics relevant to vaginal administration, such as organoleptic features, drug release, mechanical properties, disintegration in simulated vaginal fluid, osmolality and pH upon disintegration, and ex vivo adhesiveness to pig vaginal mucosa, and were found suitable for further animal in vivo testing. Films increased the vaginal retention of NPs in a mouse model as compared to the administration in PBS suspension. Furthermore, NPs were found to deeply penetrate the mucosa and reach the stroma.[131] PK of efavirenz in vaginal tissue and lavage were improved when the drug was associated with NPs: relative bioavailability in tissue and lavage was increased by roughly 2 and 6 times, respectively, as compared to films containing free efavirenz (i.e., directly dispersed in the film matrix without the incorporation of NPs). All drug assays were performed using a validated liquid chromatography–tandem mass spectrometry method.[132] Finally, NPs in films were shown safe as assessed by histological analysis and measurement of proinflammatory mediators (IL-1β, IL-6, KC, and TNFα) in vaginal lavages upon daily vaginal administration for 14 days.[131] These data seem to support that the tenofovir/efavirenz-loaded NPs in film is a promising candidate microbicide product.

4 CONCLUSIONS

The topical administration of antiretroviral drug–based microbicides may be an interesting preventive approach to circumvent the HIV/AIDS epidemic. Nanotechnology provides interesting tools in aiding the vaginal and/or rectal delivery of promising anti-HIV drugs. The examples and case studies described in this subchapter provide consistent evidence that nanocarrier systems can contribute to the development of

novel microbicide products. In particular, polymeric nanosystems seem to be particularly suitable for delivering promising antiretroviral drugs. Still, important work is required regarding the optimization of platforms for the administration of nanocarriers, long-term safety of nanomicrobicides, and scale-up and feasible industrial production of affordable products. Finally, substantial research efforts in nanotechnology-based approaches for the development of rectal microbicides are eagerly required.

ACKNOWLEDGMENTS

This work was financed by Programa Gilead GÉNESE, Gilead Portugal (PGG/046/2015 and PGG/002/2016). This article is a result of the project NORTE-01-0145-FEDER-000012, supported by Norte Portugal Regional Operational Programme (NORTE 2020), under the PORTUGAL 2020 Partnership Agreement, through the European Regional Development Fund (ERDF). This work was financed by FEDER—Fundo Europeu de Desenvolvimento Regional funds through the COMPETE 2020—Operacional Programme for Competitiveness and Internationalisation (POCI), Portugal 2020, and by Portuguese funds through FCT—Fundação para a Ciência e a Tecnologia/Ministério da Ciência, Tecnologia e Ensino Superior in the framework of the project "Institute for Research and Innovation in Health Sciences" (POCI-01-0145-FEDER-007274). José das Neves gratefully acknowledges FCT for financial support (grant SFRH/BPD/92934/2013). Parts of this manuscript are reproduced from a recent review article published by the authors' research group,[16] with permission from Elsevier (Copyright 2016).

REFERENCES

1. Wang H, Wolock TM, Carter A, Nguyen G, Kyu HH, GBD HIV Collaborators et al. Estimates of global, regional, and national incidence, prevalence, and mortality of HIV, 1980-2015: the Global Burden of Disease Study 2015. *Lancet HIV* 2016;**3**(8):e361–87.
2. Bunnell R, Mermin J, De Cock KM. HIV prevention for a threatened continent: implementing positive prevention in Africa. *JAMA* 2006;**296**(7):855–8.
3. Sabin CA, Cooper DA, Collins S, Schechter M. Rating evidence in treatment guidelines: a case example of when to initiate combination antiretroviral therapy (cART) in HIV-positive asymptomatic persons. *AIDS* 2013;**27**(12):1839–46.
4. Lundgren JD, Babiker AG, Gordin F, Emery S, Grund B, Insight Start Study Group et al. Initiation of antiretroviral therapy in early asymptomatic HIV infection. *N Engl J Med* 2015;**373**(9):795–807.
5. Simon V, Ho DD, Abdool Karim Q. HIV/AIDS epidemiology, pathogenesis, prevention, and treatment. *Lancet* 2006;**368**(9534):489–504.
6. Maartens G, Celum C, Lewin SR. HIV infection: epidemiology, pathogenesis, treatment, and prevention. *Lancet* 2014;**384**(9939):258–71.
7. Piot P, Abdool Karim SS, Hecht R, Legido-Quigley H, Buse K, Stover J, et al. Defeating AIDS—advancing global health. *Lancet* 2015;**386**(9989):171–218.
8. Baeten J, Celum C. Systemic and topical drugs for the prevention of HIV infection: antiretroviral pre-exposure prophylaxis. *Annu Rev Med* 2013;**64**:219–32.
9. Thomson KA, Baeten JM, Mugo NR, Bekker LG, Celum CL, Heffron R. Tenofovir-based oral preexposure prophylaxis prevents HIV infection among women. *Curr Opin HIV AIDS* 2016;**11**(1):18–26.

10. Horn T, Jefferys R. Preventive technologies: antiretroviral and vaccine development. *Pipeline Report* 2016. Available from: http://pipelinereport.org/2016/HIV-prevention.
11. McGowan I. The development of rectal microbicides for HIV prevention. *Expert Opin Drug Deliv* 2014;**11**(1):69–82.
12. das Neves J, Sarmento B, editors. *Drug delivery and development of anti-HIV microbicides*. Singapore: Pan Stanford; 2014.
13. UNAIDS. *Global AIDS Update*. Geneva, Switzerland: World Health Organization; 2016.
14. Morrow G, Vachot L, Vagenas P, Robbiani M. Current concepts of HIV transmission. *Curr HIV/AIDS Rep* 2007;**4**(1):29–35.
15. Haase AT. Early events in sexual transmission of HIV and SIV and opportunities for interventions. *Annu Rev Med* 2011;**62**:127–39.
16. das Neves J, Nunes R, Rodrigues F, Sarmento B. Nanomedicine in the development of anti-HIV microbicides. *Adv Drug Deliv Rev* 2016;**103**:57–75.
17. Fauci AS. An HIV vaccine: mapping uncharted territory. *JAMA* 2016;**316**(2):143–4.
18. Krishnaratne S, Hensen B, Cordes J, Enstone J, Hargreaves JR. Interventions to strengthen the HIV prevention cascade: a systematic review of reviews. *Lancet HIV* 2016;**3**(7):e307–17.
19. Smith JA, Anderson SJ, Harris KL, McGillen JB, Lee E, Garnett GP, et al. Maximising HIV prevention by balancing the opportunities of today with the promises of tomorrow: a modelling study. *Lancet HIV* 2016;**3**(7):e289–96.
20. Cutler B, Justman J. Vaginal microbicides and the prevention of HIV transmission. *Lancet Infect Dis* 2008;**8**(11):685–97.
21. Ariën KK, Jespers V, Vanham G. HIV sexual transmission and microbicides. *Rev Med Virol* 2011;**21**(2):110–33.
22. McNicholl JM. Combining biomedical preventions for HIV: vaccines with pre-exposure prophylaxis, microbicides or other HIV preventions. *Hum Vaccin Immunother* 2016;**12**(12):3202–11.
23. Baeten JM, Palanee-Phillips T, Brown ER, Schwartz K, Soto-Torres LE, Govender V, et al. Use of a vaginal ring containing dapivirine for HIV-1 prevention in women. *N Engl J Med* 2016;**375**(22):2121–32.
24. Nel A, van Niekerk N, Kapiga S, Bekker LG, Gama C, Gill K, et al. Safety and efficacy of a dapivirine vaginal ring for HIV prevention in women. *N Engl J Med* 2016;**375**(22):2133–43.
25. Abdool Karim Q, Abdool Karim SS, Frohlich JA, Grobler AC, Baxter C, Mansoor LE, et al. Effectiveness and safety of tenofovir gel, an antiretroviral microbicide, for the prevention of HIV infection in women. *Science* 2010;**329**(5996):1168–74.
26. Nunes R, Sarmento B, das Neves J. Formulation and delivery of anti-HIV rectal microbicides: advances and challenges. *J Control Release* 2014;**194**:278–94.
27. Kashuba AD, Gengiah TN, Werner L, Yang KH, White NR, Karim QA, et al. Genital tenofovir concentrations correlate with protection against HIV infection in the CAPRISA 004 trial: importance of adherence for microbicide effectiveness. *J Acquir Immune Defic Syndr* 2015;**69**(3):264–9.
28. Chen BA, Panther L, Marzinke MA, Hendrix CW, Hoesley CJ, van der Straten A, et al. Phase 1 safety, pharmacokinetics, and pharmacodynamics of dapivirine and maraviroc vaginal rings: a double-blind randomized trial. *J Acquir Immune Defic Syndr* 2015;**70**(3):242–9.
29. das Neves J, Bahia MF. Gels as vaginal drug delivery systems. *Int J Pharm* 2006;**318**(1–2):1–14.
30. Muchomba FM, Gearing RE, Simoni JM, El-Bassel N. State of science of adherence in pre-exposure prophylaxis and microbicide trials. *J Acquir Immune Defic Syndr* 2012;**61**(4):490–8.

31. Agashe H, Hu M, Rohan L. Formulation and delivery of microbicides. *Curr HIV Res* 2012;**10**(1):88–96.
32. Zhang W, Hu M, Shi Y, Gong T, Dezzutti CS, Moncla B, et al. Vaginal microbicide film combinations of two reverse transcriptase inhibitors, EFdA and CSIC, for the prevention of HIV-1 sexual transmission. *Pharm Res* 2015;**32**(9):2960–72.
33. Bunge KE, Dezzutti CS, Rohan LC, Hendrix CW, Marzinke MA, Richardson-Harman N, et al. A Phase 1 trial to assess the safety, acceptability, pharmacokinetics and pharmacodynamics of a novel dapivirine vaginal film. *J Acquir Immune Defic Syndr* 2015;**71**(5):498–505.
34. Malcolm RK, Boyd PJ, McCoy CF, Murphy DJ. Microbicide vaginal rings: technological challenges and clinical development. *Adv Drug Deliv Rev* 2016;**103**:33–56.
35. Montgomery ET, van der Straten A, Cheng H, Wegner L, Masenga G, von Mollendorf C, et al. Vaginal ring adherence in sub-Saharan Africa: expulsion, removal, and perfect use. *AIDS Behav* 2012;**16**(7):1787–98.
36. das Neves J, Amaral MH, Bahia MF. Vaginal drug delivery. In: Gad SC, editor. *Pharmaceutical manufacturing handbook: production and processes*. Hoboken, NJ: Wiley; 2008. p. 809–78.
37. das Neves J, Palmeira-de-Oliveira R, Palmeira-de-Oliveira A, Rodrigues F, Sarmento B. Vaginal mucosa and drug delivery. In: Khutoryanskiy VV, editor. *Mucoadhesive materials and drug delivery systems*. Chichester: Wiley; 2014. p. 99–131.
38. Etheridge ML, Campbell SA, Erdman AG, Haynes CL, Wolf SM, McCullough J. The big picture on nanomedicine: the state of investigational and approved nanomedicine products. *Nanomedicine* 2013;**9**(1):1–14.
39. das Neves J, Amiji MM, Bahia MF, Sarmento B. Nanotechnology-based systems for the treatment and prevention of HIV/AIDS. *Adv Drug Deliv Rev* 2010;**62**(4–5):458–77.
40. Roy U, Rodríguez J, Barber P, das Neves J, Sarmento B, Nair M. The potential of HIV-1 nanotherapeutics: from in vitro studies to clinical trials. *Nanomedicine* 2015;**10**(24):3597–609.
41. Nunes R, Sousa C, Sarmento B, das Neves J. Nanotechnology-based systems for microbicide development. In: das Neves J, Sarmento B, editors. *Drug delivery and development of anti-HIV microbicides*. Singapore: Pan Stanford; 2014. p. 415–58.
42. Jiménez JL, Pion M, de la Mata FJ, Gomez R, Muñoz E, Leal M, et al. Dendrimers as topical microbicides with activity against HIV. *New J Chem* 2012;**36**(2):299–309.
43. Nandy B, Saurabh S, Sahoo AK, Dixit NM, Maiti PK. The SPL7013 dendrimer destabilizes the HIV-1 gp120-CD4 complex. *Nanoscale* 2015;**7**(44):18628–41.
44. Klasse PJ. The molecular basis of HIV entry. *Cell Microbiol* 2012;**14**(8):1183–92.
45. O'Loughlin J, Millwood IY, McDonald HM, Price CF, Kaldor JM, Paull JR. Safety, tolerability, and pharmacokinetics of SPL7013 gel (VivaGel): a dose ranging, phase I study. *Sex Transm Dis* 2010;**37**(2):100–4.
46. Price CF, Tyssen D, Sonza S, Davie A, Evans S, Lewis GR, et al. SPL7013 Gel (VivaGel(R)) retains potent HIV-1 and HSV-2 inhibitory activity following vaginal administration in humans. *PLoS One* 2011;**6**(9):e24095.
47. Cohen CR, Brown J, Moscicki AB, Bukusi EA, Paull JR, Price CF, et al. A phase I randomized placebo controlled trial of the safety of 3% SPL7013 Gel (VivaGel(R)) in healthy young women administered twice daily for 14 days. *PLoS One* 2011;**6**(1):e16258.
48. Moscicki AB, Kaul R, Ma Y, Scott ME, Daud II, Bukusi EA, et al. Measurement of mucosal biomarkers in a phase 1 trial of intravaginal 3% StarPharma LTD 7013 gel (VivaGel) to assess expanded safety. *J Acquir Immune Defic Syndr* 2012;**59**(2):134–40.
49. Patton DL, Cosgrove Sweeney YT, McCarthy TD, Hillier SL. Preclinical safety and efficacy assessments of dendrimer-based (SPL7013) microbicide gel formulations in a nonhuman primate model. *Antimicrob Agents Chemother* 2006;**50**(5):1696–700.

50. Sepúlveda-Crespo D, Ceña-Díez R, Jiménez JL, Muñoz-Fernández MÁ. Mechanistic studies of viral entry: an overview of dendrimer-based microbicides as entry inhibitors against both HIV and HSV-2 overlapped infections. *Med Res Rev* 2017;**37**(1):149–79.
51. Alukda D, Sturgis T, Youan BB. Formulation of tenofovir-loaded functionalized solid lipid nanoparticles intended for HIV prevention. *J Pharm Sci* 2011;**100**(8):3345–56.
52. Meng J, Sturgis TF, Youan BB. Engineering tenofovir loaded chitosan nanoparticles to maximize microbicide mucoadhesion. *Eur J Pharm Sci* 2011;**44**(1–2):57–67.
53. Meng J, Zhang T, Agrahari V, Ezoulin MJ, Youan BB. Comparative biophysical properties of tenofovir-loaded, thiolated and nonthiolated chitosan nanoparticles intended for HIV prevention. *Nanomedicine* 2014;**9**(11):1595–612.
54. Zhang T, Sturgis TF, Youan BB. pH-responsive nanoparticles releasing tenofovir intended for the prevention of HIV transmission. *Eur J Pharm Biopharm* 2011;**79**(3):526–36.
55. Agrahari V, Zhang C, Zhang T, Li W, Gounev TK, Oyler NA, et al. Hyaluronidase-sensitive nanoparticle templates for triggered release of HIV/AIDS microbicide in vitro. *AAPS J* 2014;**16**(2):181–93.
56. Meng J, Agrahari V, Ezoulin MJ, Zhang C, Purohit SS, Molteni A, et al. Tenofovir containing thiolated chitosan core/shell nanofibers: In vitro and in vivo evaluations. *Mol Pharm* 2016;**13**(12):4129–40.
57. Agrahari V, Meng J, Ezoulin MJ, Youm I, Dim DC, Molteni A, et al. Stimuli-sensitive thiolated hyaluronic acid based nanofibers: synthesis, preclinical safety and in vitro anti-HIV activity. *Nanomedicine* 2016;**11**(22):2935–58.
58. Ham AS, Cost MR, Sassi AB, Dezzutti CS, Rohan LC. Targeted delivery of PSC-RANTES for HIV-1 prevention using biodegradable nanoparticles. *Pharm Res* 2009;**26**(3):502–11.
59. das Neves J, Michiels J, Ariën KK, Vanham G, Amiji M, Bahia MF, et al. Polymeric nanoparticles affect the intracellular delivery, antiretroviral activity and cytotoxicity of the microbicide drug candidate dapivirine. *Pharm Res* 2012;**29**(6):1468–84.
60. Date AA, Shibata A, Goede M, Sanford B, La Bruzzo K, Belshan M, et al. Development and evaluation of a thermosensitive vaginal gel containing raltegravir + efavirenz loaded nanoparticles for HIV prophylaxis. *Antiviral Res* 2012;**96**(3):430–6.
61. Chaowanachan T, Krogstad E, Ball C, Woodrow KA. Drug synergy of tenofovir and nanoparticle-based antiretrovirals for HIV prophylaxis. *PLoS One* 2013;**8**(4):e61416.
62. Yang S, Chen Y, Gu K, Dash A, Sayre CL, Davies NM, et al. Novel intravaginal nanomedicine for the targeted delivery of saquinavir to CD4(+) immune cells. *Int J Nanomed* 2013;**8**:2847–58.
63. das Neves J, Sarmento B. Precise engineering of dapivirine-loaded nanoparticles for the development of anti-HIV vaginal microbicides. *Acta Biomater* 2015;**18**:77–87.
64. Date AA, Shibata A, McMullen E, La Bruzzo K, Bruck P, Belshan M, et al. Thermosensitive gel containing cellulose acetate phthalate-efavirenz combination nanoparticles for prevention of HIV-1 infection. *J Biomed Nanotechnol* 2015;**11**(3):416–27.
65. Lakshmi YS, Kumar P, Kishore G, Bhaskar C, Kondapi AK. Triple combination MPT vaginal microbicide using curcumin and efavirenz loaded lactoferrin nanoparticles. *Sci Rep* 2016;**6**:25479.
66. das Neves J, Nunes R, Machado A, Sarmento B. Polymer-based nanocarriers for vaginal drug delivery. *Adv Drug Deliv Rev* 2015;**92**:53–70.
67. das Neves J, Bahia MF, Amiji MM, Sarmento B. Mucoadhesive nanomedicines: characterization and modulation of mucoadhesion at the nanoscale. *Expert Opin Drug Deliv* 2011;**8**(8):1085–104.

68. Sosnik A, das Neves J, Sarmento B. Mucoadhesive polymers in the design of nano-drug delivery systems for administration by non-parenteral routes: a review. *Prog Polym Sci* 2014;**39**(12):2030–75.
69. Ensign LM, Cone R, Hanes J. Nanoparticle-based drug delivery to the vagina: a review. *J Control Release* 2014;**190**:500–14.
70. Boegh M, Nielsen HM. Mucus as a barrier to drug delivery—understanding and mimicking the barrier properties. *Basic Clin Pharmacol Toxicol* 2015;**116**(3):179–86.
71. Yang M, Yu T, Wang YY, Lai SK, Zeng Q, Miao B, et al. Vaginal delivery of paclitaxel via nanoparticles with non-mucoadhesive surfaces suppresses cervical tumor growth. *Adv Healthc Mater* 2014;**3**(7):1044–52.
72. Xu Q, Ensign LM, Boylan NJ, Schon A, Gong X, Yang JC, et al. Impact of surface polyethylene glycol (PEG) density on biodegradable nanoparticle transport in mucus ex vivo and distribution in vivo. *ACS Nano* 2015;**9**(9):9217–27.
73. Sarmento B, das Neves J. Nanosystem formulations for rectal microbicides: a call for more research. *Ther Deliv* 2012;**3**(1):1–4.
74. Hendrix CW, Fuchs EJ, Macura KJ, Lee LA, Parsons TL, Bakshi RP, et al. Quantitative imaging and sigmoidoscopy to assess distribution of rectal microbicide surrogates. *Clin Pharmacol Ther* 2008;**83**(1):97–105.
75. Maisel K, Ensign L, Reddy M, Cone R, Hanes J. Effect of surface chemistry on nanoparticle interaction with gastrointestinal mucus and distribution in the gastrointestinal tract following oral and rectal administration in the mouse. *J Control Release* 2015;**197**:48–57.
76. das Neves J, Araújo F, Andrade F, Michiels J, Ariën KK, Vanham G, et al. In vitro and ex vivo evaluation of polymeric nanoparticles for vaginal and rectal delivery of the anti-HIV drug dapivirine. *Mol Pharm* 2013;**10**(7):2793–807.
77. Samizadeh M, Zhang X, Gunaseelan S, Nelson AG, Palombo MS, Myers DR, et al. Colorectal delivery and retention of PEG-Amprenavir-Bac7 nanoconjugates-proof of concept for HIV mucosal pre-exposure prophylaxis. *Drug Deliv Transl Res* 2016;**6**(1):1–16.
78. das Neves J, Martins JP, Sarmento B. Will dapivirine redeem the promises of anti-HIV microbicides? Overview of product design and clinical testing. *Adv Drug Deliv Rev* 2016;**103**:20–32.
79. das Neves J, Sarmento B, Amiji MM, Bahia MF. Development and validation of a rapid reversed-phase HPLC method for the determination of the non-nucleoside reverse transcriptase inhibitor dapivirine from polymeric nanoparticles. *J Pharm Biomed Anal* 2010;**52**(2):167–72.
80. das Neves J, Rocha CM, Gonçalves MP, Carrier RL, Amiji M, Bahia MF, et al. Interactions of microbicide nanoparticles with a simulated vaginal fluid. *Mol Pharm* 2012;**9**(11):3347–56.
81. das Neves J, Sarmento B, Amiji M, Bahia MF. Development and validation of a HPLC method for the assay of dapivirine in cell-based and tissue permeability experiments. *J Chromatogr B* 2012;**911**:76–83.
82. das Neves J, Amiji M, Bahia MF, Sarmento B. Assessing the physical-chemical properties and stability of dapivirine-loaded polymeric nanoparticles. *Int J Pharm* 2013;**456**(2):307–14.
83. das Neves J, Araújo F, Andrade F, Amiji M, Bahia MF, Sarmento B. Biodistribution and pharmacokinetics of dapivirine-loaded nanoparticles after vaginal delivery in mice. *Pharm Res* 2014;**31**(7):1834–45.
84. Di Fabio S, Giannini G, Lapenta C, Spada M, Binelli A, Germinario E, et al. Vaginal transmission of HIV-1 in hu-SCID mice: a new model for the evaluation of vaginal microbicides. *AIDS* 2001;**15**(17):2231–8.

85. Cohen CJ, Molina JM, Cassetti I, Chetchotisakd P, Lazzarin A, Orkin C, et al. Week 96 efficacy and safety of rilpivirine in treatment-naive, HIV-1 patients in two Phase III randomized trials. *AIDS* 2013;**27**(6):939–50.
86. Jackson AG, Else LJ, Mesquita PM, Egan D, Back DJ, Karolia Z, et al. A compartmental pharmacokinetic evaluation of long-acting rilpivirine in HIV-negative volunteers for preexposure prophylaxis. *Clin Pharmacol Ther* 2014;**96**(3):314–23.
87. Kovarova M, Council OD, Date AA, Long JM, Nochi T, Belshan M, et al. Nanoformulations of rilpivirine for topical pericoital and systemic coitus-independent administration efficiently prevent HIV transmission. *PLoS Pathog* 2015;**11**(8):e1005075.
88. Fung HB, Stone EA, Piacenti FJ. Tenofovir disoproxil fumarate: a nucleotide reverse transcriptase inhibitor for the treatment of HIV infection. *Clin Ther* 2002;**24**(10):1515–48.
89. Kearney BP, Flaherty JF, Shah J. Tenofovir disoproxil fumarate: clinical pharmacology and pharmacokinetics. *Clin Pharmacokinet* 2004;**43**(9):595–612.
90. Destache CJ, Mandal S, Yuan Z, Kang G, Date AA, Lu W, et al. Topical tenofovir disoproxil fumarate nanoparticles prevent HIV-1 vaginal transmission in a humanized mouse model. *Antimicrob Agents Chemother* 2016;**60**(6):3633–9.
91. Gupta PN, Pattani A, Curran RM, Kett VL, Andrews GP, Morrow RJ, et al. Development of liposome gel based formulations for intravaginal delivery of the recombinant HIV-1 envelope protein CN54gp140. *Eur J Pharm Sci* 2012;**46**(5):315–22.
92. Karimunnisa S, Atmaram P. Mucoadhesive nanoliposomal formulation for vaginal delivery of an antifungal. *Drug Dev Ind Pharm* 2013;**39**(9):1328–37.
93. Vanić Ž, Hurler J, Ferderber K, Golja Gasparovic P, Škalko-Basnet N, Filipovic-Grcic J. Novel vaginal drug delivery system: deformable propylene glycol liposomes-in-hydrogel. *J Liposome Res* 2014;**24**(1):27–36.
94. Pattni BS, Chupin VV, Torchilin VP. New developments in liposomal drug delivery. *Chem Rev* 2015;**115**(19):10938–66.
95. Kish-Catalone TM, Lu W, Gallo RC, DeVico AL. Preclinical evaluation of synthetic –2 RANTES as a candidate vaginal microbicide to target CCR5. *Antimicrob Agents Chemother* 2006;**50**(4):1497–509.
96. Kish-Catalone T, Pal R, Parrish J, Rose N, Hocker L, Hudacik L, et al. Evaluation of -2 RANTES vaginal microbicide formulations in a nonhuman primate simian/human immunodeficiency virus (SHIV) challenge model. *AIDS Res Hum Retroviruses* 2007;**23**(1):33–42.
97. Agarwal S, Kumari PVK. Advances in Novasome technology—a review. *Int J App Pharm* 2013;**5**(1):1–4.
98. Konopka K, Davis BR, Larsen CE, Alford DR, Debs RJ, Düzgüneş N. Liposomes modulate human immunodeficiency virus infectivity. *J Gen Virol* 1990;**71**(Pt. 12):2899–907.
99. Malavia NK, Zurakowski D, Schroeder A, Princiotto AM, Laury AR, Barash HE, et al. Liposomes for HIV prophylaxis. *Biomaterials* 2011;**32**(33):8663–8.
100. Wheeler LA. Silencing sexually transmitted infections: topical siRNA-based interventions for the prevention of HIV and HSV. *Infect Dis Obstet Gynecol* 2014;**2014**:125087.
101. Wheeler LA, Trifonova R, Vrbanac V, Basar E, McKernan S, Xu Z, et al. Inhibition of HIV transmission in human cervicovaginal explants and humanized mice using CD4 aptamer-siRNA chimeras. *J Clin Invest* 2011;**121**(6):2401–12.
102. Wheeler LA, Vrbanac V, Trifonova R, Brehm MA, Gilboa-Geffen A, Tanno S, et al. Durable knockdown and protection from HIV transmission in humanized mice treated with gel-formulated CD4 aptamer-siRNA chimeras. *Mol Ther* 2013;**21**(7):1378–89.
103. Yang S, Chen Y, Ahmadie R, Ho EA. Advancements in the field of intravaginal siRNA delivery. *J Control Release* 2013;**167**(1):29–39.

104. das Neves J. Vaginal delivery of biopharmaceuticals. In: das Neves J, Sarmento B, editors. *Mucosal delivery of biopharmaceuticals: biology, challenges and strategies*. New York, NY: Springer; 2014. p. 261–80.
105. Kanasty R, Dorkin JR, Vegas A, Anderson D. Delivery materials for siRNA therapeutics. *Nat Mater* 2013;**12**(11):967–77.
106. Eszterhas SK, Ilonzo NO, Crozier JE, Celaj S, Howell AL. Nanoparticles containing siRNA to silence CD4 and CCR5 reduce expression of these receptors and inhibit HIV-1 infection in human female reproductive tract tissue explants. *Infect Dis Rep* 2011;**3**(2):e11.
107. Boyapalle S, Xu W, Raulji P, Mohapatra S, Mohapatra SS. A multiple siRNA-based anti-HIV/SHIV microbicide shows protection in both in vitro and in vivo models. *PLoS One* 2015;**10**(9):e0135288.
108. Leung V, Ko F. Biomedical applications of nanofibers. *Polym Adv Tech* 2011;**22**(3):350–65.
109. Onoe H, Takeuchi S. Cell-laden microfibers for bottom-up tissue engineering. *Drug Discov Today* 2015;**20**(2):236–46.
110. Blakney AK, Ball C, Krogstad EA, Woodrow KA. Electrospun fibers for vaginal anti-HIV drug delivery. *Antiviral Res* 2013;**100 Suppl.**:S9–S16.
111. Ball C, Woodrow KA. Electrospun fibers for microbicide drug delivery. In: das Neves J, Sarmento B, editors. *Drug delivery and development of anti-HIV microbicides*. Singapore: Pan Stanford; 2014. p. 459–507.
112. Huang C, Soenen SJ, van Gulck E, Vanham G, Rejman J, Van Calenbergh S, et al. Electrospun cellulose acetate phthalate fibers for semen induced anti-HIV vaginal drug delivery. *Biomaterials* 2012;**33**(3):962–9.
113. Huang C, Soenen SJ, van Gulck E, Rejman J, Vanham G, Lucas B, et al. Electrospun polystyrene fibers for HIV entrapment. *Polym Adv Tech* 2014;**25**(8):827–34.
114. Stoddard RJ, Steger AL, Blakney AK, Woodrow KA. In pursuit of functional electrospun materials for clinical applications in humans. *Ther Deliv* 2016;**7**(6):387–409.
115. Ball C, Krogstad E, Chaowanachan T, Woodrow KA. Drug-eluting fibers for HIV-1 inhibition and contraception. *PLoS One* 2012;**7**(11):e49792.
116. Ball C, Woodrow KA. Electrospun solid dispersions of maraviroc for rapid intravaginal preexposure prophylaxis of HIV. *Antimicrob Agents Chemother* 2014;**58**(8):4855–65.
117. Blakney AK, Krogstad EA, Jiang YH, Woodrow KA. Delivery of multipurpose prevention drug combinations from electrospun nanofibers using composite microarchitectures. *Int J Nanomed* 2014;**9**:2967–78.
118. Krogstad EA, Woodrow KA. Manufacturing scale-up of electrospun poly(vinyl alcohol) fibers containing tenofovir for vaginal drug delivery. *Int J Pharm* 2014;**475**(1–2):282–91.
119. Fernández-Romero JA, Deal C, Herold BC, Schiller J, Patton D, Zydowsky T, et al. Multipurpose prevention technologies: the future of HIV and STI protection. *Trends Microbiol* 2015;**23**(7):429–36.
120. Carson D, Jiang Y, Woodrow KA. Tunable release of multiclass anti-HIV drugs that are water-soluble and loaded at high drug content in polyester blended electrospun fibers. *Pharm Res* 2016;**33**(1):125–36.
121. Carballo-Diéguez A, Dolezal C, Bauermeister JA, O'Brien W, Ventuneac A, Mayer K. Preference for gel over suppository as delivery vehicle for a rectal microbicide: results of a randomised, crossover acceptability trial among men who have sex with men. *Sex Transm Infect* 2008;**84**(6):483–7.

122. Nel AM, Mitchnick LB, Risha P, Muungo LT, Norick PM. Acceptability of vaginal film, soft-gel capsule, and tablet as potential microbicide delivery methods among African women. *J Womens Health* 2011;**20**(8):1207–14.
123. Palmeira-de-Oliveira R, Duarte P, Palmeira-de-Oliveira A, das Neves J, Amaral MH, Breitenfeld L, et al. Women's experiences, preferences and perceptions regarding vaginal products: results from a cross-sectional web-based survey in Portugal. *Eur J Contracept Reprod Health Care* 2015;**20**(4):259–71.
124. Woodsong C, Holt JD. Acceptability and preferences for vaginal dosage forms intended for prevention of HIV or HIV and pregnancy. *Adv Drug Deliv Rev* 2015;**15**(92):146–54.
125. das Neves J, Sarmento B. Antiretroviral drug-loaded nanoparticles-in-films: a new option for developing vaginal microbicides? *Expert Opin Drug Deliv* 2016;**14**(4):449–52.
126. Elias C, Coggins C. Acceptability research on female-controlled barrier methods to prevent heterosexual transmission of HIV: where have we been? Where are we going? *J Womens Health Gend Based Med* 2001;**10**(2):163–73.
127. Rohan LC, Zhang W. Vaginal microbicide films. In: das Neves J, Sarmento B, editors. *Drug delivery and development of anti-HIV microbicides*. Singapore: Pan Stanford; 2014. p. 291–330.
128. Gu J, Yang S, Ho EA. Biodegradable film for the targeted delivery of siRNA-loaded nanoparticles to vaginal immune cells. *Mol Pharm* 2015;**12**(8):2889–903.
129. Srinivasan P, Zhang J, Martin A, Kelley K, McNicholl JM, Buckheit Jr RW, et al. Safety and pharmacokinetics of quick dissolving polymeric vaginal films delivering the antiretroviral IQP-0528 for pre-exposure prophylaxis. *Antimicrob Agents Chemother* 2016;**60**(7):4140–50.
130. Machado A, Cunha-Reis C, Araújo F, Nunes R, Seabra V, Ferreira D, et al. Development and in vivo safety assessment of tenofovir-loaded nanoparticles-in-film as a novel vaginal microbicide delivery system. *Acta Biomater* 2016;**44**:332–40.
131. Cunha-Reis C, Machado A, Barreiros L, Araújo F, Nunes R, Seabra V, et al. Nanoparticles-in-film for the combined vaginal delivery of anti-HIV microbicide drugs. *J Control Release* 2016;**243**:43–53.
132. Barreiros L, Cunha-Reis C, Silva EM, Carvalho JR, das Neves J, Sarmento B, et al. Development and validation of a liquid chromatography-MS/MS method for simultaneous quantification of tenofovir and efavirenz in biological tissues and fluids. *J Pharm Biomed Anal* 2016;**136**:120–5.

SUBCHAPTER

Surface-enhanced Raman scattering (SERS) methods for diagnosis of infectious diseases

1.3

Carme Catala*, Nicolas Pazos-Perez*, Luca Guerrini*, Ramon A. Alvarez-Puebla*,**

**Rovira i Virgili University, Tarragona, Spain; **Catalan Institution for Research and Advanced Studies, Barcelona, Spain*

1 INTRODUCTION

Despite the progress in modern medicine, infections continue to represent one of the greatest challenges facing humanity. Such type of infections can be broadly divided into two main categories according to the location of the patient at the time the infection developed: (1) community-acquired and (2) nosocomial (hospital-acquired) infections. Nosocomial infections occur worldwide and affect both developed and resource-poor countries, and they are mostly related to infections of surgical wounds, as well as the urinary and lower respiratory tracts.[1]

Infections acquired in healthcare settings are among the major causes of death and increased morbidity among hospitalized patients, leading, consequently, to a remarkable increase in healthcare costs (only in Europe the estimated costs are €7 billion per year, including direct costs only, and reflecting 16 million extra days of hospital stay[2]). The European Centre for Disease Prevention and Control (ECDC) estimates that nosocomial infections contributed to 50,000 deaths only in Europe in 2011 and that an average of 7.7% of hospital patients had nosocomial infections in Europe (>2 million individuals annually) and almost 9% worldwide.[1] The increased length of stay for infected patients is the greatest contributor to costs. One study showed that the overall increase in the duration of hospitalization for patients with surgical wound infections was 8.2 days, ranging from 3 days for gynecology to 9.9 days for general surgery and up to 19.8 days for orthopedic surgery. Prolonged stay not only increases direct costs to patients or payers, but also indirect costs due to lost work. The advancing age and the greater prevalence of chronic diseases among admitted patients, as well as the increased use of diagnostic and therapeutic procedures, which affect the host defenses, will provide continuing pressure on nosocomial infections in the future. The increased use of drugs, the need for isolation, and the use of additional laboratory and other diagnostic studies also contribute to costs. Additionally, rapid and long-range human mobility is now responsible for the fast geographical spread of infectious disease, making the fight against infections to be tackled globally. Nowadays, mobility and traffic have reached a complexity and volume of an unprecedented degree. More than 60 million people travel billions of miles on more than 2 million international flights each week.[3] Hundreds of millions of people

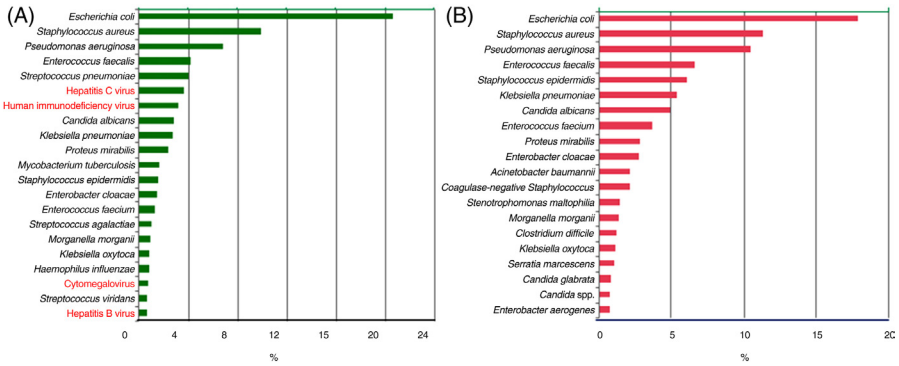

FIGURE 1.3.1

Most prevalent pathogens in (A) community-acquired and (B) nosocomial infections. Viral agents are shown in *gray* (*red* in the web version).

Data obtained from European Prevalence Survey of Healthcare-Associated Infections and Antimicrobial Use (EPPS) 2012.

commute on a complex web of highways and railroads, most of which operate at their maximum capacity. Despite this increasing connectivity and our ability to visit virtually every place on this planet in a matter of days, the magnitude and intensity of modern human traffic have made human society more susceptible to threats intimately connected to human travel.

Notably, although both community-acquired and nosocomial infections can be due to many agents, 95% of the infections can be ascribed to around 30 microorganisms (Fig. 1.3.1).

The time at which effective antimicrobial therapy is initiated is known to be the single strongest predictor of outcome, as even a delay of an hour in its administration increases the risk of death by 8%.[4,5] Besides the obvious economic benefits, the development of fast, accurate, and inexpensive diagnostic methods thus appears as a major goal for alleviating human pain. Conventional microbial typing methods are reliable, but suffer from inherent time-consuming complexities. Among these methods, the most common one remains the culture of the microorganism in different media to isolate the species and identify its nature (Fig. 1.3.2A). Sequential cultures can be avoided by implementing mass spectrometry (MS) techniques for the identification of isolated pure colonies (Fig. 1.3.2B). These methods, including the identification by MS, require of time for the agent to grow (24–72 h). On the other hand, immunological tests to identify microorganisms are also popular. Immunological techniques, such as enzyme-linked immune sorbent assay (ELISA, Fig. 1.3.2C), fluorescence immune assay (FIA), or radioimmunoassay (RIA) offer faster results but cannot be considered as multiplex assays. Further, they require a considerable amount of sample and are expensive (€100 for each analytical kit or €100,000 for an automatized system). To increment portability, a new fluorescence immune assay–like technique known as lateral flow immunochromatography has been recently

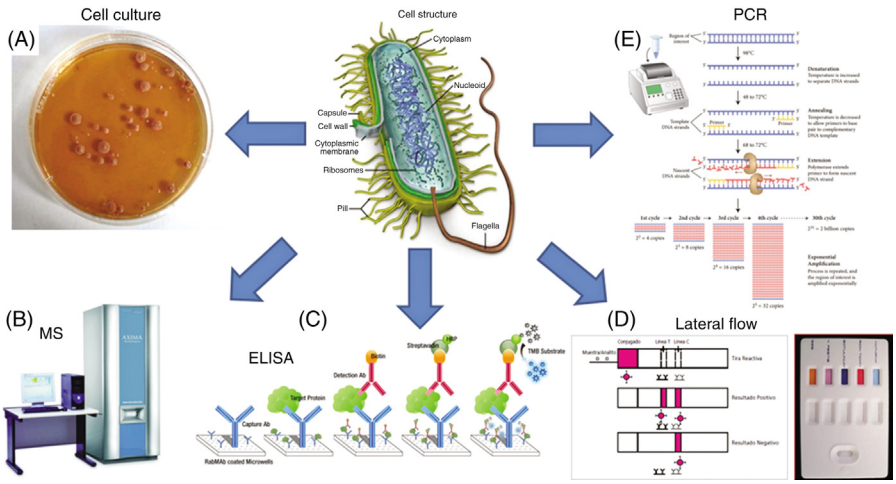

FIGURE 1.3.2 Some Examples for the Actual Detection of Microorganisms in Clinical Diagnosis.

(A) Cell culture, (B) mass spectrometry (MS) of isolated pure colonies, (C) enzyme-linked immune sorbent assay (ELISA), (D) Lateral flow immunochromatography, and (E) polymerase chain reaction (PCR).

developed (Fig. 1.3.2D). This method is simple, the chemicals can be stored for certain time, and offers results that can be easily interpreted with the naked eye (i.e., it does not require extensively trained personnel). However, each reactive strip necessary to identify a single given agent in a single given sample is about €200. Furthermore, this method suffers from poor sensitivity and, thus, accumulation of microorganisms in the sample is a necessary step to allow positive detection of the target. Alternatively, some labs are introducing the polymerase chain reaction (PCR) to identify microorganisms through the profiling of their genetic code (Fig. 1.3.2E). This technique is quantitative and semimultiplex, but also laborious, slow, and expensive (€250 each analysis of sample). Overall, it can be concluded that the current methods for detection of microorganisms are flawed, with problems related to sensitivity, selectivity, speed, price, and technological restrictions. In this scenario, surface-enhanced Raman scattering (SERS) spectroscopy offers an exceptional opportunity for the development of new sensing devices amenable to implementation of quantitative multiplex analysis in real time.[6]

The application of nanostructured materials toward the development of novel detection techniques with improved sensitivity and/or simplified and faster applicability has rapidly become an appealing alternative to other technologies. Among them, SERS is a powerful analytical technique that has already proven to be particularly effective in environmental detection and monitoring applications. Essentially, SERS can be described as the Raman scattering amplified by the presence of a plasmonic structure in close vicinity to the target analyte. In such a case, the main cause of the excitation of

vibrational levels of the molecule is the collective oscillation of conduction electrons of the metal upon excitation with the appropriate light. This generates an ultrastrong electromagnetic near-field in the proximity of the nanostructure surface (known as localized surface plasmon resonances). As Raman scattering, SERS provides a complex spectral pattern that contains all the compositional and structural characteristics of the molecule under study.[7] SERS, as Raman, is also characterized by extreme experimental flexibility, as Raman measurements can be carried out over a wide spectral range, are insensitive to air and water, and require no sample preparation.

Recent spectacular advances in nanofabrication techniques fuelled the development of a large variety of rationally designed SERS substrates with an optimized, uniform, and reproducible response. This successfully translated the outstanding analytical potential of SERS to reliable, widely accepted, and commercially viable sensing applications. The dependence of localized surface plasmon resonances on parameters, such as size, shape, composition, and surrounding medium, provides multiple possibilities for tuning the optical response and, thus, optimizing the SERS performance of the plasmonic nanostructure for a specific application. In conjunction with the control of the signal amplification provided by the optical enhancer, a key step in the practical implementation of sensing applications (including SERS) is the appropriate chemical functionalization of the "bare" metallic surface. This step is necessary to impart the required selectivity and/or sensitivity toward the target analyte, especially in complex mediums. Two design approaches are commonly used to devise plasmonic nanostructures as SERS sensing platforms: (1) direct SERS and (2) encoded particles. In direct SERS, the detection is achieved by directly acquiring the SERS spectrum of the analyte. However, when performing direct SERS, several other species besides the target molecules can be detected simultaneously, thus hampering the application of this strategy when complex analytical matrixes are involved, such as those in biological or environmental applications. In fact, when the number of targets and background species is high, the overlapping of vibrational modes of different molecules is very likely, hence making the interpretation of the overall vibrational spectrum extremely difficult or nearly impossible. On the other hand, SERS-encoded particles can be typically prepared by using an efficient plasmonic substrate that is labeled with a SERS molecule, protected with an external inert layer, and functionalized with the appropriate selective chemoreceptor [such as an antibody (*Ab*) or an aptamer]. In this case, the identification and quantification of the analyte are indirectly correlated to the presence and intensity of the specific SERS label.

2 PLASMONIC MATERIALS FOR DIAGNOSIS OF INFECTIOUS DISEASES

A critical aspect in the implementation of a SERS-based sensing strategy for microorganism detection relies on the preparation of the appropriate plasmonic materials. In general, the format and functionalization of the plasmonic materials are dictated by the selected strategy (i.e., either direct SERS or by using encoded nanoparticles).

The task of finding "the universal SERS substrate" is not trivial and may not even be the right approach for implementing SERS as an analytical tool. For practical quantitative analytical applications, SERS must fulfill the typical requirements of an analytical technique: reproducibility of the results, linearity of the response, standardization, molecular selectivity, and clear methodology for sample preparation. Unfortunately, these requirements are not easily met in the case of SERS experiments. Chemical and electronic effects must be carefully controlled to bring SERS as close as possible to the basic analytical requirements. SERS can be maximized mainly through control of two main factors: (1) careful design of the optical substrate and (2) its appropriate functionalization.

Regarding the optical substrate, SERS has been mainly obtained in nanostructured thin films and colloidal nanoparticles.[8–10] Colloidal nanoparticles are advantageous for many reasons. Their versatility and ease of synthesis with a high degree of control over the composition, shape, and size, make them by far, the most commonly used substrates in SERS. Through careful control of these three key factors (composition, size, and shape), the optical and plasmonic properties can be tuned to maximize the SERS enhancement.[11]

The composition of the metallic nanoparticles deeply affects the intensity of the SERS signal. In this respect, the most important SERS platforms so far have been made of silver and gold,[12] while research using other materials (such as Cu, Pd, Pt, Rh, CuTe, Si, etc.)[13] is still marginal. In general, it can be stated that silver is a much more efficient optical material than gold, giving rise to SERS signals over 2 orders of magnitude higher than those of gold, as silver scattering contribution is larger than that of gold.[14] Additionally, silver can be excited with radiation ranging from UV to IR, while gold is restricted to the red or IR spectrum owing to damping by the interband transitions. As a consequence, silver nanoparticles are preferred when dealing with practical applications. However, it is worth noting that gold nanoparticles not only permit a better control of particle size and shape, but are also significantly more stable and biocompatible.[15–17]

Currently many methods are available for obtaining colloids with high SERS activity, but this topic continues to be a booming research field. Within the limits of wet chemistry, colloidal methods can be divided in a variety of processes, including chemical reduction, laser ablation, or photoreduction, the first one being the most commonly used.[11,18] The chemical reduction usually comprises a metallic salt (precursor), which is reduced by a chemical agent to produce colloidal dispersions that contain particles of different sizes and variable shapes. Regarding the synthesis of silver nanoparticles, tuning of the size and shape properties is much more difficult to achieve than in the case of gold due to higher reactivity of silver, which limits the extent of control that can be exerted over the selective growth at different crystal facets.[19]

However, many synthetic processes have been described to obtain differently sized and shaped nanoparticles, including seed-mediated, polyol, biological, hydro/solvothermal, galvanic replacement, photochemical, electrochemical, or template-mediated synthesis,[20–23] which give rise to highly monodisperse colloids in shape and

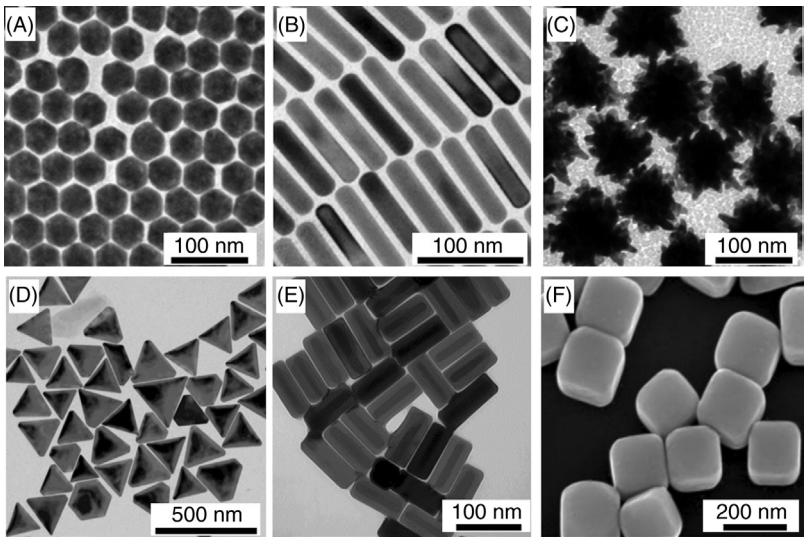

FIGURE 1.3.3 Transmission Electron Microscopy (TEM) Images of Nanoparticles With Different Shapes, Sizes, and Composition.

(A) Gold nanospheres, (B) gold nanorods, (C) silver nanoplates, (D) gold nanostars, (E) silver nanobars, and (F) silver nanocubes.

Figures adapted with permission from Pazos-Perez N, Garcia de Abajo FJ, Fery A, Alvarez-Puebla RA. From nano to micro: synthesis and optical properties of homogeneous spheroidal gold particles and their superlattices. Langmuir *2012;**28**(24):8909–14*[25]*; Ye X, Zheng C, Chen J, Gao Y, Murray CB. Using binary surfactant mixtures to simultaneously improve the dimensional tunability and monodispersity in the seeded growth of gold nanorods.* Nano Lett *2013;**13**(2):765–71*[26]*; Liebig F, Sarhan RM, Prietzel C, Reinecke A, Koetz J. "Green" gold nanotriangles: synthesis, purification by polyelectrolyte/micelle depletion flocculation and performance in surface-enhanced Raman scattering.* RSC Adv *2016;**6**(40):33561–8*[27]*; Sun Y, Xia Y. Shape-controlled synthesis of gold and silver nanoparticles.* Science *2002;**298**(5601):2176–9.*[28]

size. Among these methods, the seed-mediated growth process is the most widely used when dealing with shape-controlled nanoparticle synthesis. This protocol includes a two-step process in which the first step consists of the generation of very small spherical particles. In the second step, the particles grow anisotropically in a different direction due to the reduction of metal salts on the surface of the initial seed nanoparticles. The presence of preformed seeds is highly advantageous, as the particle size distribution becomes significantly narrower. The control of experimental variables, such as the concentration of the metal salt, reducing agent, growth speed, temperature, capping agent, or chosen solvent, provides a broad range of differently sized and shaped nanoparticles (Fig. 1.3.3).[18,24]

Besides the simplicity of the synthetic methods, "as-prepared" metal nanoparticles present remarkable advantages when dealing with diagnostic systems in biofluids, as they permit direct SERS analysis within the analyte natural solution medium; they present a large surface area and good dispersion in liquids that allows for a close

adsorbent–adsorbate interaction, so that the analyte can be naturally retained onto the nanoparticles' surface; the Brownian motion of the analyte–particle complexes minimizes damage to the sample, even when more energetic laser lines and higher power at the sample for excitation are used; and, fundamentally they allow for the screening of large volumes of fluids, as required in the modern clinical practice for diagnosing infectious diseases.

3 FABRICATION AND LABELING OF SERS-ENCODED NANOPARTICLES

Despite all the advantages mentioned earlier, bare plasmonic nanoparticles are usually not enough for the appropriate recognition of complex analytes, such as microorganisms. Direct SERS spectra of microorganism usually show common spectral patterns, especially when studying closely related species. Additionally, if the goal of the method is the determination of the microorganism directly in the biological matrix, the chemical species present will overlap the microorganism SERS spectra, making the interpretation of the result impossible. Thus, as an alternative, SERS can be used as a labeling method in a similar way as fluorophores are used in immunology bioassays.[29] Although fluorescence is powerful and convenient, the lack of features in the obtained spectra (usually composed of just one broad feature) limits the number of analytes that can be recognized with certainty. Thus, the use of SERS as an encoding alternative is rapidly gaining relevance not only due to its unprecedented detection limits that dramatically decrease the detection times, but also owing to the practically unlimited number of barcodes that can be used for simultaneous detection.

The fabrication and characteristics (such as material, size, biocompatibility, and others) of the desired SERS-encoded particles strongly depend on each specific application. However, all of them share some common requirements: (1) presence of an optical enhancer (i.e., the plasmonic nanomaterial), (2) addition of a SERS code, and (3) protection with a silica or polymer layer to prevent leaching of the SERS reporter, while providing a suitable surface for biofunctionalization[30] and colloidal stability (Fig. 1.3.4). The first reported works using SERS-encoded particles for multiplex determination relied either on the addition of a SERS tag directly onto the plasmonic particles or on the precoupling of the tag to the biomolecular interface.[31] Nowadays, the preparation of SERS-encoded particles is becoming more exotic. The simplest way to produce SERS-encoded nanoparticles comprises the SERS codification of single spherical plasmonic colloids and encapsulation within silica or polymer shells.[32–34] On the other hand, silica coating of nanoparticles is also a mature technology.[35] Thus, the key step for the codification of single nanoparticles relies on the incorporation of the Raman label to give rise to a signal as strong as possible without compromising colloidal stability. The formation of the protective shell around the single colloidal particle inhibits plasmon coupling and, in turn, the generation of hot spots (specific gaps between particles where the electromagnetic field is extremely

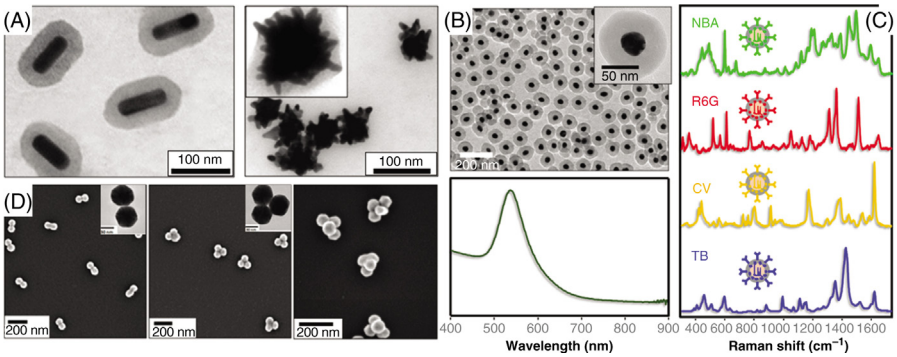

FIGURE 1.3.4

(A) Some examples of encoded plasmonic nanostructures, including single-particle rods or stars and dimers, trimers, and tetramers of spheres. (B) Encoded gold spheres and their plasmonic response. (C) Surface-enhanced Raman scattering (SERS) response of encoded (gold spheres) with four different SERS labels. *CV*, Cystal violet; *NBA*, nile blue A; *R6G*, rhodamine 6G; *TB*, toluidine blue.

Figures adapted with permission from Fernández-López C, Mateo-Mateo C, Alvarez-Puebla RA, Pérez-Juste J, Pastoriza-Santos I, Liz-Marzán LM. Highly controlled silica coating of PEG-capped metal nanoparticles and preparation of SERS-encoded particles. Langmuir *2009;**25**(24):13894–9*[32]*; Mir-Simon B, Reche-Perez I, Guerrini L, Pazos-Perez N, Alvarez-Puebla RA. Universal one-pot and scalable synthesis of SERS encoded nanoparticles.* Chem Mater *2015;**27**(3):950–8*[57]*; Pazos-Perez N, Wagner CS, Romo-Herrera JM, Liz-Marzán LM, García de Abajo FJ, Wittemann A, et al. Organized plasmonic clusters with high coordination number and extraordinary enhancement in surface-enhanced Raman scattering (SERS).* Angew Chem Int Ed *2012;**51**(51):12688–93.*[58]

high due to coupling between their plasmon resonances[36,37]). Even though the recent demonstration of the heterogeneous distribution of plasmon modes within anisotropic particles[38,39] is leading to the development of highly active nanoparticles such as nanostars or lace nanoshells[40,41] (Fig. 1.3.4), still the most popular approach for the fabrication of nanometer-sized SERS-encoded particles is the use of nanoparticle aggregates as plasmonic cores. Particle aggregation can be easily promoted by changing the solvent, increasing the ionic strength of the suspension,[42] or just spontaneously due to the adsorption of the Raman label.[43] Notwithstanding, these uncontrollable aggregation processes are usually undesired because they lead to a random distribution of hot spots with subsequent signal heterogeneity from cluster to cluster. Thus, several approaches were developed toward controlling aggregation. One of the oldest and probably most successful approaches comprises the so-called composite organic–inorganic nanoparticles (COIN).[44–46] The COIN approach consists of controlled label-induced aggregation of silver particles. An external shell of bovine serum albumin (BSA) is spontaneously retained onto the COIN; it not only protects the code, but also allows for further functionalization with biomolecules, such as proteins (antibodies). Other strategies for the generation of aggregated encoded particles relies on the induction of aggregation by an increase in the ionic strength, followed

by a silica coating of silver or gold colloids.[47,48] In fact, these particles have recently been demonstrated to give rise to a sufficiently intense signal to enable individually identification in a Raman flow cytometer.[49] Nevertheless, both methods still yield uncontrollable aggregates with ensuing fluctuations in their SERS intensities. For this reason, an increasing activity is observed for the development of controlled methods for the fabrication of SERS active dimers, including spheres, cages, pyramids, or even rods[50–56] (Fig. 1.3.4).

4 DIRECT SERS ANALYSIS OF BACTERIA

The most common approach for SERS analysis of bacteria relies on the acquisition of the intrinsic SERS spectra of the microorganisms placed in direct contact with the SERS substrate. Traditionally, this was achieved by simply drying a mixture of unfunctionalized "naked" silver nanoparticles and highly concentrated bacteria onto an appropriate Raman spectroscopy substrate, prior to spectral acquisition (Fig. 1.3.5A).[59–62] A large number of SERS spectra are then collected over different points to improve the statistical reliability and reproducibility of the final bacterial fingerprint (Fig. 1.3.5B). Chemometrics is finally applied for positive identification and discrimination between bacteria (Fig. 1.3.5C).

In this scenario, the SERS spectra are the sole result of the contributions from the components of the bacterial membrane. Nonetheless, the final spectral profile has shown to be extremely sensitive to several experimental factors, such as colloidal properties and sample preparation.[59] In particular, the rather nonhomogeneous distribution of the nanoparticles onto the bacterial walls significantly limits the spectral reproducibility and hampers any quantitative estimation of the target concentration.

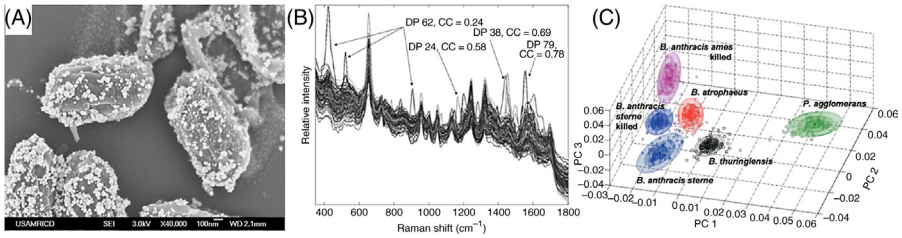

FIGURE 1.3.5

(A) Scanning electron microscopy (SEM) image showing coverage of silver nanoparticles on *Bacillus atrophaeus* spores. (B) One hundred and ten *B. atrophaeus* spore spectra overlaid showing good signal reproducibility. (C) Principal component analysis plot showing discrimination between five *Bacillus* spore samples and *Pantoea agglomerans*. *CC*, Cross-correlation value; *DP*, data point.

Figure adapted with permission from Guicheteau J, Argue L, Emge D, Hyre A, Jacobson M, Christesen S. Bacillus *spore classification via surface-enhanced Raman spectroscopy and principal component analysis.* Appl Spectrosc *2008;**62**(3):267–72.*[61]

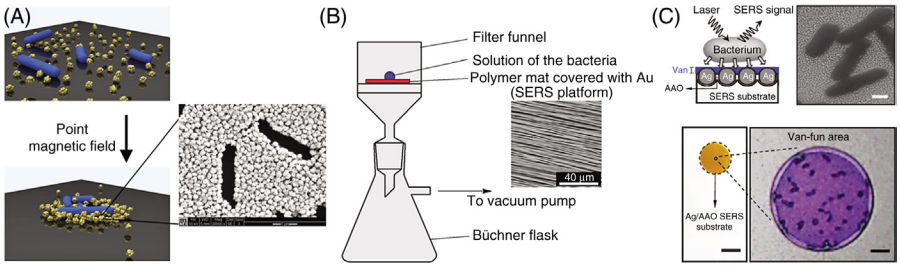

FIGURE 1.3.6

(A) Schematics of the condensation process of magnetic gold nanoparticles and bacteria, together with a SEM image within the area of analysis (bacteria are shown in *dark contrast*, the scale bars is 1 μm). (B) Scheme of embedding bacteria on the SERS platform directly from the solution and SEM image of the polymer mats (PLLA-b) covered with 90 nm of gold. (C) Schematic diagram showing the cross-sectional view of a bacterium on a vancomycin (Van)-coated substrate. SEM images of bacteria on the substrate (scale bar 500 nm) plus an optical image of the Van-coated region with the captured *E. coli* (scale bar 5 μm). *AAO*, Anodic aluminum oxide; *van-fun area*, vancomycin-functionalized area.

Part A, Figure adapted with permission from Zhang L, Xu J, Mi L, Gong H, Jiang S, Yu Q. Multifunctional magnetic–plasmonic nanoparticles for fast concentration and sensitive detection of bacteria using SERS. Biosens Bioelectron *2012;**31**(1):130–6*[63]*; part B, Figure adapted with permission from Szymborski T, Witkowska E, Adamkiewicz W, Waluk J, Kamińska A. Electrospun polymer mat as a SERS platform for the immobilization and detection of bacteria from fluids.* Analyst *2014;**139**(20):5061–4*[64]*; part C, Figure adapted with permission from Liu TY, Tsai KT, Wang HH, Chen Y, Chen YH, Chao YC, et al. Functionalized arrays of Raman-enhancing nanoparticles for capture and culture-free analysis of bacteria in human blood.* Nat Commun *2011;**2**:538.*[65]

Several new approaches were developed to solve this problem, with a reduction in the bacterial concentration required to achieve a detectable signal. For instance, magnetic–plasmonic core–shell nanoparticles were used in place of traditional colloids to enable a high concentration of bacteria by applying an external point magnetic field. As a result, a large number of microorganisms and nanoparticles can be effectively condensed into a highly compact dot (Fig. 1.3.6A).[63] On the other hand, Szymborski et al.[64] combined periodic structures of nanosized fibers with nanostructured gold layers to be used as a dual-efficient SERS filter for the immobilization of bacteria from solutions, such as blood, urine, water, or milk (Fig. 1.3.6B).

In addition to mechanical forces, other strategies exploiting biochemical interactions have been developed to this purpose. A paradigmatic example is represented by the work of Wang and coworkers.[65] SERS-active silver nanoparticle arrays were coated with vancomycin (Van), an antibiotic used to treat a number of bacterial infections. Profiting from the high binding affinity of bacteria toward Van, a 1000-fold increase in bacteria capture from biofluids (saliva, phlegm, or blood) was achieved without the introduction of significant spectral interference (Fig. 1.3.6C). Van-coated SERS substrates acted both as a bacteria-capturing tool and an efficient sensing

platform for the identification of SERS fingerprints of the targeted bacteria. The authors reported a concentration of 30% of *Enterococcus* was present in 1 mL o water (10^2 cfu/mL) that was added onto a microscopic Van-coated area of 707.14 μm^2 (30-μm diameter). This microscopic localization helps to reduce the laborious procedure required to locate the bacteria on the substrate and therefore facilitate their subsequent sensing by SERS.

5 INTEGRATED SERS MICROFLUIDIC DEVICES AND SERS-ENCODED NANOPARTICLES

Despite all the improvements regarding sample manipulation and concentration, the traditional approach to the direct SERS analysis of bacteria dried on a solid substrate has major issues in terms of spectral fluctuations, extremely long measuring time to acquire statistically reliable datasets, and lack of quantitative response.[66,67] These limitations can be potentially addressed by combining SERS with microfluidics.

Recent advances in the microfabrication have led to the development of novel microflowing systems for bioparticle separation and analysis. Implementation of microfluidics and biosensor technologies provides the ability to manage and integrate chemical and biological components into a single platform, offering the opportunity for developing portable, autonomous, and disposable devices capable of performing real-time detection, unprecedented accuracies, and simultaneous analysis of different analytes in a single device.[68] Microsystems are already revolutionizing the way we do science and have led to the development of a number of ultrasensitive bioanalytical devices capable of analyzing complex biological samples.[69,70]

Popp and coworkers[66,71] provided the first example of flow-through SERS measurements of bacterial samples in a microfluidic device (Fig. 1.3.7A). Such an approach drastically reduced the acquisition time, while improving spectral reproducibility through the analysis of the sample in suspension. Initially, the authors demonstrated the efficiency of this SERS microfluidic device in the classification of nine different precultivated *Escherichia coli* strains (buffered solutions, ca. 8×10^7 cells/mL).[66] Subsequently, six different species of precultivated mycobacteria (buffered solutions, concentration range from ca. 4 to 40×10^7 cells/mL) were successfully identified.[71] In this latter work, a bead-beating module for the disruption of the bacterial cells was combined with the microfluidic device (Fig. 1.3.7B), leading to an automated closed system for sample preparation and measurement. Disruption of the bacterial membrane allows the colloidal silver nanoparticles to interact with all cell components rather that the bacterial walls alone. As a result, richer spectral information is available in the SERS spectra, thus improving the overall discrimination capabilities via chemometric methods.

As the ultimate goal for bacterial identification is the complete bypassing of the cultivation step, concentration procedures were then implemented into SERS microfluidics biosensors, mostly based on microfluidic dielectrophoresis (DEP).[72–75] In DEP, nonuniform electric fields are exerted on dielectric particles, including cells

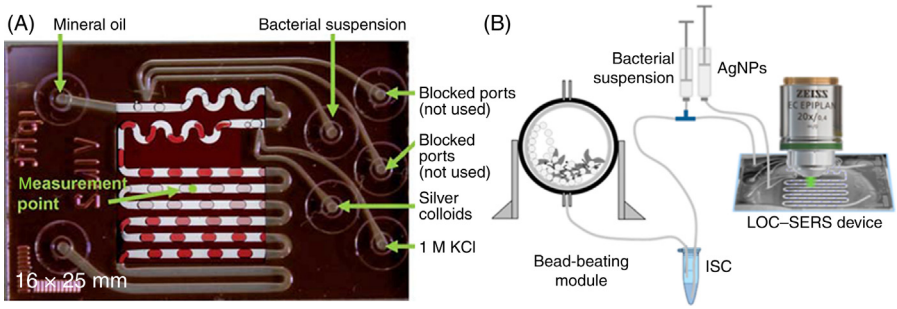

FIGURE 1.3.7

(A) Application of two-phase liquid/liquid segmented flow in a microfluidic chip for the acquisition of Raman spectra of the separation medium oil and SERS spectra within the droplets at the measurement point in the second channel. (B) Scheme of sample preparation, including the sample lysing module (bead-beating system) for the bacterial cell disruption, the internal storage container (ISC), the syringe pump system, and the droplet-based microfluidic device mounted to the microscope stage. *AgNPs*, Silver nanoparticles; *LOC*, lab on a chip.

Part A, Figure adapted with permission from Walter A, März A, Schumacher W, Rösch P, Popp J. Towards a fast, high specific and reliable discrimination of bacteria on strain level by means of SERS in a microfluidic device. Lab on a Chip *2011;**11**(6):1013–21.*[66]

and microorganisms, to control their location.[76] Cheng et al.[72] combined a short-range DEP and long-range AC electroosmosis flows to rapidly and selectively concentrate pathogens in the diluted human blood sample at the stagnation area on a SERS-active roughened electrode. The high density of bacteria aggregates at the measuring spot achieved intense SERS fingerprints of *Staphylococcus aureus*, *E. coli*, and *Pseudomonas aeruginosa* spiked into blood down to ca. 10^3 cfu/mL. Typically, 50 µL of 20-time diluted human whole blood sample spiked with pathogens (dilution is necessary to avoid blood cell coagulation) were dropped onto the chips and subjected to AC excitation for 3 min (ca. 40%–50% capture efficiency onto the stagnation area was achieved) before being investigated by SERS for 5 min.

Microfluidic DEP devices were also integrated with SERS using encoded nanoparticles for the detection of bacteria. Madiyar et al.[73] captured and concentrated *E. coli* DHα5 cells coated with SERS tags on a nanoelectrode array placed at the bottom of a microfluidic chip (Fig. 1.3.8). The SERS signal was successfully measured during DEP capture with single-bacterium sensitivity and a quantitative response in the 5 to 1×10^9 cfu/mL range (buffered solutions). The SERS-encoded nanoparticles consisted of iron oxide–gold core–shell nanoparticles initially coated with thiolated PEG. They were infused with a Raman reporter and finally conjugated with a selective Ab. Typically, the bacteria and antibody-conjugated SERS-encoded nanoparticle solutions were mixed together and incubated overnight at 4°C. Several centrifugation/washing cycles were further applied to remove the excess unbound particles

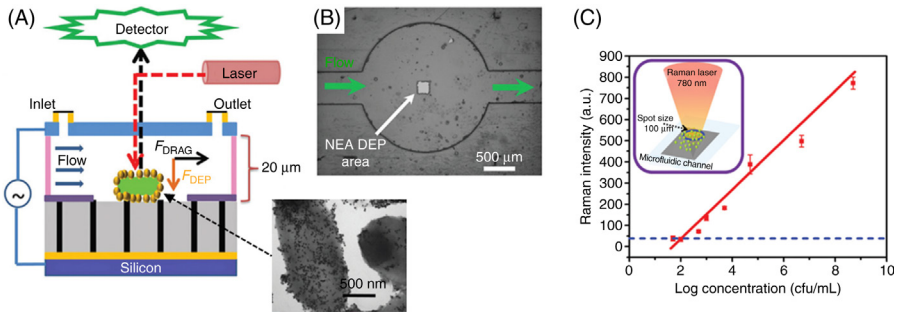

FIGURE 1.3.8

(A) Outline of the dielectrophoresis (DEP) capture of the bacteria coated with SERS-encoded nanoparticles for the Raman detection. A representative TEM of *E. coli* DHα5 bacterial cells attached with SERS-encoded nanoparticles is also included. (B) Optical microscope image taken under 4× magnification showing the microfluidic channel and the active square at the center. (C) SERS intensity from the samples with the bacterial concentrations in the 5 to 1.0 × 10^9 cfu/mL range (DEP capture time = 50 s). The inset shows a 100-μm diameter laser focal spot aligned with a 200 × 200 μm^2 active DEP area. *NEA*, Nanoelectrode array.

Figure adapted with permission from Madiyar FR, Bhana S, Swisher LZ, Culbertson CT, Huang X, Li J. Integration of a nanostructured dielectrophoretic device and a surface-enhanced Raman probe for highly sensitive rapid bacteria detection. Nanoscale *2015;**7**(8):3726–36.*[73]

before analysis. Bacteria detection was also successfully performed in more complex media spiked with 5 × 10^5 cfu/mL *E. coli* cells.

Lin et al.[74] exploited a DEP microfluidic device for trapping individual microorganisms in a defined location in space for their in situ investigation with a confocal micro-Raman system. Clusters of gold nanoparticles aggregated in the presence of dye molecules where silica-coated and bioconjugated with Ab were to be used as SERS-encoded nanoparticles. Buffered suspensions of two bacteria (*Salmonella enterica* serotype Choleraesuis and *Neisseria lactamica*) were mixed with SERS-encoded particles and incubated for 1 h at room temperature before being subjected to multiple centrifugation/washing cycles to eliminate unbound nanoparticles prior to DEP–Raman analysis. The practical detection limit with a 10-min measurement time was estimated to be 70 cfu/mL, while the total assay time, including sample pretreatment, was less than 2 h (no quantitative response was reported).

With the aim of improving the detection specificity and signal enhancement by reducing the miss binding, Wang et al.[75] recently developed a biosensor using a three-epitope detection scheme to avoid the antibody–antigen binding failures, which may occur in the one-epitope setup. Here, different SERS-encoded nanoparticles were conjugated with three monoclonal antibodies that bind to three different membrane receptors. Buffered suspensions of *E. coli* O157:H7 preconcentrated via a DEP microfluidic device were then incubated with the mixture of SERS-encoded nanoparticles. SERS analysis was performed on droplets of sample solutions placed

on a gold-coated microscope slide. In this setup, only SERS signals consisting of the superimposed contributions of the different SERS tags were associated with positive recognition events. Limits of detection down to 1 cfu/mL were reported.

Unfortunately, while the sensitivity issue has been addressed by some of these methods, only small volumes (~microliters) of samples, which are normally not relevant for clinical diagnosis, can actually be investigated. Further, additional steps to record a suitable signal for identification are often required. Recently, our group reported the fabrication of a novel microorganism optical detection system (MODS, Fig. 1.3.9A) for the real-time, multiplexed pathogen identification and quantification (down to the single colony-forming unit detection) through fast screening of large body fluid volumes (10 min/mL of blood) as required by standard medical practice for the analysis of biological samples.[77]

As for previous sensing schemes, mixing of bacteria-containing fluids with antibody-functionalized SERS-encoded silver nanoparticles induced the accumulation of the particles at the bacterial membrane. In our case, however, SERS-encoded particles were designed so as to yield, upon adhesion onto the bacteria walls, a dense array of interparticle gaps in which the Raman signal is exponentially amplified by several orders of magnitude relative to the dispersed particles. Incubation time was optimized to maximize the nanoparticle coating up to the saturation point (~60%), while avoiding the unwanted flocculation of bacteria overloaded with nanoparticles (Fig. 1.3.9B). Under this scenario, the sample can be directly pumped through a millifluidic channel where a backscattered detecting laser continuously monitors the liquid stream, therefore removing the need of time-consuming centrifugation/washing cycles prior to the SERS analysis. In fact, positive events associated with a nanoparticle-coated colony-forming unit traversing the laser focus generate SERS intensities well above the background of dispersed encoded nanoparticles. For a demonstration of bacteria detection, we successfully and simultaneously quantified three different types of bacteria (*S. aureus*, *E. coli*, and *Streptococcus agalactiae*) at a rate of 13 min/mL of blood or serum (Fig. 1.3.9C) and at concentrations ranging from units to tens of colony-forming unit per milliliter. Notably, no false identifications were observed in any of the analyses or positive events recorded from blank samples. All of the obtained concentrations were consistent with those found using conventional bacterial culture, but with a considerably lower standard deviation (Fig. 1.3.9C).

Antibodies are an excellent option for the accurate recognition of specific targets; however, they are expensive to produce, delicate to handle, and rather large in size (a factor that limits the formation of active hot spots). In the last years, a new family of biomolecules (aptamers) has been developed as an efficient alternative to antibodies. Aptamers display similar or even larger target specificities,[79,80] while providing key advantages in terms of stability, immunogenicity, facility of production, functionalization, and reduced size. To address this point, we recently extended the use of MODS for online SERS quantification of bacteria in different human fluids (urine, blood, or pleural and ascites fluids infected with very low concentration of *S. aureus*) using aptamer-functionalized SERS-encoded nanoparticles.[81] In this work, we extensively characterized the efficiency of different biofunctionalized

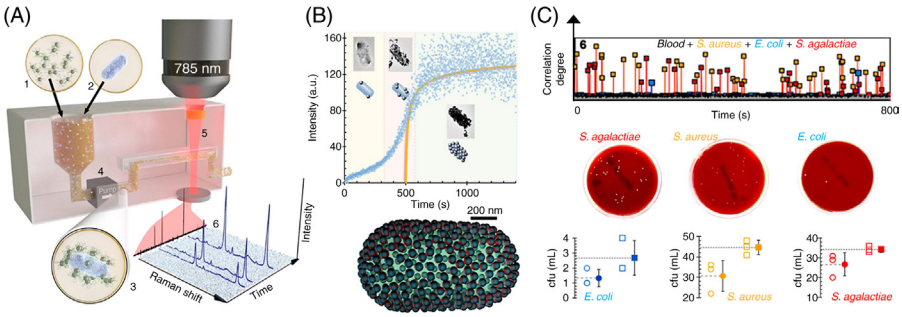

FIGURE 1.3.9

(A) Conceptual view of a microorganism optical detection system (MODS). Antibody-conjugated silver nanoparticles labeled with different Raman-active molecules (*1*) are mixed in a vessel with the sample fluid (*2*). The presence of one of the targeted bacteria promotes the accumulation of the corresponding antibody-matching nanoparticles on its membrane until full coverage is achieved (3). Then, the mixture is circulated through a millifluidic channel with a micropump (*4*) and investigated with a 785-nm laser (*5*) to record the SERS signal (*6*). (B) Kinetics of nanoparticle aggregation as measured through the time-dependent SERS signal *(symbols)* after adding *E. coli* to the mixture of coded nanoparticles. The *solid curve* corresponds to the simulation of the temporal evolution of silver nanoparticles aggregation on the bacteria membrane produced by random nanoparticle-membrane encounters. (C) MODS performance for contaminated blood samples and comparison with bacterial cultures. The blood sample was spiked with a combination of three different bacteria and concentrations (*S. aureus*, *E. coli*, and *S. agalactiae*). Top: Correlation was calculated between a temporal series of spectra collected over 270-ms intervals and the SERS reference of the labeled nanoparticles. Large correlation values reveal the passage of an individual bacteria or colony-forming unit. Middle: Bacterial cultures (24–48 h) for the microorganism inoculated in the blood samples (*white spots* correspond to colony-forming units). Bottom: Comparison of the bacteria concentrations (cfu/mL) as determined by MODS *(open squares)* for the sample contaminated with three pathogens versus traditional cultures *(open circles)*. Averages over three runs of both MODS and culture experiments are shown by the corresponding *solid symbols*.

Figure adapted with permission from Pazos-Perez N, Pazos E, Catala C, Mir-Simon B, Gómez-de Pedro S, Sagales J, et al. Ultrasensitive multiplex optical quantification of bacteria in large samples of biofluids. Sci Rep *2016;**6**:29014.*[78]

SERS-encoded particles, demonstrating the important advantages of using aptamers over antibodies as biorecognition elements. First, aptamers exhibit much larger affinity for bacteria than antibodies. Second, the final SERS intensity registered for aptamers (at nanoparticle saturation) is around 40% larger than that for antibodies. This can be explained by considering that antibody conjugation onto nanoparticle surfaces results in a random orientation, where a fraction of those attached antibodies experience an inactivation of their binding sites (i.e., paratope).[82] Conversely, aptamers can be easily functionalized/modified without any loss of their activity and, then,

their conjugation on the nanoparticle surface can be directed to yield a conformation suitable for their efficient interaction with the target entity. Furthermore, the smaller size of aptamers reduces the interparticle gaps at the bacterial surface, leading to an overall increase of the electromagnetic energy generated at the hot spot.

6 CONCLUSIONS

SERS probes and labels offer several advantages over other optical probes with respect to versatility, sensitivity, selectivity, and biocompatibility. Future challenges include the development of multifunctional SERS probes with optimized plasmonic nanostructures as basic building blocks. Plasmonic structures, as key components of SERS probes, can offer high local optical fields for sensitive diagnostic probing with SERS, with much lower acquisition times. This later parameter is of paramount importance due to the sample volumes commonly screened in actual medical practice. Utilizing the progress that has been made in the design of SERS-encoded particles, the application of SERS probes is about to revolutionize bioanalysis. The first proof-of-principle studies are promising and will pave the way for enabling multiplex identification and quantification of microorganisms directly on their biological matrix with unprecedented speed, low cost, and sensitivity.

REFERENCES

1. World Health Organization. Prevention of hospital-acquired infections. 2012. Available from: http://apps.who.int/medicinedocs/index/assoc/s16355e/s16355e.pdf.
2. World Health Organization. Health care-associated infections. Available from: http://www.who.int/gpsc/country_work/gpsc_ccisc_fact_sheet_en.pdf.
3. Brockmann D. Human mobility and spatial disease dynamics. Reviews of nonlinear dynamics and complexity. Weinheim: Wiley-VCH Verlag GmbH & Co. KGaA; 2010 [pp. 1–24].
4. Kumar A, Roberts D, Wood KE, Light B, Parrillo JE, Sharma S, et al. Duration of hypotension before initiation of effective antimicrobial therapy is the critical determinant of survival in human septic shock. *Crit Care Med* 2006;**34**(6):1589–96.
5. Dellinger RP, Levy MM, Rhodes A, Annane D, Gerlach H, Opal SM, et al. Surviving sepsis campaign: international guidelines for management of severe sepsis and septic shock: 2012. *Crit Care Med* 2013;**41**(2):580–637.
6. Efrima S, Zeiri L. Understanding SERS of bacteria. *J Raman Spectrosc* 2009;**40**(3):277–88.
7. Long DA. *Raman Spectroscopy*. Maidenhead: McGraw-Hill; 1977.
8. Comin A, Manna L. New materials for tunable plasmonic colloidal nanocrystals. *Chem Soc Rev* 2014;**43**(11):3957–75.
9. Murray WA, Barnes WL. Plasmonic materials. *Adv Mater* 2007;**19**(22):3771–82.
10. West PR, Ishii S, Naik GV, Emani NK, Shalaev VM, Boltasseva A. Searching for better plasmonic materials. *Laser Photon Rev* 2010;**4**(6):795–808.
11. Wang AX, Kong X. Review of recent progress of plasmonic materials and nano-structures for surface-enhanced Raman scattering. *Materials* 2015;**8**(6):3024–52.

12. Abalde-Cela S, Aldeanueva-Potel P, Mateo-Mateo C, Rodríguez-Lorenzo L, Alvarez-Puebla RA, Liz-Marzán LM. Surface-enhanced Raman scattering biomedical applications of plasmonic colloidal particles. *J Royal Soc Interf* 2010;**7**(Suppl. 4):S435–50.
13. Naik GV, Shalaev VM, Boltasseva A. Alternative plasmonic materials: beyond gold and silver. *Adv Mater* 2013;**25**(24):3264–94.
14. Le Ru EC, Etchegoin PG. *Principles of surface-enhanced Raman spectroscopy*. United Kingdom: Elsevier; 2009.
15. Zeng S, Baillargeat D, Ho HP, Yong KT. Nanomaterials enhanced surface plasmon resonance for biological and chemical sensing applications. *Chem Soc Rev* 2014;**43**(10):3426–52.
16. Zheng YB, Kiraly B, Weiss PS, Huang TJ. Molecular plasmonics for biology and nanomedicine. *Nanomedicine* 2012;**7**(5):751–70.
17. Pelaz B, Alexiou C, Alvarez-Puebla RA, Alves F, Andrews AM, Ashraf S, et al. Diverse applications of nanomedicine. *ACS Nano* 2017;**11**(3):2313–81.
18. Rycenga M, Cobley CM, Zeng J, Li W, Moran CH, Zhang Q, et al. Controlling the synthesis and assembly of silver nanostructures for plasmonic applications. *Chem Rev* 2011;**111**(6):3669–712.
19. Lu X, Rycenga M, Skrabalak SE, Wiley B, Xia Y. Chemical synthesis of novel plasmonic nanoparticles. *Annu Rev Phys Chem* 2009;**60**:167–92.
20. Iravani S, Korbekandi H, Mirmohammadi SV, Zolfaghari B. Synthesis of silver nanoparticles: chemical, physical and biological methods. *Res Pharm Sci* 2014;**9**(6):385–406.
21. Mittal AK, Chisti Y, Banerjee UC. Synthesis of metallic nanoparticles using plant extracts. *Biotechnol Adv* 2013;**31**(2):346–56.
22. Zhao P, Li N, Astruc D. State of the art in gold nanoparticle synthesis. *Coord Chem Rev* 2013;**257**(3–4):638–65.
23. Zhou W, Gao X, Liu D, Chen X. Gold nanoparticles for in vitro diagnostics. *Chem Rev* 2015;**115**(19):10575–636.
24. Grzelczak M, Perez-Juste J, Mulvaney P, Liz-Marzan LM. Shape control in gold nanoparticle synthesis. *Chem Soc Rev* 2008;**37**(9):1783–91.
25. Pazos-Perez N, Garcia de Abajo FJ, Fery A, Alvarez-Puebla RA. From nano to micro: synthesis and optical properties of homogeneous spheroidal gold particles and their superlattices. *Langmuir* 2012;**28**(24):8909–14.
26. Ye X, Zheng C, Chen J, Gao Y, Murray CB. Using binary surfactant mixtures to simultaneously improve the dimensional tunability and monodispersity in the seeded growth of gold nanorods. *Nano Lett* 2013;**13**(2):765–71.
27. Liebig F, Sarhan RM, Prietzel C, Reinecke A, Koetz J. "Green" gold nanotriangles: synthesis, purification by polyelectrolyte/micelle depletion flocculation and performance in surface-enhanced Raman scattering. *RSC Adv* 2016;**6**(40):33561–8.
28. Sun YG, Xia YN. Shape-controlled synthesis of gold and silver nanoparticles. *Science* 2002;**298**(5601):2176–9.
29. Braeckmans K, De Smedt SC, Leblans M, Roelant C, Demeester J. Encoding microcarriers: present and future technologies. *Nat Rev Drug Discov* 2002;**1**:1–10.
30. Golightly RS, Doering WE, Natan MJ. Surface-enhanced Raman spectroscopy and homeland security: a perfect match? *ACS Nano* 2009;**3**(10):2859–69.
31. Cao YC, Jin R, Mirkin CA. Nanoparticles with Raman spectroscopic fingerprints for DNA and RNA detection. *Science* 2002;**297**:1536–40.
32. Fernandez-Lopez C, Mateo-Mateo C, Alvarez-Puebla RA, Perez-Juste J, Pastoriza-Santos I, Liz-Marzan LM. Highly controlled silica coating of PEG-capped metal nanoparticles and preparation of SERS-Encoded particles. *Langmuir* 2009;**25**(24):13894–9.

33. Küstner B, Gellner M, Schütz M, Schöppler F, Marx A, Ströbel P, et al. SERS labels for red laser excitation: silica-encapsulated SAMs on Tunable gold/silver nanoshells. *Angew Chem Int Ed* 2009;**48**(11):1950–3.
34. Wang G, Park H-Y, Lipert RJ, Porter MD. Mixed monolayers on gold nanoparticle labels for multiplexed surface-enhanced Raman scattering based immunoassays. *Anal Chem* 2009;**81**(23):9643–50.
35. Guerrero-Martinez A, Perez-Juste J, Liz-Marzan LM. Recent progress on silica coating of nanoparticles and related nanomaterials. *Adv Mater* 2010;**22**(11):1182–95.
36. Brus L. Noble metal nanocrystals: plasmon electron transfer photochemistry and single-molecule Raman spectroscopy. *ACC Chem Res* 2008;**41**(12):1742–9.
37. Alvarez-Puebla R, Liz-Marzan LM, Javier Garcia de Abajo F. Light concentration at the nanometer scale. *J Phys Chem Lett* 2010;**1**(16):2428–34.
38. Nelayah J, Kociak M, Stéphan O, De Abajo FJG, Tencé M, Henrard L, et al. Mapping surface plasmons on a single metallic nanoparticle. *Nat Phys* 2007;**3**(5):348–53.
39. Rodriguez-Lorenzo L, Alvarez-Puebla RA, Pastoriza-Santos I, Mazzucco S, Stephan O, Kociak M, et al. Zeptomol detection through controlled ultrasensitive surface-enhanced Raman scattering. *J Am Chem Soc* 2009;**131**(13):4616–8.
40. Rodriguez-Lorenzo L, Krpetic Z, Barbosa S, Alvarez-Puebla RA, Liz-Marzan LM, Prior IA, et al. Intracellular mapping with SERS-encoded gold nanostars. *Integr Biol* 2011;**3**(9):922–6.
41. Yang M, Alvarez-Puebla R, Kim H-S, Aldeanueva-Potel P, Liz-Marzan LM, Kotov NA. SERS-active gold lace nanoshells with built-in hotspots. *Nano Lett* 2010;**10**(10):4013–9.
42. Fresnais J, Lavelle C, Berret JF. Nanoparticle aggregation controlled by desalting kinetics. *J Phys Chem C* 2009;**113**(37):16371–9.
43. Moskovits M, Vlčková B. Adsorbate-induced silver nanoparticle aggregation kinetics. *J Phys Chem B* 2005;**109**(31):14755–8.
44. Su X, Zhang J, Sun L, Koo T-W, Chan S, Sundararajan N, et al. Composite organic−inorganic nanoparticles (COINs) with Chemically encoded optical signatures. *Nano Lett* 2004;**5**(1):49–54.
45. Sun L, Sung K-B, Dentinger C, Lutz B, Nguyen L, Zhang J, et al. Composite organic−inorganic nanoparticles as Raman labels for tissue analysis. *Nano Lett* 2007;**7**(2):351–6.
46. Lutz BR, Dentinger CE, Nguyen LN, Sun L, Zhang J, Allen AN, et al. Spectral analysis of multiplex Raman probe signatures. *ACS Nano* 2008;**2**(11):2306–14.
47. Brown LO, Doorn SK. Optimization of the preparation of glass-coated, dye-tagged metal nanoparticles as SERS substrates. *Langmuir* 2008;**24**(5):2178–85.
48. Brown LO, Doorn SK. A controlled and reproducible pathway to dye-tagged, encapsulated silver nanoparticles as substrates for SERS multiplexing. *Langmuir* 2008;**24**(6):2277–80.
49. Goddard G, Brown LO, Habbersett R, Brady CI, Martin JC, Graves SW, et al. High-resolution spectral analysis of individual SERS-active nanoparticles in flow. *J Am Chem Soc* 2010;**132**(17):6081–90.
50. Stoerzinger KA, Hasan W, Lin JY, Robles A, Odom TW. Screening nanopyramid assemblies to optimize surface enhanced Raman scattering. *J Phys Chem Lett* 2010;**1**(7):1046–50.
51. Rycenga M, Camargo PHC, Li W, Moran CH, Xia Y. Understanding the SERS effects of single silver nanoparticles and their dimers, one at a time. *J Phys Chem Lett* 2010;**1**(4):696–703.
52. Jin R. Nanoparticle clusters light up in SERS. *Angew Chem Int Ed* 2010;**49**(16):2826–9.

53. Chen G, Wang Y, Yang M, Xu J, Goh SJ, Pan M, et al. Measuring ensemble-averaged surface-enhanced Raman scattering in the hotspots of colloidal nanoparticle dimers and trimers. *J Am Chem Soc* 2010;**132**(11):3644–5.
54. Pallaoro A, Braun GB, Reich NO, Moskovits M. Mapping local pH in live cells using encapsulated fluorescent SERS nanotags. *Small* 2010;**6**(5):618–22.
55. Moskovits M, Braun GB, Lee SJ, Laurence T, Fera N, Fabris L, et al. Generalized approach to SERS-active nanomaterials via controlled nanoparticle linking, polymer encapsulation, and small-molecule infusion. *J Phys Chem C* 2009;**113**(31):13622–9.
56. Li S, Pedano ML, Chang S-H, Mirkin CA, Schatz GC. Gap structure effects on surface-enhanced Raman scattering intensities for gold gapped rods. *Nano Lett* 2010;**10**(5):1722–7.
57. Mir-Simon B, Reche-Perez I, Guerrini L, Pazos-Perez N, Alvarez-Puebla RA. Universal one-pot and scalable synthesis of SERS encoded nanoparticles. *Chem Mater* 2015;**27**(3):950–8.
58. Pazos-Perez N, Wagner CS, Romo-Herrera JM, Liz-Marzan LM, de Abajo FJG, Wittemann A, et al. Organized plasmonic clusters with high coordination number and extraordinary enhancement in surface-enhanced Raman scattering (SERS). *Angew Chem Int Ed* 2012;**51**(51):12688–93.
59. Jarvis RM, Goodacre R. Characterisation and identification of bacteria using SERS. *Chem Soc Rev* 2008;**37**(5):931–6.
60. Jarvis RM, Goodacre R. Discrimination of bacteria using surface-enhanced Raman spectroscopy. *Anal Chem* 2004;**76**(1):40–7.
61. Guicheteau J, Argue L, Emge D, Hyre A, Jacobson M, Christesen S. *Bacillus* spore classification via surface-enhanced Raman spectroscopy and principal component analysis. *Appl Spectrosc* 2008;**62**(3):267–72.
62. Muhamadali H, Subaihi A, Mohammadtaheri M, Xu Y, Ellis DI, Ramanathan R, et al. Rapid, accurate, and comparative differentiation of clinically and industrially relevant microorganisms: via multiple vibrational spectroscopic fingerprinting. *Analyst* 2016;**141**(17):5127–36.
63. Zhang L, Xu J, Mi L, Gong H, Jiang S, Yu Q. Multifunctional magnetic-plasmonic nanoparticles for fast concentration and sensitive detection of bacteria using SERS. *Biosens Bioelectron* 2012;**31**(1):130–6.
64. Szymborski T, Witkowska E, Adamkiewicz W, Waluk J, Kaminska A. Electrospun polymer mat as a SERS platform for the immobilization and detection of bacteria from fluids. *Analyst* 2014;**139**(20):5061–4.
65. Liu TY, Tsai KT, Wang HH, Chen Y, Chen YH, Chao YC, et al. Functionalized arrays of Raman-enhancing nanoparticles for capture and culture-free analysis of bacteria in human blood. *Nat Commun* 2011;**2**(1):538.
66. Walter A, Marz A, Schumacher W, Rosch P, Popp J. Towards a fast, high specific and reliable discrimination of bacteria on strain level by means of SERS in a microfluidic device. *Lab on a Chip* 2011;**11**(6):1013–21.
67. Cheng I-F, Lin C-C, Lin D-Y, Chang H-C. A dielectrophoretic chip with a roughened metal surface for on-chip surface-enhanced Raman scattering analysis of bacteria. *Biomicrofluidics* 2010;**4**(3):034104.
68. Sackmann EK, Fulton AL, Beebe DJ. The present and future role of microfluidics in biomedical research. *Nature* 2014;**507**(7491):181–9.
69. Fenniri H, Alvarez-Puebla R. High-throughput screening flows along. *Nat Chem Biol* 2007;**3**(5):247–9.

70. Abalde-Cela S, Abell C, Alvarez-Puebla RA, Liz-Marzán LM. Real time dual-channel multiplex SERS ultradetection. *J Phys Chem Lett* 2014;**5**(1):73–9.
71. Muhlig A, Bocklitz T, Labugger I, Dees S, Henk S, Richter E, et al. LOC-SERS: a promising closed system for the identification of mycobacteria. *Anal Chem* 2016;**88**(16):7998–8004.
72. Cheng IF, Chang H-C, Chen T-Y, Hu C, Yang F-L. Rapid (<5 min) identification of pathogen in human blood by electrokinetic concentration and surface-enhanced Raman spectroscopy. *Sci Rep* 2013;**3**:2365.
73. Madiyar FR, Bhana S, Swisher LZ, Culbertson CT, Huang XH, Li J. Integration of a nanostructured dielectrophoretic device and a surface-enhanced Raman probe for highly sensitive rapid bacteria detection. *Nanoscale* 2015;**7**(8):3726–36.
74. Lin HY, Huang CH, Hsieh WH, Liu LH, Lin YC, Chu CC, et al. On-line SERS detection of single bacterium using novel SERS nanoprobes and a microfluidic dielectrophoresis device. *Small* 2014;**10**(22):4700–10.
75. Wang C, Madiyar F, Yu C, Li J. Detection of extremely low concentration waterborne pathogen using a multiplexing self-referencing SERS microfluidic biosensor. *J Biol Eng* 2017;**11**(1):9.
76. Pethig R. Review article—dielectrophoresis: status of the theory, technology, and applications. *Biomicrofluidics* 2010;**4**(2):022811.
77. Cockerill IFR, Wilson JW, Vetter EA, Goodman KM, Torgerson CA, Harmsen WS, et al. Optimal testing parameters for blood cultures. *Clin Infect Dis* 2004;**38**(12):1724–30.
78. Pazos-Perez N, Pazos E, Catala C, Mir-Simon B, Gómez-de Pedro S, Sagales J, et al. Ultrasensitive multiplex optical quantification of bacteria in large samples of biofluids. *Sci Rep* 2016;**6**:29014.
79. Bunka DHJ, Stockley PG. Aptamers come of age—at last. *Nature Rev Microbiol* 2006;**4**(8):588–96.
80. Keefe AD, Pai S, Ellington A. Aptamers as therapeutics. *Nat Rev Drug Discov* 2010;**9**(7):537–50.
81. Catala C, Mir-Simon B, Feng X, Cardozo C, Pazos-Perez N, Pazos E, et al. Online SERS quantification of *Staphylococcus aureus* and the application to diagnostics in human fluids. *Adv Mater Technol* 2016;**1**(8):1600163.
82. Gordon MR, Canakci M, Li L, Zhuang J, Osborne B, Thayumanavan S. Field guide to challenges and opportunities in antibody–drug conjugates for chemists. *Bioconjugate Chem* 2015;**26**(11):2198–215.

SUBCHAPTER

Radiolabeled functional nanoparticles in preventive and regenerative medicine

1.4

Sanja Vranješ-Đurić*, Nenad L. Ignjatović**

**Vinča Institute of Nuclear Sciences, University of Belgrade, Belgrade, Serbia;*

***Institute of Technical Sciences of the Serbian Academy of Science and Arts, Belgrade, Serbia*

1 INTRODUCTION

Nuclear medicine is a branch of medicine that uses radiation to provide information about the functioning of a person's specific tissue/organs or to treat a disease. Radiolabeled nanoparticles (NPs) represent a new class of agents with a great potential for nuclear medicine applications. The key advantage of using radiolabeled NPs is that a very small amount can be used to obtain information of great importance.[1] They may be used to detect and characterize disease, to deliver relevant therapeutics, and to monitor the therapeutic effect as well. Furthermore radiotracer-based imaging either using single-photon emission computed tomography (SPECT) or positron emission tomography (PET) is particularly suited in the study of pharmacokinetic/pharmacodynamic parameters of nanomaterials and determination of their optimal nanodimensional architecture for tissue/organ regeneration. Measuring radiation from radioactive tracers attached to NPs has been demonstrated to be a highly sensitive and specific method that allows accurate quantification, without limits to tissue penetration in any organ. Nuclear imaging approaches are highly suitable for detection, as they offer a high detection sensitivity at high temporal and spatial resolutions, requiring a radionuclide concentration of around 10^{-10} M at the site of interest.

Nanoparticulate agents typically demonstrate pharmacokinetic behavior different from that of small molecules[2] and provide flexible platforms for integration of multiple functional entities, including targeting ligands, multiple types of contrast materials, and/or therapeutics. In contrast to traditional compounds used for radiopharmaceutical preparation, nanomaterials have an immense available surface area per unit of volume and tunable optical, electronic, magnetic, and biological properties. Generally, they can be tailored to meet the needs of specific applications and engineered to have different physicochemical properties that affect in vivo biodistribution: sizes, shapes, chemical compositions, surface chemical characteristics, and hollow or solid structures.[3] Efficient diagnosis/radiotherapy is provided through passive targeting based on the enhanced permeability and retention (EPR) effect (Fig. 1.4.1) and/or active targeting through the incorporation of a targeting moiety on an NP. Nontargeted NPs can accumulate in tumors, as the tumor vasculature

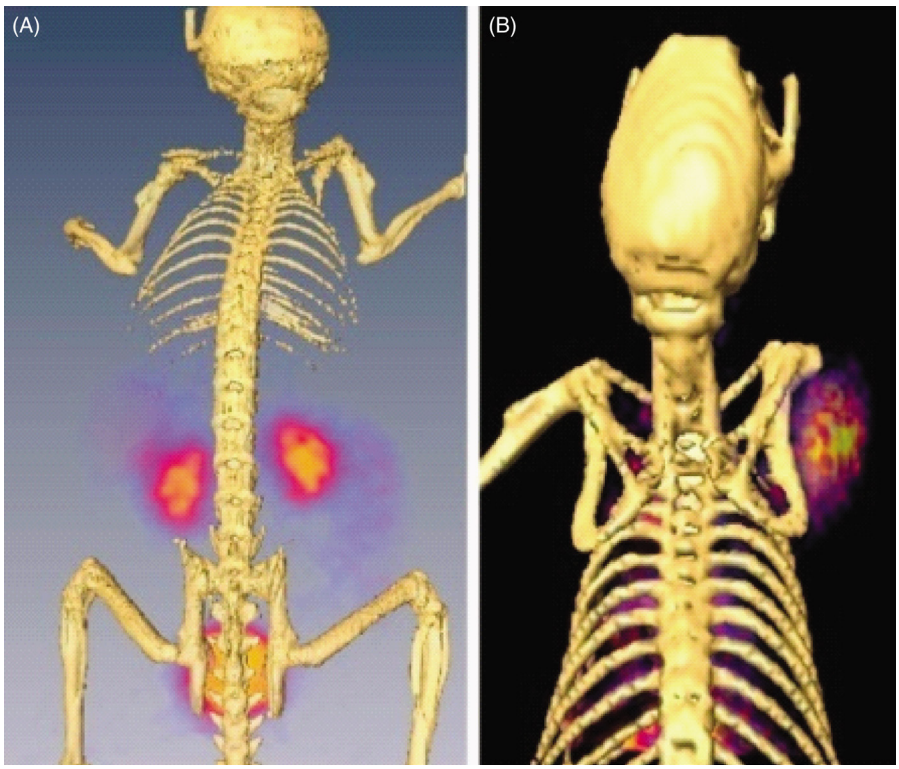

FIGURE 1.4.1 Passive Targeting.

Reconstructed positron emission tomography (PET)/computed tomography (CT) imaging in BALB/c mice with ^{68}Ga-(1,4,7,10-tetraazacyclododecane-1,4,7,10-tetraacetic acid)-polyamidoamine dendrimer (^{68}Ga-DOTA-PAMAM) acquired 1 h postadministration. (A) The kidneys and urinary bladder in normal mice and (B) tumor uptake localized in the tumor-bearing mouse.

Reproduced from Ghai A, Singh B, Hazari PP, Schultz MK, Parmar A, Kumar P, et al. Radiolabeling optimization and characterization of ^{68}Ga labeled DOTA–polyamido-amine dendrimer conjugate–Animal biodistribution and PET imaging results. Appl Radiat Isot *2015;**105**:40–6.*[4]

is usually leaky and without lymphatic drainage. Active targeting is achieved by functionalizing the NPs surface with suitable vectors, including peptides, antibodies, and other biomolecules, which recognize characteristic epitopes at the surface of the diseased cells.

Radiolabeled antibodies may effectively target even single cancer cells in circulation[5] or small cancer cell clusters,[6] thereby enabling a more specific radiation dose delivery, preventing damage to healthy tissues.

2 RADIOLABELING OF NANOPARTICLES: SELECTION OF RADIONUCLIDES AND OPTIMIZATION OF THE RADIOLABELING PROCEDURE

Several key issues need to be addressed for the selection and application of radionuclides for the radiolabeling of NPs. In contrast to NP production, the radiolabeling process is time limited and difficult because of the contamination risk. The handling of radionuclides has to be carried out in specially designed radiochemical laboratories with controlled ventilation and air conditioning, shielded remote handling facilities, and special equipment intended for measuring the radioactivity of the selected radionuclide. There are two main methods for the fabrication of radionuclides: using a nuclear reactor or using a particle accelerator. These methods are complementary in providing a wide variety of radionuclides for application in medicine and research (Fig. 1.4.2).

The ability to access radionuclides without the use of on-site accelerators or reactors depends on the availability of generator-produced radionuclides in which the parent radionuclide is produced from a reactor or cyclotron. A generator is a

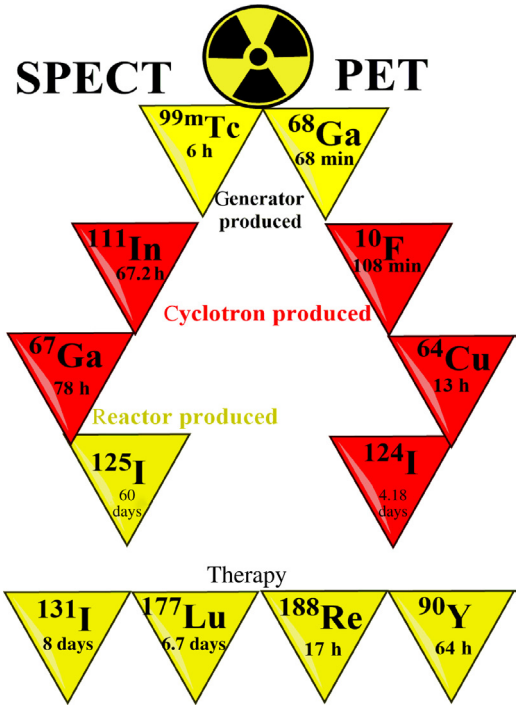

FIGURE 1.4.2 Radionuclides for the Radiolabeling of Nanoparticles (NPs).

SPECT, Single-photon emission computed tomography.

device that is used to extract one radionuclide from another. The molybdenum-99 (^{99}Mo)/technetium-99m (^{99m}Tc) generator is especially popular and very convenient. The differences in the half-lives and chemical properties of ^{99}Mo (half-life: 66 h) and ^{99m}Tc (half-life: 6 h) are exploited to separate them in the generator. This procedure can be repeated many times providing a nearly continuous supply of radionuclides at a low cost. Germanium-68/gallium-68, strontium-82/rubidium-82, and tungsten-188/rhenium-188 are newly developed generators.

The selection criteria for radionuclides must be based on the physical data about the radionuclide and biological variables governing their use. The considerations for physical characteristics include the physical half-life, type of emissions, energy of the radiation(s), daughter product(s), method of production, and radionuclide purity. The biochemical aspects include tissue targeting, the retention of radioactivity in the organ/tissue, in vivo stability, and toxicity.

Diagnostic radionuclides are generally short-lived radionuclides capable of providing the necessary information on biodistribution, dosimetry, and the limiting or the critical organ or the tissue. Radionuclides for SPECT imaging decay by the emission of high-energy photons (γ), while PET radionuclides decay by emission of positrons (β^+). The selection of appropriate therapeutic radionuclides that emit α- or β- particles depends upon the nature, the extent, and stage of disease. These types of particulate radiations allow very high ionization per length of travel. Therefore, they are fully deposited within a small range of tissue (usually in millimeter). The longer range of beta particles can still permit uniform tumor irradiation despite of a possible heterogeneity in distribution of radioactivity within the tumor. Therapeutic radionuclides that also decay with γ-radiation can be advantageous if the energy and intensity are within the diagnostic range, as distribution of the radiolabeled NPs can be visualized.[7]

The physical half-life of radionuclide plays a crucial role for measurements in the desired time frame, and which radionuclide or half-life is suitable for the investigated question and pharmacokinetic profile has to be considered. For measurements within a short (initial) time frame after intravenous administration, short-lived PET radionuclides have been applied, for example, fluorine-18 (half-life 109.7 min), gallium-68 (half-life 67.7 min), or even nitrogen-13 (half-life 9.97 min).[8] Conversely, if the half-life is too short, most decay will occur before the radiolabeled NPs targeting has reached the maximum tissue accumulation.

The major requirements of the radiolabeling procedure are that the labeling process does not significantly alter the structure or properties of the NPs and that the stability of radiolabeled product is sufficient to allow further in vivo tracking. Once the radiolabeling method for the selected radionuclide and NPs type is optimized, the radioactive part may be used not only to track NPs, but also for radiodiagnosis or radiotherapy.

Depending on the radionuclide and the composition and structure of NPs, two approaches may be applied for efficient radiolabeling (Fig. 1.4.3): direct radiolabeling (mostly via nucleophilic/electrophilic labeling and coordination chemistry) or indirect radiolabeling (via a chelator or a complexing agent, which requires additional synthetic steps). Furthermore, radionuclides can be attached to whole particles

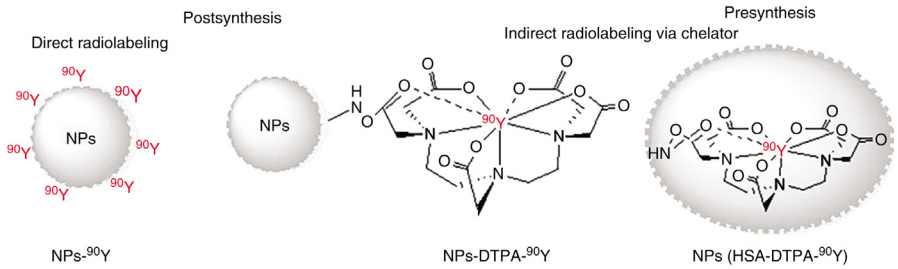

FIGURE 1.4.3 Radiolabeling of NPs.

DTPA, Diethylenetriaminepentaacetic acid; *HSA*, human serum albumin.

synthesized in advance (postsynthesis approach), or they can be entrapped in NPs during the synthesis (presynthesis approach).

The convenience, efficiency, and gentleness of radiolabeling procedures are some of the requirements that have to be met by radiolabeling methods. The binding of radionuclides to an NP has to be irreversible to prevent their escape to other tissues or organs. Careful in vitro experiments for measuring the stability of radiolabeled NPs (mostly in serum) are generally required prior to in vivo studies. The biodistribution patterns of radiolabeled NPs do not seem to be crucially affected by the radiolabeling approach. In general, radiolabeled NPs are excreted into the urinary tract via the kidneys and they mostly accumulate in the reticuloendothelial tissues, liver, and spleen, due to the substantial uptake by the macrophages that are present in these organs. If they agglomerate and the size is relatively large, in range of micrometers, the highest uptake after intravenous administration occurs in the lungs.[9]

2.1 RADIOLABELING WITH γ-EMITTING RADIONUCLIDES

Technetium-99m (^{99m}Tc), indium-111 (^{111}In), gallium-67 (^{67}Ga), and iodine-125 (^{125}I) are the most commonly used γ-emitting radionuclides for NP radiolabeling. These radionuclides emit single photons detected by a gamma camera that can view organs from different angles.

2.1.1 Radiolabeling with ^{99m}Tc

Radiolabeling with ^{99m}Tc (half-life 6 h) accounts for about 80% of all nuclear medicine procedures worldwide. This can be attributed to its ideal physical properties, such as its half-life, that allow for prolonged in vivo imaging and γ-photon single-energy emission at 140 keV, which is beneficial for effective imaging. The chemical form of ^{99m}Tc occurs as ^{99m}Tc-pertechnetate $\left(^{99m}TcO_4^-\right)$. In a chemical reaction, it is necessary to reduce its oxidation state to a lower value. Stannous chloride ($SnCl_2$) is the most often used reducing agent. The direct method of ^{99m}Tc labeling of NPs is based on the fact that the reduced $^{99m}TcO_4$ reacts with random groups, such as hydroxyl, carboxylic, and amino groups, present on the surface of the NPs. A direct labeling method was used to label hydroxyapatite nanoparticles (HApNP),[10] as well

as astaxanthin-loaded solid lipid NPs. The direct nose-to-brain delivery of the ^{99m}Tc-labeled lipid NPs was evident by γ-scintigraphy imaging, suggesting their potential use for various neurological diseases.[11] Tassano et al. developed another direct labeling procedure via a tricarbonyl precursor $\left[^{99m}\mathrm{Tc}(\mathrm{H_2O})(\mathrm{CO_3})\right]^{+}$ for radiolabeling dendrimers.[12] This method has been proven to be effective for labeling various ligands, such as ethylendiamine-*N*,*N*′-diacetate, which have significant tumor uptake exclusively by passive targeting.[13] NPs loaded with these compounds have a higher probability for tumor uptake.

Radiometals, both diagnostic (^{64}Cu, ^{68}Ga, and ^{89}Zr) and therapeutic (^{90}Y and ^{177}Lu), are best attached to NPs via chelation. The indirect chelator-mediated ^{99m}Tc-labeling of NPs has been applied to a variety of NP structures.[14] Helbok et al. performed efficient radiolabeling of PEGylated cholesterol liposomes and micelles via an acyclic diethylenetriaminepentaacetic acid (DTPA) chelator.[15] Also, poly(ethylene) glycol (PEG) liposomes can be labeled relatively easily and stably with ^{99m}Tc after liposome synthesis, using a procedure which includes the conjugation of ^{99m}Tc to hexamethyl propyleneamine (HMPAO)[16] or hydrazino nicotinamide (HYNIC)[17] followed by their encapsulation into liposomes. The HYNIC-based method provides ^{99m}Tc-labeled liposomes with a high labeling yield (>95%) and improved in vitro and in vivo characteristics compared to the liposomes labeled via ^{99m}Tc-HMPAO. Chitosan (Ch) hydrogel NPs loaded with a vascular endothelial growth factor (a potent angiogenic factor) were efficiently labeled with ^{99m}Tc via a DTPA chelator. The quantitative imaging with ^{99m}Tc-Ch NPs has been demonstrated to be a valuable strategy that can be combined with an angiogenic therapy to customize the treatment of myocardial ischemia.[18] Mercapto acetyl triglycine (MAG3) has been applied to facilitate radiolabeling of morpholinos.[19] *meso*-2,3-Dimercaptosuccinic acid (DMSA) is also a suitable ligand that forms complex compounds with ^{99m}Tc, $^{186/188}$Re, ^{166}Ho, ^{177}Lu, and ^{90}Y. DMSA enables bidentate binding via two sulfur atoms on silver nanoclusters (Fig. 1.4.4) and additional radiolabeling is possible via the binding of radiometals to DMSA.[20]

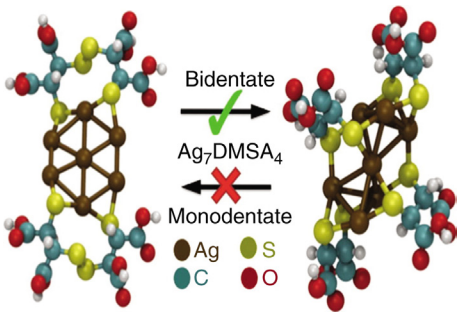

FIGURE 1.4.4 Bidentate-Binding of *meso*-2,3-Dimercaptosuccinic Acid (DMSA) on Silver Nanoclusters.

Reproduced from Zaluzhna O, Brightful L, Allison TC, Tong YJ. Spectroscopic evidence of a bidentate-binding of meso*-2,3-dimercaptosuccinic acid on silver nanoclusters.* Chem Phys Lett *2011;**509**(4):148–51.*[20]

In some chelating systems it is possible to apply a theranostic approach by substituting the diagnostic radionuclide with a therapeutic one, whereas the chelator and the nanodimensional structure remain. Due to the similar chemical properties of ^{99m}Tc for ^{188}Re, the labeling procedure is based on the similar complexation chemistries of two radionuclides with the same vector.

Further studies on indirect NP ^{99m}Tc-labeling may include the investigation of novel ligands, such as diamino dioxime ligands that form a neutral and lipophilic complex with ^{99m}Tc. The specified ligand and those that are chemically similar to it pass easily through the intact blood–brain barrier. Accordingly, they have a high potential in cerebral perfusion imaging.[21] Iron oxide nanoparticles (IONPs) may be labeled with a variety of diagnostic and therapeutic radionuclides via direct and indirect, chelator-based radiolabeling techniques. The ^{99m}Tc-labeled aminosilane-coated IONPs may be promising candidates for guided cancer diagnosis and magnetic hyperthermia therapy. Targeting is enabled via the conjugation with a new peptide-based Arg-Gly-Asp (RGD) derivate, which has a high affinity and selectivity for the $\alpha v\beta 3$ integrin receptor presented in several tumors. The specific character of ^{99m}Tc-NPs-RGD was confirmed in a receptor blocking study, in which the coadministration of an excess amount of the native peptide blocked an experimentally induced U87MG tumor (with an overexpression of the $\alpha v\beta 3$ receptors). This resulted in a significantly reduced uptake of ^{99m}Tc-NPs-RGD, indicating the specific character of the targeted IONPs (Fig. 1.4.5).[22]

2.1.2 Radiolabeling with ^{111}In

Indium-111 (^{111}In), is a readily available γ-emitting radiometal, which is widely used in clinical practice for diagnosis.[23] Several methods for the radiolabeling of NPs are described in the literature involve their conjugation with a chelate. The coupling of ^{111}In to NPs can be achieved by chelating molecules, such as DTPA or 1,4,7,10-tetraazacyclododecane-1,4,7,10-tetraacetic acid (DOTA), which are conjugated to the polymers as in the case of ^{111}In-DTPA-PEG-*b*-PCL micelles. PEG is an artificial but biocompatible hydrophilic polymer that has been widely applied for NP coating. The radiotracer method has been used to prove that it is possible to use PEG derivatives as tumor-imaging carriers. After ^{111}In labeling via DTPA, in vivo biodistribution studies demonstrated an increased tumor uptake and a prolonged circulation half-life with the increase in the molecular weight of PEG.[24] NPs that degrade and radionuclides that detach or are released from the NPs can cause artifacts. Dual radiolabeling using γ-emitters with different energy spectra incorporated into the core and coating may be used as a general methodology for a wide range of engineered NPs for the visualization of the degradation process of NPs in vivo. To label the core, ^{111}In-doped IONPs were encapsulated inside poly(lactide-*co*-glycolide) nanoparticles (PLGA NPs) during the preparation. The bovine serum albumin (BSA) coating was labeled by electrophilic substitution using ^{125}I. Imaging revealed different fates for the core and coating, with a fraction of the two radionuclides colocalizing in the liver and lungs for long periods of time after administration, suggesting that NPs are stable in these organs.[25] The conjugation of chelating agents to NPs

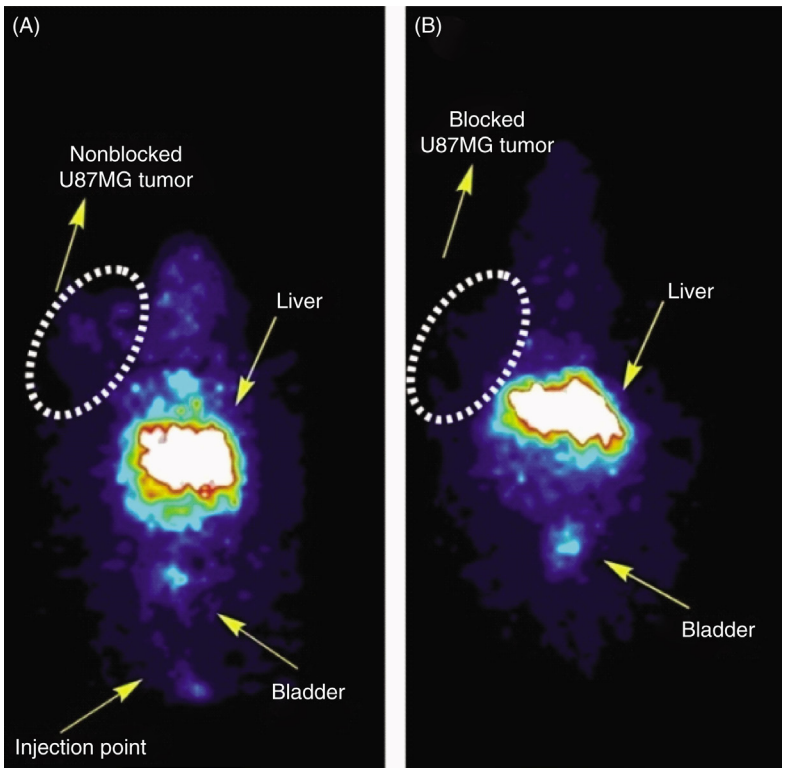

FIGURE 1.4.5 Active Targeting.

Representative planar γ images of ^{99m}Tc-NPs-[Arg-Gly-Asp (RGD)] [(A) nonblocked and (B) blocked] of a U87MG tumor–bearing mouse at 1 h post-injection.

Reproduced from Tsiapa I, Efthimiadou EK, Fragogeorgi E, Loudos G, Varvarigou AD, Bouziotis P, et al. ^{99m}Tc-labeled aminosilane-coated iron oxide nanoparticles for molecular imaging of αvβ3-mediated tumor expression and feasibility for hyperthermia treatment. J Colloid Interf Sci *2014;**433**:163–75.*[22]

could affect their biodistribution. The attachment of such a chelate could alter the corona of the micelles and, consequently, their biodistribution and pharmacokinetics. Similarly to other radionuclides, ^{111}In may also be entrapped in the micellar core during the formation of micelles without the need for any chemical modification.[26]

Polymeric micelles (lactosome) were labeled via DOTA with ^{111}In and ^{90}Y for SPECT imaging and radiotherapy, respectively. Biodistribution studies revealed that ^{111}In-DOTA-lactosome was selectively accumulated in the tumor site of mice due to the EPR effect. The observed antitumor therapeutic effect of ^{90}Y-DOTA-lactosome depended on the dose frequency and amount.[27]

2.1.3 Radiolabeling with ^{67}Ga

Gallium-67 (^{67}Ga) is a cyclotron-produced radiometal used for the imaging and localization of inflammatory lesions (infections). To get a better insight into

the transport mechanism of peptide-conjugated NPs to tumors, bombesin peptide–functionalized gold nanoparticles (AuNPs) were indirectly labeled with ^{67}Ga, and in vivo biological studies of ^{67}Ga-labeled AuNPs in human prostate tumor–bearing mice were performed. In the case of ^{67}Ga, the DTPA derivatives are unable to provide a stable coordination of ^{67}Ga with AuNPs. Therefore, ^{67}Ga labeling was pursued via DOTA-containing AuNPs. For intravenous administration, the receptor-mediated pathway appears to be outweighed by the EPR effect, while for the intraperitoneal administration, it has been concluded that the gastrin-releasing peptide receptor–mediated mechanism plays a role in pancreatic uptake.[28]

2.1.4 Radiolabeling with radioisotopes of iodine

Isotopes of iodine have been extensively used in clinical nuclear medicine imaging and radiation therapy. Out of the 37 known isotopes of iodine, 4—^{123}I, ^{124}I, ^{125}I, and ^{131}I—are suitable for SPECT or PET imaging. With a 60-day half-life, γ-emitter ^{125}I is useful for the long-term tracking and imaging of radiolabeled NPs. ^{131}I (half-life 8 days) is a strong γ-emitter, but due to its mode of β-decay, it is used for β-therapy, commonly in treating thyroid cancer. Dual-purpose theranostic radionuclides, for example, ^{131}I, or the pair ^{124}I/^{131}I can be used for imaging followed by therapy using the same radiolabeling procedure.

The traditional radiolabeling method with iodine radioisotopes is nucleophilic halogen exchange based on chloramine T oxidation (referred to as the iodogen method) by direct radioiodination or by using prosthetic groups, such as tyrosine residues of proteins.[29] Tang et al. synthesized a SPECT/magnetic resonance imaging (MRI)/optical trimodality probe by labeling fluorescent silica-coated IONPs with ^{125}I using the iodogen oxidation method. A radioactive probe was used to label mesenchymal stem cells and quantitatively track their migration and biodistribution in ischemic rats.[30]

The radiotracer technique has been demonstrated to be a relevant approach to the study the biodistribution of fullerenes (C_{60}). Although water-soluble C_{60} derivatives [polyhydroxylated fullerene $C_{60}(OH)_n$] were successfully radiolabeled with different radiotracers, including ^{67}Ga, ^{99m}Tc, ^{125}I, or ^{14}C, similar studies have not been performed with nano-C_{60}. The study of Nikolić et al.[31] described for the first time the efficient ^{125}I labeling of the solvent exchange–produced C_{60} NPs based on the intercalation of ^{125}I into fullerene crystals during the colloid preparation. Fullerene molecular crystals are filled with tetrahydrofuran (THF) molecules, but Na^{125}I ion pairs are also entrapped, much more in the case when Na^{125}I was added during than after the C_{60} dissolution (Fig. 1.4.6).

The labeling of particles after the preparation usually requires some chemical modification. HApNPs were modified with aminopropyltriethoxysilane to introduce amino groups on the surface of HAp for effective radioiodination.[32] Labeling without any modification achieved by adding the oxidizing agent chloramine T in situ during the formation of HAp resulted in the reproducible high labeling yield of ^{125}I-labeled HAp.[33]

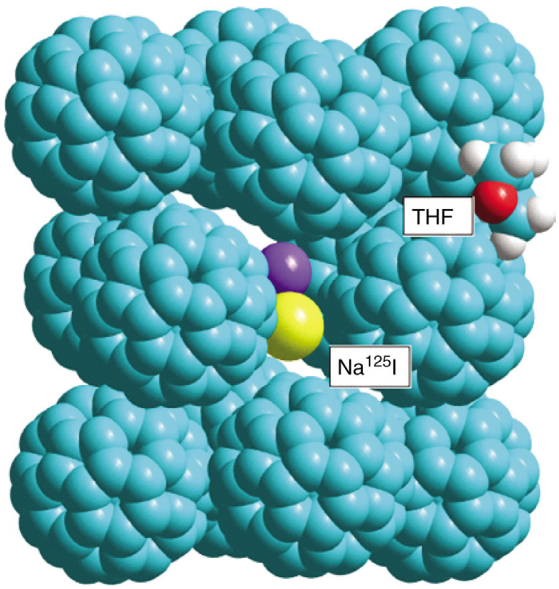

FIGURE 1.4.6 The Proposed Structure of Radiolabeled C_{60} Containing $Na^{125}I$ Ion Pair Intercalated in its Crystalline Lattice.

THF, tetrahydrofuran.

Reproduced from Nikolić N, Vranješ-Đurić S, Janković D, Đokić D, Mirković M, Bibić N, et al. Preparation and biodistribution of radiolabeled fullerene C60 nanocrystals. Nanotechnology *2009;**20**(38):385102.*[31]

2.2 RADIOLABELING WITH PET RADIONUCLIDES

Fluorine-18 (^{18}F, half-life 109.8 min), copper-64 (^{64}Cu half-life 12.7h), iodine-124 (^{124}I), gallium-68 (^{68}Ga, half-life 68 min), and zirconium-89 (^{89}Zr, half-life 78.4 h) are positron-emitting radionuclides mostly used for PET functional imaging. Compared to SPECT imaging, PET imaging may offer increased accuracy, higher sensitivity, and better resolution.[34] PET is a more recent development in medicine, and it uses radionuclides produced in a cyclotron. A cyclotron is a type of particle accelerator in which charged particles accelerate outward from the center along a spiral path. Limitations to the widespread use of PET arise from the high costs of cyclotrons needed to produce the short-lived radionuclides for PET scanning, the need for a specially adapted on-site chemical synthesis apparatus for radiolabeling, and a PET imaging facility in close proximity to the cyclotron due to the short half-life of most positron-emitting radionuclides. Furthermore, liposomes and some other NPs are the products of multiple steps that require a much longer process related to the half-lives of commonly used positron emitter nuclei. Thus, labeling methods in which components of liposome or preformulated drugs are substituted with short-lived positron-emitting radionuclides are impractical.

Urakami et al.[35] developed a rapid and efficient labeling method for lipid NPs via 1-[^{18}F]fluoro-3,6-dioxatetracosane without changing their physiological properties. Dynamic PET scanning showed that liposome-encapsulated hemoglobin delivers oxygen even into the ischemic region from the periphery toward the core of ischemia.

In recent years, the use of PET isotopes with a relatively long half-life (^{64}Cu, ^{89}Zr and ^{68}Ga) has been increased. These metals can be coupled in a straightforward fashion using chelators, such as DTPA, DOTA, 1,4,7-triazacyclononane-1,4,7-triacetic acid (NOTA), 1,4,8,11-tetraazacyclotetradecane-*N*,*N*′,*N*″,*N*‴-tetraacetic acid (TETA), and derivatives of these macrocyclic chelating agents. Originally, DOTA was designed for lanthanides (e.g., Gd^{3+}), but it can be used for a wide range of radiometals as well. As DOTA has four carboxylic functions on the side chains of the macrocycle-bearing four nitrogens, the binding of ^{64}Cu leads to deformed octahedral complexation of the Cu^{2+} ion, thereby leaving two of the acidic functions free. Accordingly, one is available for the coupling to NPs or polymers and the other allows further derivatization, or acts as an additional hydrophilic group. The review of Stockhofe et al.[8] presents a comprehensive study on various approaches and methods for the labeling of potential drug delivery systems using positron emitters.

^{64}Cu has favorable decay characteristics, (β^+: 0.653 MeV, 17.4%; β^-: 0.578 MeV, 39%) for both PET and radiotherapy. Due to a half-life of 12.7 h, it has been shown to be very effective for assessing the behavior of nanomaterials in vivo for prolonged times. The functionalization of PMMA-core/PEG-shell NPs with a DOTA ligand allowed for the chelation of ^{64}Cu and enabled the investigation of the biodistribution of these materials in correlation to the molecular weight of the backbone and the PEG grafts.[36] The method for ^{64}Cu labeling via NOTA as the chelator was developed in the case of cRGD-functionalized and doxorubicin-conjugated IONPs for potential application in drug delivery and PET/MRI dual-modality imaging.[37] Also, the application of an improved ^{64}Cu-labeling procedure via a novel amine-activated chelator [2-*p*-(3-aminopropylthioureido)benzyl-1,4,7,10-tetraazacyclododecane-tetraacetic acid (amine-Bz-DOTA)] conjugated to the surface of dextran sulfate–coated IONPs, enabled to avoid cross-linking of IONPs (which caused NP aggregation) and obtain a higher labeling yield.[38] Additional binding of tumor-specific antibodies to ^{64}Cu-labeled doxorubicin–loaded silica-based NPs provided an increased accumulation at the tumor site via an enhanced permeability, the retention effect, and antibody-mediated binding to tumor.[8]

The use of ^{68}Ga (positron emission intensity 87%) is on the rise due to several identifiable properties of this radionuclide. These include a superior image quality to that provided by SPECT radionuclides and the potential for on-demand production via a generator (^{68}Ge/^{68}Ga-generator).[39] Successful ^{68}Ga labeling requires a chelating agent and so far, DOTA and NOTA chelators have been used to radiolabel organic and inorganic nanodimensional systems with ^{68}Ga cation. Polyamidoamine dendrimer (PAMAM) was conjugated successfully with bifunctional chelate *N*-hydroxysuccinimide ester of DOTA, and the subsequent radiolabeling with ^{68}Ga was achieved with a high radiolabeling yield and stability. However, DOTA-like macrocycles are not the best ligands for Ga^{3+}, as the incorporation of ions inside the macrocyclic cavity leads to severe distortion of the coordination octahedra around the Ga^{3+} ions. NOTA-like ligands with a bis(phosphonate)-containing side arm (as the bone-targeting group) connected to a metal-binding cage through acetamide or methylphosphonate pendant arms ($NOTAM^{BP}$ and $NO2AP^{BP}$) have been shown as highly potent chelators for small $^{68}Ga^{3+}$ ions.[40] Synthetic apatite nanocrystals have

demonstrated an excellent ability to bind two PET radionuclides, ^{18}F and ^{68}Ga, with a good in vitro stability. Na^{18}F was used for the direct incorporation of the radionuclide into the crystal lattice, while the labeling by surface functionalization was accomplished by using ^{68}GaNO2AP^{BP}.

2.3 RADIOLABELING WITH THERAPEUTIC β-EMITTING RADIONUCLIDES

Currently, radionuclide therapy remains an important treatment option. The ionizing radiation from radionuclides can kill cells or inhibit the growth in the periphery and the inaccessible centers of cancerous lesions. The sites of damage comprise all cellular levels, especially DNA in the nucleus of cells.[41] Internal radiotherapy relies on the implantation of radioactive seeds, such as radiolabeled microparticles and NPs, delivering highly localized doses to a diseased area. Due to the inhomogeneous distribution of radiolabeled particles, especially within large tumors with a necrotic center, long-range β-emitters with lower linear energy transfers and greater annihilation distances of several cells (typically 0.2–12 mm) provide a larger and tortuous radioactive dose volume. Yttrium-90 (^{90}Y), lutetium-177 (^{177}Lu), and rhenium-188 (^{188}Re) are proposed as suitable candidates for the internal radionuclide therapy, especially of primary and metastatic malignancies, while α- and Auger-emitters, due to their short range in tissues, would be more appropriate for the effective killing of circulating cells with a minimal irradiation of the blood.[42] No more than a few studies were conducted with α-emitting radionuclides, such as ^{225}Ac (half-life 10 days), which were mostly attached through chelation.[43]

2.3.1 Radiolabeling with ^{90}Y

^{90}Y is a high-energy β-emitter with optimal nuclear physical characteristics (half-life 64.1 h, E_{max} = 2.27 MeV) for radionuclide therapy. It can affect tumor cells up to a maximum depth of 11 mm in the soft tissue. This is described by the cross fire effect occurring due to the long path of β-particles that crosses multiple individual cells, decreasing the need for targeting each cancer cell with the radiopharmaceutical. Radiolabeled NPs, such as ^{90}Y-silicate/citrate colloid and ^{186}Re-sulfur colloid, have been used for radiosynovectomy with very encouraging results, especially in Europe.[44] The method is based on the local intraarticular injection of nanoparticulates/colloids labeled with suitable therapeutic radionuclides into a diseased joint, where they are phagocytized by the macrophages of the inflamed synovial membrane delivering a selective radiation dose to the synovium. ^{90}Y-labeled colloid NPs, such as antimony trisulfide colloid (Sb_2S_3)[45] and tin fluoride colloid (SnF-c)[46] have a potential application in radiosinevactomy.[47] SnF-c particles were ^{90}Y labeled by the addition of $^{90}YCl_3$ before the formation of primary particles (nucleation) and particle growth. These particles first aggregate and finally agglomerate due to the increased temperature, agitation, and aging (schematically represented in Fig. 1.4.7).The particle size of ^{90}Y-SnF-c for different therapeutic applications is controlled by manipulating the conditions under which the colloids form.

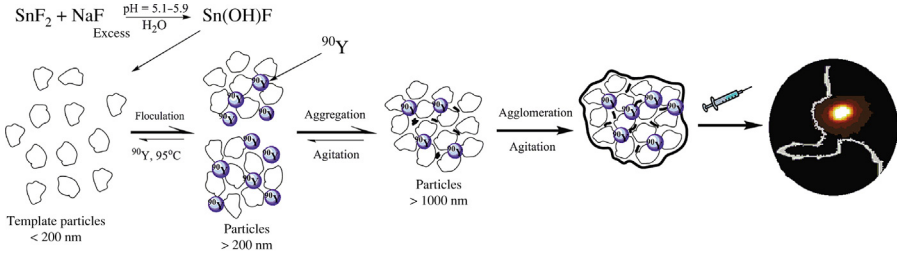

FIGURE 1.4.7 Formation of ^{90}Y-SnF-c Agglomerates From Template Particles and Scintigraphic Images Recorded at 96 h After Intraarticular Injection in Wistar Rats.

Reproduced from Jankovic D, Vranjes-Djuric S, Djokic D, Markovic M, Ajdinovic B, Jaukovic L, et al. ^{90}Y-labeled tin fluoride colloid as a promising therapeutic agent: Preparation, characterization, and biological study in rats. J Pharm Sci *2012;**101**(6):2194–203.*[46]

Among the different varieties of NPs proposed for use in radiosynovectomy, HAp hold considerable promise mainly due to its excellent properties.[48] Favorable properties of HAp (such as biocompatibility, the ease of synthesizing them within the desired particle size range, and very high affinity for metal ions) have led to extensive studies on radiolabeled HApNPs with a wide variety of therapeutic radionuclides, including ^{90}Y,[49] ^{153}Sm,[50] ^{177}Lu,[51] ^{169}Er,[52] and ^{166}Ho.[53] The direct labeling of HApNPs has been demonstrated to be a convenient and reproducible method for the facile preparation of ^{90}Y-labeled HApNPs with a high radiolabeling yield (>98%) and radiochemical purity.[54]

The direct labeling approach was also used for ^{90}Y labeling of both Fe_3O_4-naked and Fe_3O_4-PEG600diacid NPs.[55] The carboxylate-rich surface of Fe_3O_4-PEG600diacid NPs is suitable for labeling with positively charged $^{90}Y^{3+}$. Therefore, the labeling resulted in a very high labeling yield (99%) and good in vitro and in vivo stability. Due to the significant uptake of ^{90}Y-Fe_3O_4-PEG600 NPs in liver and their low uptake by other tissues, magnetite NPs labeled with β-emitters could be suitable for use in the combined radiotherapy–hyperthermia cancer treatment. Magnetic NPs coated with proteins, such as human serum albumin (HSA), were also effectively ^{90}Y labeled by the direct approach, without any further surface chemical modification.[56] The indirect ^{90}Y labeling of NPs is possible via different ligands [2,3-dicarboxypropane-1,1-diphosphonic acid (DPD) (Fig. 1.4.8)[57] and DMSA], which are capable of forming stable complexes with ^{90}Y.

2.3.2 Radiolabeling with ^{177}Lu

^{177}Lu (half-life 6.7 days) is the ideal β^- radionuclide for theranosis, as it has a particulate emission (β^- or Auger electron) for effecting therapy and emits several accompanying γ-photons of 208 keV (11%) and 113 keV (6.4%), which are used for diagnostic evaluation and dosimetry.[58] The advantage of the long half-life of ^{177}Lu has been utilized in mapping the pharmacokinetics of potential agents, in radiosynovectomy of knee joints, and the therapy of hepatocellular carcinoma. Several studies

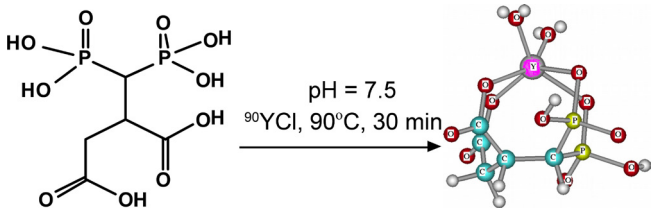

FIGURE 1.4.8 Indirect ^{90}Y-Labeling of NPs via 2,3-Dicarboxypropane-1,1-Diphosphonic Acid (DPD).

The energy minimized structure of proposed complex ^{90}Y-DPD.

Reproduced from Djokić DD, Janković DL, Nikolić NS. Labeling, characterization, and in vivo localization of a new ^{90}Y-based phosphonate chelate 2,3-dicarboxypropane-1,1-diphosphonic acid for the treatment of bone metastases: comparison with ^{99m}Tc–DPD complex. Bioorg Med Chem *2008;**16**(8):4457–65.*[57]

were conducted with ^{177}Lu-labeled AuNPs for imaging and therapy in tumor-bearing mice. AuNPs modified with PEG chains linked to DOTA made complex compounds with ^{177}Lu. Gold nanoseeds injected intratumorally were highly effective for inhibiting the growth of breast cancer tumors in CD-1 athymic mice and caused no normal organ toxicity.[59] Targeting with ^{177}Lu-AuNPs conjugated to RGD peptide showed a higher delivery into the tumor site than non-RGD and ^{177}Lu-RGD controls, highlighting the potential therapeutic capacity of radiolabeled NPs for endoradiotherapy.[60] Based on the previous work, where ^{68}Ga-labeled DOTA–conjugated bisphosphonates were investigated as PET-imaging agents, a few DOTA-based bisphosphonates were synthesized and labeled with ^{177}Lu for potential application in treating metastatic bone tumors.[61]

3 RADIOLABELED NPs IN NUCLEAR MEDICINE IMAGING AND BIODISTRIBUTION STUDIES

Different types of NPs have so far been labeled with radionuclides: from inorganic and organic to the metal and hybrid ones. Due to their good mechanical properties, chemical resistance, biocompatibility, and optical and electrical properties, diamond nanoparticles (ND) represent a special research challenge in radiolabeling technologies.[62,63] Radiolabeled NDs may be suitable not only for bioimaging applications, due to their stability, but they may also have wider applications. Their surface enables new possibilities for functionalization, as well as the uploading of suitable proteins and drugs. ^{3}H labeling of detonation nanodiamonds was performed by using tritium microwave plasma (Fig. 1.4.9).[64] The analysis shows that 93% of the tritium atoms are strongly bound to the surface, while 7% are built into the ND core.

Exosomes are extracellular nanosized vesicles that most cells produce. Macrophage-derived exosome-mimetic nanovesicles were labeled with ^{99m}Tc and their distribution was analyzed using the SPECT/CT technique in vivo. The results

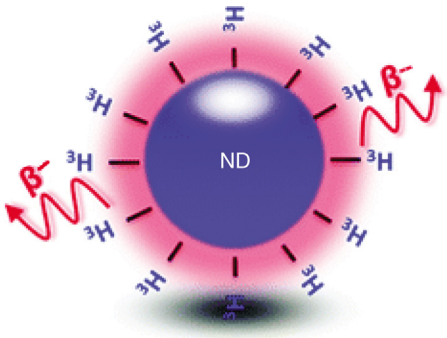

FIGURE 1.4.9 Tritium-Labeled Diamond Nanoparticles (ND).

Reproduced from Girard HA, El-Kharbachi A, Garcia-Argote S, Petit T, Bergonzo P, Rousseau B, et al. Tritium labeling of detonation nanodiamonds. Chem Commun *2014;**50**(22):2916–8.*[64]

enabled the determination of the highest accumulation of ^{99m}Tc-exosome-mimetic nanovesicles in the liver.[65]

The biodistribution of PLGA NPs with and without encapsulated ascorbic acid in healthy rats was examined after their direct labeling with ^{99m}Tc, which binds outside, on the surface of NPs.[66] The investigated nanospheres exhibit a prolonged blood circulation time accompanied with a time-dependent reduction in the lungs, liver, and spleen. This is a quick and convenient method to investigate the pharmacological behavior of a new nanoparticulate system for controlled and systemic drug delivery with a double effect.[67,68] In such a system, it is of utmost importance to study the release of drugs from bioresorbable polymers and, in the second stage, after the resorption of the polymer, to investigate the potential of nonbioresorbable calcium phosphate as a filler in a bone defect. The surface properties of PLGA/HAp core–shell NPs loaded with clindamycin and their changes under the simulated physiological conditions during the degradation process could also be investigated using a radiotracer method.[69]

Radiolabeled nanomaterials based on graphene, including graphene, graphene oxide (GO), reduced graphene oxide (rGO), graphene quantum dots (GQDs), and their derivatives indicate their high potential as imaging agents in a variety of bioimaging applications, especially in PET/SPECT.[70] ^{111}In-mesoporous silica nanoparticle (MSN) proved to be suitable for the tracking of neural stem cells in glioblastoma therapies. Multimodal dynamic in vivo imaging of NSCs behavior in the brain is an important parameter in the design of a controlled, targeted, and successful therapy. MSNs were labeled with ^{111}In using DOTA-NHS-ester through amide formation. SPECT confirmed the ability of ^{111}In-MSN-NSCs to penetrate through the blood–brain barrier and their localization in tumor cells.[71]

Multimodality imaging by taking advantage of two or more imaging modalities can provide structural, functional, and molecular information of importance for the diagnosis and treatment.[72] It is possible to couple, for example, magnetic

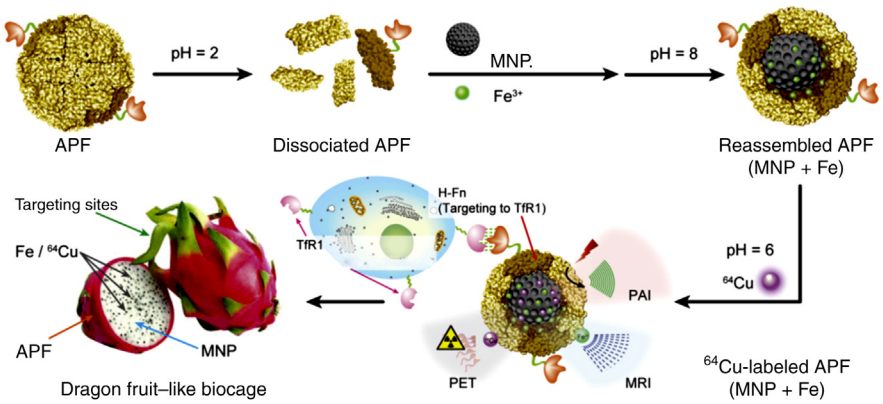

FIGURE 1.4.10 Schematic Illustration of AMF Nanocage Synthesis.

AMP, APF:Melanin:Fe^{3+}; *APF*, apoferritin; *H-Fn*, human H-ferritin; *MNP*, melanin nanoparticle; *PAI*, photoacoustic imaging, *TfR1*, transferrin receptor.

Reproduced from Yang M, Fan Q, Zhang R, Cheng K, Yan J, Pan D, et al. Dragon fruit-like biocage as an iron trapping nanoplatform for high efficiency targeted cancer multimodality imaging. Biomaterials *2015;**69**:30–7.*[74]

resonance (MR)-active NPs to a chelating system, thereby enabling in vivo tracking by multimodal imaging techniques (e.g., SPECT/MRI, PET/MRI). The synthesized core/shell NPs of $Co_{0.16}Fe_{2.84}O_4$@$NaYF_4$(Yb, Er) and Fe_3O_4@$NaYF_4$(Yb, Tm) were stabilized with bisphosphonate polyethylene glycol conjugates (BP-PEG) and radiolabeled with ^{18}F or ^{64}Cu and ^{99m}Tc. The fabricated particles have shown the advanced features and the possibility of application in the trimodal imaging (MRI, PET/SPECT, and fluorescent imaging). A high colloidal stability and a narrow size distribution (~10 nm) allow for the potential use of these particles as visual guides during surgery.[73] $^{64}Cu^{2+}$-labeled natural biopolymer–based multifunctional NPs were successfully used in cancer multimodal [PET/MRI/photoacoustic imaging (PAI)] imaging techniques.[74] "Dragon fruit–like biocage" based on apoferritin (APF) was employed (Fig. 1.4.10) to construct an efficient and excellent biostability nanoplatform [APF:Melanin:Fe^{3+} (AMF) AMF] suitable for multimodal clinical application.

Radiolabeled ultrasmall nanoparticles (USNPs) with core sizes in the 1–3 nm range have shown specific features in biomedical applications. Due to the potential of USNPs for interactions with individual cells and the covalent attachment of small molecules, active molecular targeting can be effectively achieved.[75] ^{68}Ga-labeled iron oxide has been successfully studied using PET/MR dual-modal imaging modality during specific accumulation in tumor cells.[76] ^{65}Zn-labeled CdSe/CdS/ZnS-quantum dots (^{65}Zn-Qdots) were used to achieve a full quantification of biodistribution and degradation during the in vivo test.[77] Depending on the attached or incorporated radioisotopes, USNPs systems have so far been mostly exploited in the SPECT and PET imaging modalities.

The particles of poorly crystalline HAp (D_{50} = 72 nm) coated with Ch and the Ch–PLGA polymer blend have shown multifunctional characteristics in bone tissue engineering.[78] ^{125}I was used for the in situ radiolabeling of HAp, HAp/Ch, and HAp/Ch–PLGA synthesized particles. Biodistribution studies have shown that after the intravenous administration to normal male Wistar rats, HAp particles have the highest liver accumulation 10 min after injection and rapid excretion from the body without residual radioactivity 24 h after injection.[33] HAp/Ch particles have the highest accumulation in the liver 10 min after injection with considerable amount (almost 50%) retained 24 h later. HAp/Ch–PLGA has the highest uptake in the lungs 10 min after injection and moderate retention in the same organ 24 h later (Fig. 1.4.11). The results of the biodistribution of ^{125}I-labeled particles based on HAp NPs indicate that they could be applied as organ-targeting carriers of various drugs in therapy.

Different approaches to the radiolabeling of superparamagnetic iron oxide nanoparticles (SPIONs) with ^{14}C were tested to obtain a suitable system that could be used in the analysis of biodistribution. The concept of surface functionalization and formation of a multiple core system made it possible to obtain particles with a hydrodynamic radius smaller than 100 nm. NPs are functionalized with polycarboxylate or polyamine surface functional groups, and ^{14}C is incorporated directly into the carbon backbone of the organic molecules. This concept makes it possible to obtain identical surface chemical functionality of labeled and nonlabeled particles, enabling an accurate analysis prior to potential clinical applications.[79] NP carrier crown ether-conjugated silica (SiNPs) is radiolabeled with ^{22}Na with a loading efficacy of 98.1% ± 1.4%. Due to the relatively long half-life of 2.6 years, this radionuclide has not had a wider application in biomedicine. However, for these reasons, ^{22}Na may represent a practical choice in research. The 1-month in vivo study on female BALB/c mice (6-weeks old) showed that ^{22}Na-SiNPs were removed from the organism after 2 weeks, and completely after a month. The highest accumulation of particles was recorded in the liver, 5 min after intravenous administration.[80] Heat-induced metal ion-binding reaction, which enables radiolabeling without modifying the surface structure, was used for the labeling of paramagnetic IONPs. Feraheme (FH, solution composed of a nonstoichiometric Fe_3O_4 magnetite core, approximately 5–10 nm in diameter stabilized with a carboxymethyl dextran coating; total size: 17–31 nm diameter) NPs were labeled with ^{89}Zr in a thermal reaction at 120°C in less than 60 min. The biodistribution of ^{89}Zr-FHNPs 96 h after the intravenous injection to mice indicated the uptake of ^{89}Zr-FH in the lymphatic system.[81]

To analyze and interpret the biodistribution of various components of multicomponent and more complex nanosystems the concept of dual radiolabeling of NPs was applied. Citrate-coated AuNPs (monodisperse, 14 nm in diameter) were labeled with ^{14}C and ^{198}Au. By using liquid scintillation to determine ^{14}C and γ-spectroscopy for ^{198}Au, different biodistribution profiles were determined for the Au core and the citrate surface coating over time. The obtained results of biodistribution show that over time the delamination and degradation of the citrate coating of NPs occur.[82] PLGA-coated IONPs were labeled with two γ-emitters ^{111}In and ^{125}I (Fig. 1.4.12), such that during the synthesis Au was labeled with ^{111}In and PLGA with ^{125}I. The

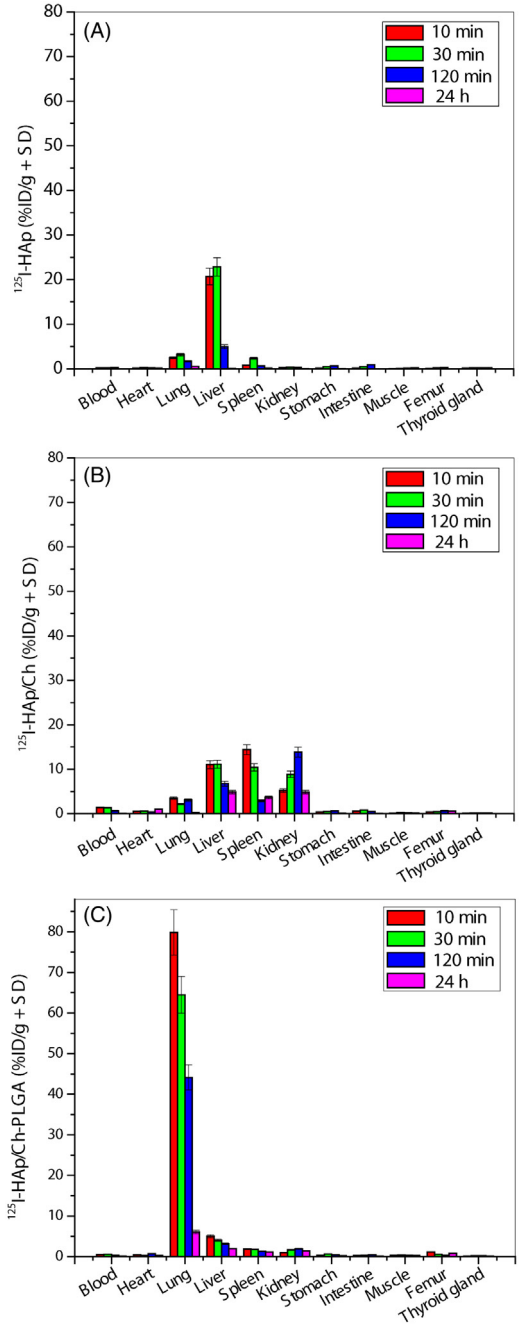

FIGURE 1.4.11

Biodistribution of (A) ^{125}I-hydroxyapatite (HAp), (B) ^{125}I-HAp/chitosan (Ch), and (C) ^{125}I-HAp/Ch–poly(lactide-*co*-glycolide) (PLGA).

Reproduced from Ignjatović N, Djurić SV, Mitić Ž, Janković D, Uskoković D. Investigating an organ-targeting platform based on hydroxyapatite nanoparticles using a novel in situ method of radioactive 125 Iodine labeling. Mater Sci Eng C *2014;**43**:439–46.*[33]

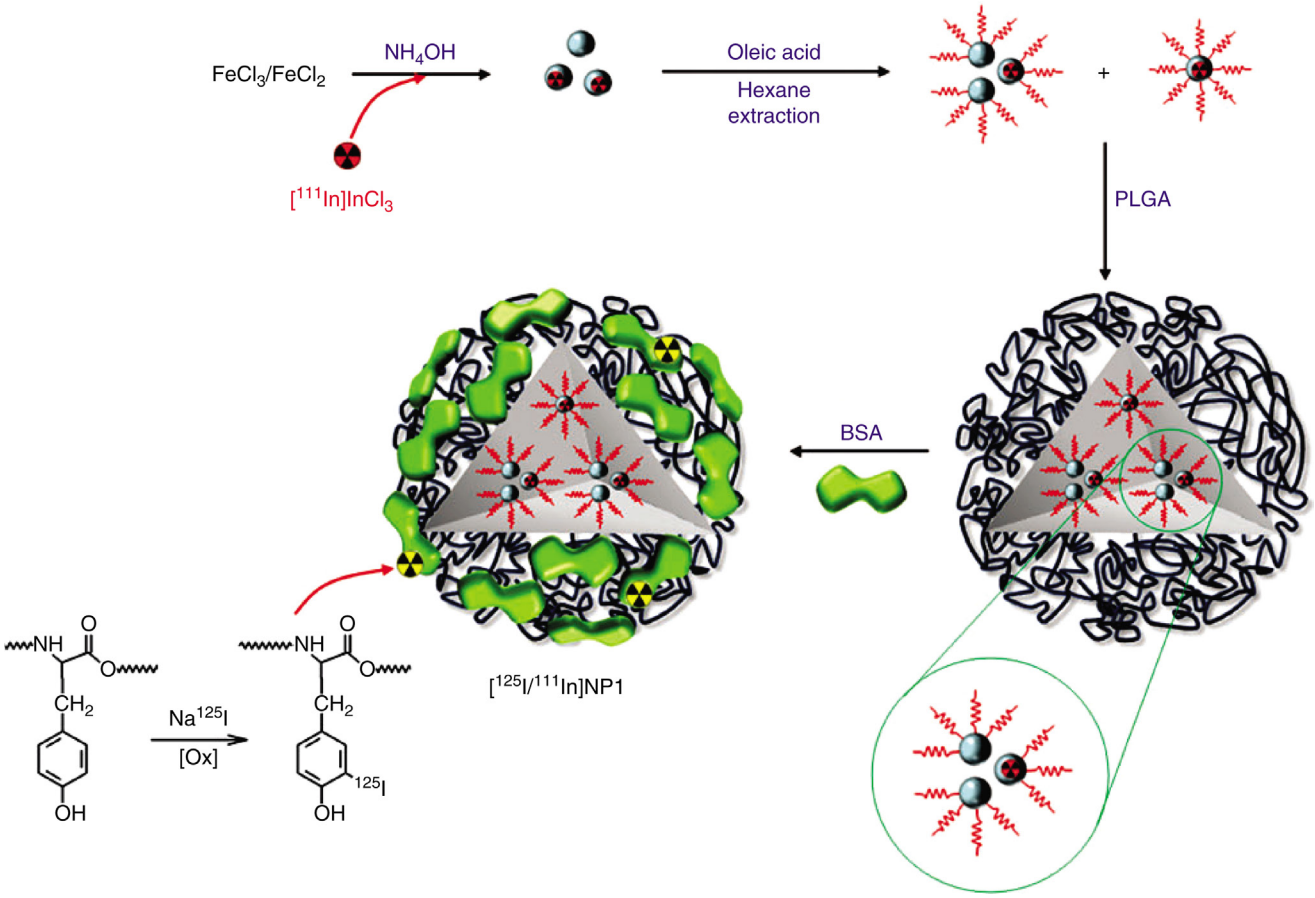

FIGURE 1.4.12 Schematic Representation of Dual-Labeled [^{125}I/^{111}In] of PLGA-Coated Iron Oxide Nanoparticles (IONPs).

BSA, Bovine serum albumin.

Data taken from Llop J, Jiang P, Marra di M, Gómez-Vallejo V, Echeverría M, Yu S, et al. Visualisation of dual radiolabelled poly(lactide-co-glycolide) nanoparticle degradation in vivo using energy-discriminant SPECT. J Mater Chem B *2015;**3**(30):6293–300.*[25]

energy-discriminant SPECT modality was used to analyze each radioisotope independently during the in vivo test with mice (BALB/cJRJ). The results showed that over time, the PLGA surface coating separated from the core, as ^{125}I was detected in the thyroid glands and urine, and ^{111}In in the liver.[25]

4 RADIOLABELED NPs IN THERAPY

New research strategies in designing radiolabeled NPs are aimed at obtaining radiolabeled multifunctional nanoobjects that would accomplish specific and targeted therapy.[83,84] Functional NPs with active targeting (targeted nanoparticles) could serve as carriers of radionuclides in the radiotherapy of cancer and induce a high mortality of cancer cells, while simultaneously sparing normal cells with minimal side effects.[85] HApNPs radiolabeled with ^{99m}Tc have shown high stability during in vivo studies in mice. The results showed a higher affinity to bone tissues in contrast to the surrounding muscle tissue.[86]

To achieve a more specific targeting, targeted nanoparticles are functionalized with various molecules. Anticancer therapeutic properties of the ^{125}I-labeled hybrid nanosized cyclic RGD–conjugated AuNPs (cRGD-AuNPs) system were tested (including acute apoptosis 2 days posttreatment and long-term influence up to 21 days). The results confirmed the effective targeting of tumor with ^{125}I-cRGD-AuNP and the suppression of its growth.[87] It has been demonstrated that the systems based on AuNPs functionalized with an epidermal growth factor as carriers of ^{111}In are successful in the targeting and therapy of epidermal growth factor receptor–positive cancers.[88] Targeted radiotherapy was also successfully achieved with conjugated surfaces of nanosystems on the basis of BSA nanocapsules, silica, monoclonal antibodies, etc.[89–91]

Multifunctional nanoplatforms for the simultaneous use of radiotherapy and chemotherapy could enable significant progress in the field of nanooncology. The designed lipid–polymer hybrid nanoplatform ChemoRad (Fig. 1.4.13), which contains PLGA and lecithin, was used as a suitable carrier for docetaxel, ^{111}In, and ^{90}Y.[92] The results obtained with the prostate cancer model confirmed the realization of highly specific targeted delivery of the drug with increased effective radiotherapy at the same time.

5 RADIOLABELED NPs IN THERANOSTICS

Multifunctional nanoparticulate systems with hybrid and improved properties are a result of creative research. Clear boundaries between objects for diagnostic imaging, therapy, or biodistribution have almost disappeared. The term "theranostics" has unified the diagnostic and therapeutic potentials of the system into a single agent to achieve efficient, specific, and individual therapy in various diseases.[94]

Gadolinium-doped hydroxyapatite (HAp-Gd) nanorods could be used as theranostic NPs to detect the early stages of osteosarcoma, or as carriers of radioisotopes in therapy. Gadolinium endows HAp with paramagnetic properties, while phosphorous and gadolinium in the HAp-Gd sample can be activated by neutron

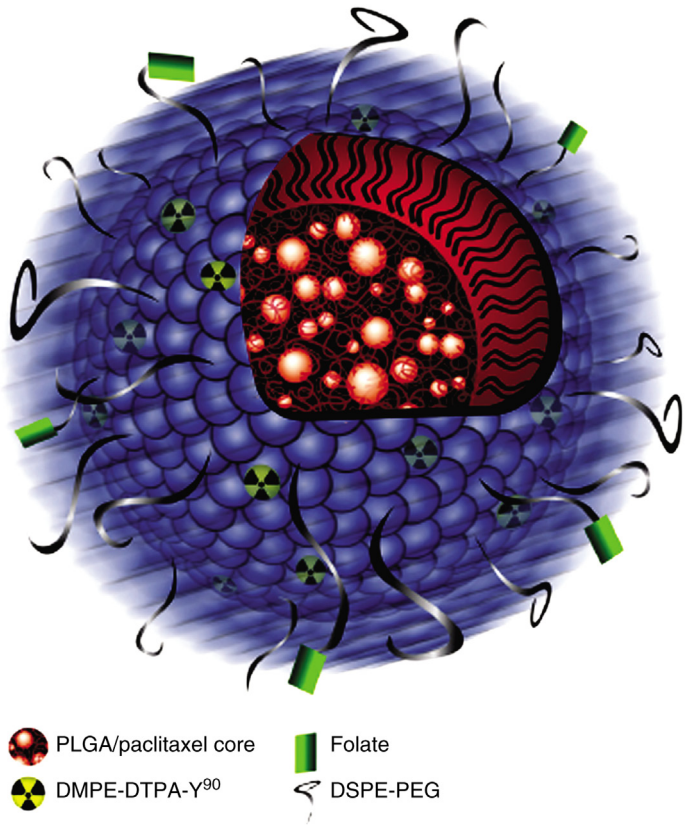

FIGURE 1.4.13 Schematic Representation of the ChemoRad NPs.

DMPE, 1,2-dimyristoyl-sn-glycero-3-phosphoethanolamine; *DSPE*, 1,2-distearoyl-sn-glycero-3-phosphoethanolamine.

Reproduced from Werner ME, Karve S, Sukumar R, Cummings ND, Copp JA, Chen RC, et al. Folate-targeted nanoparticle delivery of chemo-and radiotherapeutics for the treatment of ovarian cancer peritoneal metastasis. Biomaterials *2011;**32**(33):8548–54.*[93]

capture, in a nuclear reactor, producing ^{32}P and ^{159}Gd radioisotopes.[95] The multifunctional platform based on single-walled carbon nanotubes (SWNTs) coated with a shell of polydopamine (PDA) was modified with PEG. SWNT@PDA-PEG was labeled with ^{131}I nucleotide, which potentially allows nuclear imaging and cancer therapy. An in vivo study in mice confirmed the accumulation of intravenously administered ^{131}I-SWNT@PDA-PEG in the tumor tissues. The PDA coating not only allowed an easy labeling with ^{131}I but also its delivery, due to which the system was able to perform radionuclide therapy as well.[96]

A particular research challenge is focused on the preparation of radiolabeled NPs with significant in vivo stability. A detailed analysis of the chelator-free radiolabeling technique indicates the vital importance of deprotonated silanol groups during

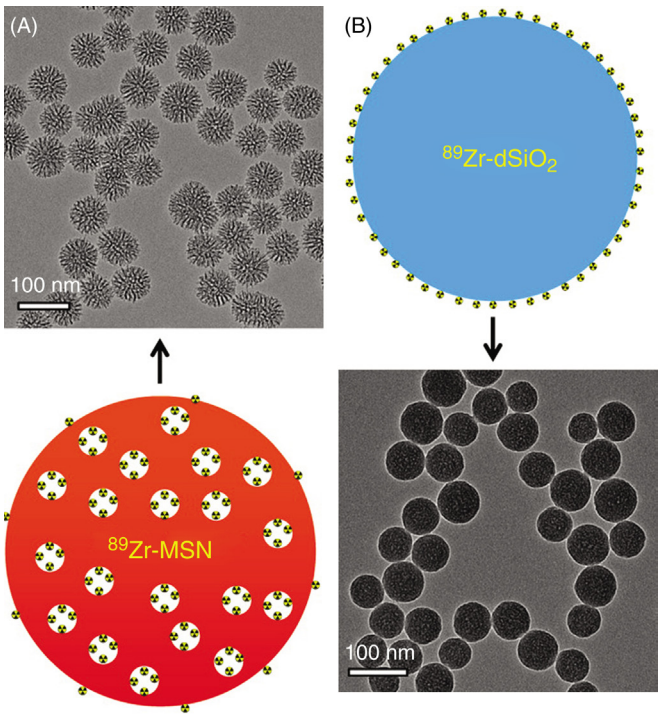

FIGURE 1.4.14 ^{89}Zr-Labeled Silica NPs.

(A) mesoporous silica NPs (MSN) and (B) nonporous silica NPs ($dSiO_2$).

Adapted and reprinted from Chen F, Goel S, Valdovinos HF, Luo H, Hernandez R, Barnhart TE, et al. In vivo integrity and biological fate of chelator-free zirconium-89-labeled mesoporous silica nanoparticles. ACS Nano *2015;**9**(8):7950–9.*[97]

the labeling of MSN (Fig. 1.4.14A) and nonporous ($dSiO_2$) silica NPs (Fig. 1.4.14B) with ^{89}Zr to obtain long stable systems. The in vivo study of the stability of these systems indicates that the detachment rate of ^{89}Zr-MSN is about 20 times slower than that of ^{89}Zr-$dSiO_2$. The results obtained with PET modality indicated that the existence of mesochannels within MSN particles is responsible for the high stability of ^{89}Zr-MSN system over a period of 3 weeks.[97] After the injection of ^{89}Zr-MSN, their accumulation in the liver and spleen can be perceived, while the bone uptake is not present, which is not the case with ^{89}Zr-$dSiO_2$.

A long circulation half-life of in vivo radiolabeled NPs leaves enough time for the EPR effect and the successful implementation of this type of particles in theragnostics. The ^{64}Cu-labeled PEGylated reduced graphene oxide–IONPs (^{64}Cu-PEGylated rGO–IONPs), reaching about 68 nm in size, were intravenously administered to mice that had an ischemic hind limb. On the basis of PET and Doppler imaging it was determined that the accumulation of particles in the ischemic hind limb was the highest after 3 days and the lowest after 17 days.[98]

ACKNOWLEDGMENTS

This work was supported by grants of the Ministry of Education and Science of the Republic of Serbia, under project no. III45004 and III45015.

REFERENCES

1. Soo Lee D, Im HJ, Lee YS. Radionanomedicine: widened perspectives of molecular theragnosis. *Nanomedicine* 2015;**11**:795–810.
2. Vranješ S, Jovanović MS, Prvulović M, Stefanović LJ, Kljajić R, Ratajac R. Chemical and biological properties of verapamil labeled with technetium-99m-potential myocardial imaging agents. *J. Radioanal Nucl Chem* 2002;**253**:81–6.
3. de Barros ALB, Tsourkas A, Saboury B, Nascimento Cardoso V, Alavi A. Emerging role of radiolabeled nanoparticles as an effective diagnostic technique. *EJNMMI Res* 2012;**2**:39.
4. Ghai A, Singh B, Panwar Hazari P, Schultz MK, Parmar A, Kumar P, et al. Radiolabeling optimization and characterization of ^{68}Ga-labeled DOTA-polyamido-amine dendrimer conjugate—animal biodistribution and PET imaging results. *Appl Radiat Isot* 2015;**105**:40–6.
5. Beyer G-J, Miederer M, Vranješ-Đurić S, Čomor JJ, Kuenzi G, Hartley O, et al. Targeted alpha therapy in vivo: direct evidence for single cancer cell kill using ^{149}Tb-Rituximab. *Eur J Nucl Med Mol Imag* 2004;**1**(4):547–54.
6. Fani M, Vranješ S, Archimandritis SC, Potamianos S, Xanthopoulos S, Bouziotis P, et al. Labelling of monoclonal antibodies with samarium-153 for potential use in radioimmunotherapy. *Appl Radiat Isot* 2002;**57**:665–74.
7. Yeong C-H, Cheng MH, Ng KH. Therapeutic radionuclides in nuclear medicine: current and future prospects. *J Zhejiang Univ Sci B* 2014;**15**(10):845–63.
8. Stockhofe K, Postema JM, Schieferstein H, Ross TL. Radiolabeling of nanoparticles and polymers for PET imaging. *Pharmaceuticals* 2014;**7**:392–418.
9. Srivastava SC, Mausner LF. Therapeutic radionuclides: production, physical characteristics, and applications. In: Baum RP, editor. *Therapeutic nuclear medicine, medical radiology and radiation oncology*. Berlin, Heidelberg: Springer-Verlag; 2013. p. 11–41.
10. Maia AL, Cavalcante CH, De Souza MG, De Carolina AF, Rubello D, Chondrogiannis S, et al. Hydroxyapatite nanoparticles: preparation, characterization, and evaluation of their potential use in bone targeting: an animal study. *Nucl Med Commun* 2016;**37**:775–82.
11. Bhatt C, Srivastava P, Pandey P, Khan P, Panda W. Nose to brain delivery of astaxanthin-loaded solid lipid nanoparticles: fabrication, radio labeling, optimization and biological studies. *RSC Adv* 2016;**6**:10001–10.
12. Tassano MR, Audicio PF, Gambini JP, Fernandez M, Damian JP, Moreno M, et al. Development of ^{99m}Tc(CO)$_3$-dendrimer-FITC for cancer imaging. *Bioorg Med Chem Lett* 2011;**21**:5598–601.
13. Lakić M, Sabo Lj, Ristić S, Savić A, Petričević S, Nikolić N, et al. Synthesis and biological evaluation of ^{99m}Tc-tricarbonyl complex of O,O′-diethyl ethylenediamine-*N*,*N*′-di-3-propanoate as potential tumor diagnostic agents. *Appl Organomet Chem* 2016;**30**:81–8.
14. Psimadas D, Bouziotis P, Georgoulias P, Valotassiou V, Tsotakos T, Loudos G. Radiolabeling approaches of nanoparticles with ^{99m}Tc. *Contrast Media Mol Imag* 2013;**8**:333–9.
15. Helbok A, Decristoforo C, Dobrozemsky G, Rangger C, Diederen E, Stark B, et al. Radiolabeling of lipid-based nanoparticles for diagnostics and therapeutic applications: a comparison using different radiometals. *J Liposome Res* 2010;**20**:219–27.

16. Dams ETM, Oyen WJG, Boerman OC, Storm G, Laverman P, Kok PJM, et al. ^{99m}Tc PEG Liposomes for the scintigraphic detection of infection and inflammation: clinical evaluation. *J Nucl Med* 2000;**41**:622–30.
17. Laverman P, Dams ETM, Oyen WJG, Storm G, Koenders EB, Prevost R, et al. A novel method to label liposomes with Tc-99m via the hydrazino nicotinyl derivative. *J Nucl Med* 1999;**40**:192–7.
18. Hwang H, Kwon J, Oh PS, Lee TK, Na KS, Lee CM, et al. Peptide-loaded nanoparticles and radionuclide imaging for individualized treatment of myocardial ischemia. *Radiology* 2014;**273**:160–7.
19. Faintuch BL, Núñez GE, Teodoro R, Moro AM, Mengatti J. Radiolabeled nano-peptides show specificity for an animal model of human PC3 prostate cancer cells. *Clinics* 2011;**66**:327–36.
20. Zaluzhna O, Brightful L, Allison TC, Tong YJ. Spectroscopic evidence of a bidentate-binding of *meso*-2,3-dimercaptosuccinic acid on silver nanoclusters. *Chem Phys Lett* 2011;**509**:148–51.
21. Mirković M, Janković D, Vranješ-Đurić S, Radović M, Stanković D, Mijin D, et al. Novel tetradentate diamine dioxime ligands: synthesis, characterization and in vivo behavior of their ^{99m}Tc-complexes. *Appl Organomet Chem* 2012;**26**:347–55.
22. Tsiapa I, Efthimiadou EK, Fragogeorgi E, Loudos G, Varvarigou AD, Bouziotis P, et al. ^{99m}Tc-labeled aminosilane-coated iron oxide nanoparticles for molecular imaging of $\alpha_v\beta_3$-mediated tumor expression and feasibility for hyperthermia treatment. *J Colloid Interface Sci* 2014;**433**:163–75.
23. Psimadas D, Georgoulias P, Valotassiou V, Loudos G. Molecular nanomedicine towards cancer: ^{111}In-labeled nanoparticles. *J Pharm Sci* 2012;**101**:2271–80.
24. Kanazaki K, Sano K, Makino A, Yamauchi F, Takahashi A, Homma T, et al. Feasibility of poly(ethylene glycol) derivatives as diagnostic drug carriers for tumor imaging. *J Control Release* 2016;**226**:115–23.
25. Llop J, Jiang P, Marradi M, Gómez-Vallejo V, Echeverría M, Yu S, et al. Visualisation of dual radiolabelled poly(lactide-*co*-glycolide) nanoparticle degradation in vivo using energy discriminant SPECT. *J Mater Chem B* 2015;**3**:6293–300.
26. Laan AC, Santini C, Jennings L, de Jong M, Bernsen MR, Denkova AG. Radiolabeling polymeric micelles for in vivo evaluation: a novel, fast, and facile method. *EJNMMI Res* 2016;**6**:1–10.
27. Kurihara K, Ueda M, Hara I, Hara E, Sano K, Makino A, et al. Inflammation- induced synergetic enhancement of nanoparticle treatments with DOXIL® and ^{90}Y-Lactosome for orthotopic mammary tumor. *J Nanopart Res* 2016;**18**:137.
28. Silva F, Zambre A, Campello MPC, Gano L, Santos I, Ferraria AM, et al. Interrogating the role of receptor-mediated mechanisms: biological fate of peptide-functionalized radiolabeled gold nanoparticles in tumor mice. *Bioconjug Chem* 2016;**27**:1153–64.
29. Benezra M, Penate-Medina O, Zanzonico PB, Schaer D, Ow H, Burns A, et al. Multimodal silica nanoparticles are effective cancer-targeted probes in a model of human melanoma. *J Clin Invest* 2011;**121**:2768–80.
30. Tang Y, Zhang C, Wang J, Lin X, Zhang L, Yang Y, et al. MRI/SPECT/fluorescent tri-modal probe for evaluating the homing and therapeutic efficacy of transplanted mesenchymal stem cells in a rat ischemic stroke model. *Adv Funct Mater* 2015;**25**:1024–34.
31. Nikolić N, Vranjes-Đurić S, Janković D, Đokić D, Mirković M, Bibić N, et al. Preparation and biodistribution of radiolabeled fullerene C60 nanocrystals. *Nanotechnology* 2009;**20**:385102–9.

32. Xie GP, Lu WX. In vivo tissue distribution of hydroxyapatite nanoparticles modified with aminopropyltriethoxysilane. *Chinese Pharm J* 2015;**50**(8):695–9.
33. Ignjatović N, Vranješ Đurić S, Mitić Ž, Janković D, Uskoković D. Investigating an organ-targeting platform based on hydroxyapatite nanoparticles using a novel in situ method of radioactive ^{125}Iodine labeling. *Mater Sci Eng C* 2014;**43**:439–46.
34. Ai F, Ferreira CA, Chen F, Cai W. Engineering of radiolabeled iron oxide nanoparticles for dual modality imaging. *Wiley Interdiscip Rev Nanomed Nanobiotechnol* 2016;**8**:619–30.
35. Urakami T, Kawaguchi AT, Akai S, Hatanaka K, Koide H, Shimizu K, et al. In vivo distribution of liposomeencapsulated hemoglobin determined by positron emission tomography. *Artif Organs* 2009;**33**:164–8.
36. Pressly ED, Rossin R, Hagooly A, Fukukawa K, Messmore BW, Welch MJ, et al. Structural effects on the biodistribution and positron emission nanoparticles comprised of amphiphilic block graft copolymers. *Biomacromolecules* 2007;**8**:3126–34.
37. Yang X, Hong H, Grailer JJ, Rowland IJ, Javadi A, Hurley SA, et al. cRGD-functionalized, DOX-conjugated, and Cu-labeled superparamagnetic iron oxide nanoparticles for targeted anticancer drug delivery and PET/MR imaging. *Biomaterials* 2011;**32**:4151–60.
38. Jarrett BR, Gustafsson B, Kukis DL, Louie AY. Synthesis of ^{64}Cu-labeled magnetic nanoparticles for multimodal imaging. *Bioconjug Chem* 2008;**19**:1496–504.
39. Rösch F, Riss PJ. The renaissance of the ^{68}Ge/^{68}Ga radionuclide generator initiates new developments in ^{68}Ga radiopharmaceutical chemistry. *Curr Top Med Chem* 2010;**10**:1633–68.
40. Holub J, Meckel M, Kubíček V, Rösch F, Hermann P. Gallium(III) complexes of NOTA-bis(phosphonate) conjugates as PET radiotracers for bone imaging. *Contrast Media Mol Imaging* 2015;**10**:122–34.
41. Morales-Avila E, Ortiz-Reynoso M, Seyedeh Fatemeh M, Amirhossein A. Multifunctional radiolabeled nanoparticles: strategies and novel classification of radiopharmaceuticals for cancer treatment. *J Drug Target* 2015;**23**:191–201.
42. Beyer GJ, Čomor JJ, Daković M, Soloviev D, Tamburella C, Hageb E, et al. Production routes of the alpha emitting 149-Tb for medical application. *Radiochim Acta* 2002;**90**:247–52.
43. McLaughlin MF, Woodward J, Boll RA, Wall JS, Rondinone AJ, Kennel SJ, et al. Gold coated lanthanide phosphate nanoparticles for targeted alpha generator radiotherapy. *PLoS One* 2013;**8**:2–9.
44. Knapp FFR, Dash A. *Radiopharmaceuticals for therapy*. India: Springer; 2016 [pp. 1–347].
45. Janković D, Maksin T, Đokić D, Milonjić S, Nikolić N, Mirković M, et al. Particle size analysis: ^{90}Y and ^{99m}Tc-labelled colloids. *J Microsc* 2008;**232**:601–4.
46. Jankovic D, Vranjes-Djuric S, Djokic D, Markovic M, Ajdinovic B, Jaukovic Lj, et al. ^{90}Y-labeled tin fluoride colloid as a promising therapeutic agent: preparation, characterization, and biological study in rats. *J Pharm Sci* 2012;**101**:2194–203.
47. van der Zant FM, Boer RO, Moolenberg JD, Jahangier ZN, Bijlsma JWJ, Jacobs JWG. Radiation synovectomy with ^{90}Yttrium, ^{186}Rhenium and ^{169}Erbium: a systematic literature review and meta-analysis. *Clin Exp Rheumatol* 2009;**27**:130–9.
48. Chakraborty S, Vimalnath KV, Rajeswari A, Shinto A, Radhakrishnan ER, Dash A. Radiolanthanide-labeled HA particles in the treatment of rheumatoid arthritis: ready-to-use cold kits for rapid formulation in hospital radiopharmacy. *J Radioanal Nucl Chem* 2014;**302**:875–81.
49. Kampen WU, Voth M, Pinkert J, Krause A. Therapeutic status of radiosynoviorthesis of the knee with yttrium [^{90}Y] colloid in rheumatoid arthritis and related indications. *Rheumatology* 2007;**46**:16–24.

50. Chinol M, Vallabhajosula S, Goldsmith SJ, Klein MJ, Deutsch KF, Chinen LK, et al. Chemistry and biological behaviour of Samarium-153 and Rhenium-186-labeled hydroxyapatite particles: potential radiopharmaceuticals for radiation synovectomy. *J Nucl Med* 1993;**34**:1536–42.
51. Chakraborty S, Das T, Banerjee S, Sarma HD, Venkatesh M. Preparation and preliminary biological evaluation of ^{177}Lu labeled hydroxyapatite as a promising agent for radiation synovectomy of small joints. *Nucl Med Commun* 2006;**27**:661–8.
52. Chakraborty S, Das T, Chirayil V, Lohar SP, Sharma HD. Erbium-169 labeled hydroxyapatite particulates for use in radiation synovectomy of digital joints—a preliminary investigation. *Radiochim Acta* 2014;**102**:443–50.
53. Unni PR, Chaudhari PR, Venkatesh M, Ramamoorthy N, Pillai MRA. Prepration and bioevaluation of ^{166}Ho labeled hydroxyapatite (HA) particles for radiosynovectomy. *Nucl Med Biol* 2002;**29**:199–209.
54. Vimalnath KV, Chakraborty S, Rajeswari A, Sarma HD, Nuwad J, Pandey U, et al. Radiochemistry, pre-clinical studies and first clinical investigation of ^{90}Y-labeled hydroxyapatite (HA) particles prepared utilizing ^{90}Y produced by (n,γ) route. *Nucl Med Biol* 2015;**42**:455–64.
55. Radovic M, Calatayud MP, Goya GF, Ibarra MR, Antic B, Spasojevic V, et al. Preparation and in vivo evaluation of multifunctional ^{90}Y-labeled magnetic nanoparticles designed for cancer therapy. *J Biomed Mater Res A* 2015;**103**:126–34.
56. Radović M, Vranješ-Đurić S, Nikolić N, Janković D, Goya GF, Torres T, et al. Development and evaluation of ^{90}Y-labeled albumin microspheres loaded with magnetite nanoparticles for possible applications in cancer therapy. *J Mat Chem* 2012;**22**:24017–25.
57. Djokić DDJ, Janković DLJ, Nikolić NS. Labeling, characterization, and in vivo localization of a new ^{90}Y-based phosphonate chelate 2,3-dicarboxypropane-1,1-diphosphonic acid for the treatment of bone metastases: comparison with ^{99m}Tc-DPD complex. *Bioorg Med Chem* 2008;**16**:4457–65.
58. Banerjee S, Das T, Theranostic. Applications of Lutetium-177 in radionuclide therapy. *Curr Radiopharm* 2016;**9**:94–101.
59. Yook S, Cai Z, Lu Y, Winnik MA, Pignol JP, Reilly RM. Intratumorally injected ^{177}Lu-labeled gold nanoparticles: gold nanoseed brachytherapy with application for neoadjuvant treatment of locally advanced breast cancer. *J Nucl Med* 2016;**57**:936–42.
60. Vilchis-Juárez A, Ferro-Flores G, Santos-Cuevas C, Morales-Avila E, Ocampo-García B, Díaz-Nieto L, et al. Molecular targeting radiotherapy with cyclo-RGDfK(C) peptides conjugated to ^{177}Lu-labeled gold nanoparticles in tumor-bearing mice. *J Biomed Nanotechnol* 2014;**10**:393–404.
61. Bergmann R, Meckel M, Kubíček V, Pietzsch J, Steinbach J, Hermann P, et al. ^{177}Lu-labelled macrocyclic bisphosphonates for targeting bone metastasis in cancer treatment. *EJNMMI Res* 2016;**6**:1–12.
62. Ho D, Wang C-HK, Chow EK-H. Nanodiamonds: the intersection of nanotechnology, drug development, and personalized medicine. *Sci Adv* 2015;**1**:e1500439.
63. Mochalin VN, Shenderova O, Ho D, Gogotsi Y. The properties and applications of nanodiamonds. *Nat Nanotechnol* 2012;**7**:11–23.
64. Girard H, El-Charbachi A, Garcia-Arqote S, Petit T, Bergonzo P, Rousseau B, et al. Tritium labeling of detonation nanodiamonds. *Chem Commun* 2014;**50**:2916–8.
65. Won HD, Hongyoon C, Chul JS, Min YY, Yong PJ, Eun CN, et al. Noninvasive imaging of radiolabeled exosome-mimetic nanovesicle using ^{99m}Tc-HMPAO. *Sci Rep* 2015;**5**:15636.
66. Stevanović M, Maksin T, Petković J, Filipic M, Uskoković D. An innovative, quick and convenient labeling method for the investigation of pharmacological behavior and the metabolism of poly(DL-lactide-*co*-glycolide) nanospheres. *Nanotechnology* 2009;**20**:335102.

67. Ignjatović NL, Ninkov P, Sabetrasekh R, Uskoković DP. A novel nano drug delivery system based on tigecycline-loaded calcium phosphate coated with poly-DL-lactide-*co*-glycolide. *J Mater Sci Mater Med* 2010;**21**:231–9.
68. Ignjatović N, Uskoković V, Ajduković Z, Uskoković D. Multifunctional hydroxyapatite and poly(DL-lactide-*co*-glycolide) nanoparticles for the local delivery of cholecalciferol. *Mater Sci Eng C* 2013;**33**:943–50.
69. Vukomanović M, Šarčev I, Petronijević B, Škapin SD, Ignjatović N, Uskoković D. Poly(DL-lactide-*co*-glycolide)/hydroxyapatite core-shell nanospheres. Part 4: a change of the surface properties during degradation process and the corresponding in vitro cellular response. *Colloid Surf B* 2012;**91**:144–53.
70. Lin J, Huang X. Graphene-based nanomaterials for bioimaging. *Adv Drug Deliv Rev* 2016;**105**:242–54.
71. Cheng S-H, Yu D, Tsai H-M, Morshed R, Kanojia D, Lo L-W, et al. Dynamic in vivo SPECT imaging of neural stem cells functionalized with radiolabeled nanoparticles for tracking of glioblastoma. *J Nucl Med* 2016;**57**:279–84.
72. Xing Y, Zhao J, Conti P, Chen K. Radiolabeled nanoparticles for multimodality tumor imaging. *Theranostics* 2014;**4**:290–305.
73. Cui X, Mathe D, Kovács N, Horváth I, Jauregui-Osoro M, Torres Martin de Rosales R, et al. Synthesis, characterization, and application of core–shell $Co_{0.16}Fe_{2.84}O_4$@$NaYF_4$(Yb, Er) and Fe_3O_4@$NaYF_4$(Yb, Tm) nanoparticle as trimodal (MRI, PET/SPECT, and optical) imaging agents. *Bioconjug Chem* 2016;**27**:319–28.
74. Yang M, Fan Q, Zhang R, Cheng K, Yan J, Pan D, et al. Dragon fruit-like biocage as an iron trapping nanoplatform for high efficiency targeted cancer multimodality imaging. *Biomaterials* 2015;**69**:30–7.
75. Zarschler K, Rocks L, Licciardello N, Boselli L, Polo E, Pombo Garcia K, et al. Ultrasmall inorganic nanoparticles: state-of-the-art and perspectives for biomedical applications. *Nanomedicine* 2016;**12**:1663–701.
76. Moon SH, Yang BY, Kim YJ, Hong MK, Lee YS, Lee DS, et al. Development of a complementary PET/MR dual-modal imaging probe for targeting prostate-specific membrane antigen (PSMA). *Nanomedicine* 2016;**12**:871–9.
77. Bargheer D, Giemsa A, Freund B, Heine M, Waurisch C, Stachowski GM, et al. The distribution and degradation of radiolabeled superparamagnetic iron oxide nanoparticles and quantum dots in mice. *Beilstein J Nanotechnol* 2015;**6**:111–23.
78. Ignjatović N, Wu V, Ajduković Z, Mihajilov-Krstev T, Uskoković V, Uskoković D. Chitosan-PLGA polymer blends as coatings for hydroxyapatite nanoparticles and their effect on antimicrobial properties, osteoconductivity and regeneration of osseous tissues. *Mater Sci Eng C* 2016;**60**:357–64.
79. Nallathamby P, Mortensen N, Palko H, Malfatti M, Smith C, Sonnett J, et al. New surface radiolabeling schemes of super paramagnetic iron oxide nanoparticles (SPIONs) for biodistribution studies. *Nanoscale* 2015;**7**:6545–55.
80. Al Faraj A, Alotaibi B, Shaik AP, Shamma KZ, Al Jammaz I, Gerl J. Sodium-22-radiolabeled silica nanoparticles as new radiotracer for biomedical applications: in vivo positron emission tomography imaging, biodistribution, and biocompatibility. *Int J Nanomedicine* 2015;**10**:6293–302.
81. Boros E, Bowen A, Josephson L, Vasdev N, Holland J. Chelate-free metal ion binding and heat-induced radiolabeling of iron oxide nanoparticles. *Chem Sci* 2015;**6**:225–36.
82. Rambanapasi C, Barnard N, Grobler A, Buntting H, Sonopo M, Jansen D, et al. Dual radiolabeling as a technique to track nanocarriers: the case of gold nanoparticles. *Molecules* 2015;**20**:12863–79.

83. Yu MK, Park J, Jon S. Targeting strategies for multifunctional nanoparticles in cancer imaging and therapy. *Theranostics* 2012;**2**:3–44.
84. Koziorowski J, Stanciu A, Gómez-Vallejo V, Llop J. Radiolabeled nanoparticles for cancer diagnosis and therapy. *Anticancer Agents Med Chem* 2017;**17**:333–54.
85. Nguyen KT. Targeted nanoparticles for cancer therapy: promises and challenges. *J Nanomed Nanotechnol* 2011;**2**:103e.
86. Maia AL, Cavalcante CH, Souza MG, de Ferreira CA, Rubello D, Chondrogiannis S, et al. Hydroxyapatite nanoparticles: preparation, characterization, and evaluation of their potential use in bone targeting: an animal study. *Nucl Med Commun* 2016;**37**:775–82.
87. Su N, Dang Y, Liang G, Liu G. Iodine-125-labeled cRGD-gold nanoparticles as tumor-targeted radiosensitizer and imaging agent. *Nanoscale Res Lett* 2015;**10**:160.
88. Song L, Falzone N, Vallis KA. EGF-coated gold nanoparticles provide an efficient nanoscale delivery system for the molecular radiotherapy of EGFR-positive cancer. *Int J Radiat Biol* 2016;**92**:716–23.
89. Liang S, Jin X, Ma Y, Guo J, Wang H. Folic acid-conjugated BSA nanocapsule (*n*-BSA-FA) for cancer targeted radiotherapy and imaging. *RSC Adv* 2015;**5**:88560–6.
90. Chen F, Hong H, Zhang Y, Valdovinos H, Shi S, Kwon G, et al. In vivo tumor targeting and image-guided drug delivery with antibody-conjugated, radio labeled mesoporous silica nanoparticles. *ACS Nano* 2013;**7**:9027–39.
91. Scott A, Wolchok J, Old L. Antibody therapy of cancer. *Nat Rev Cancer* 2012;**12**:278–87.
92. Wang A, Yuet K, Zhang L, Gu F, Huynh-Le M, Radovic-Moreno A, et al. ChemoRad nanoparticles: a novel multifunctional nanoparticle platform for targeted delivery of concurrent chemoradiation. *Nanomedicine* 2010;**5**:361–8.
93. Werner ME, Karve S, Sukumar R, Cummings ND, Coppa JA, Chen RC, et al. Folate-targeted nanoparticle delivery of chemo- and radiotherapeutics for the treatment of ovarian cancer peritoneal metastasis. *Biomaterials* 2011;**32**:8548–54.
94. Xie J, Lee S, Chen X. Nanoparticle-based theranostic agents. *Adv Drug Deliv Rev* 2010;**62**:1064–79.
95. Cipreste M, Peres A, Cotta A, Aragon F, Antunes A, Leal A, et al. Synthesis and characterization of ^{159}Gd-doped hydroxyapatite nanorods for bioapplications as theranostic systems. *Mater Chem Phys* 2016;**181**:301–11.
96. Zhao H, Chao Y, Liu J, Huang J, Pan J, Guo W, et al. Polydopamine coated single-walled carbon nanotubes as a versatile platform with radionuclide labeling for multimodal tumor imaging and therapy. *Theranostics* 2016;**6**:1833–43.
97. Chen F, Goel S, Valdovinos HF, Luo H, Hernandez R, Barnhart TE, et al. In vivo integrity and biological fate of chelator-free zirconium-89-labeled mesoporous silica nanoparticles. *ACS Nano* 2015;**9**:7950–9.
98. England CG, Im H-J, Feng L, Chen F, Graves SA, Hernandez R, et al. Re-assessing the enhanced permeability and retention effect in peripheral arterial disease using radiolabeled long circulating nanoparticles. *Biomaterials* 2016;**100**:101–9.